Coherent Creation of Single Molecules from Single Atoms

A DISSERTATION PRESENTED
BY
YICHAO YU
TO
THE DEPARTMENT OF PHYSICS

IN PARTIAL FULFILLMENT OF THE REQUIREMENTS
FOR THE DEGREE OF
DOCTOR OF PHILOSOPHY
IN THE SUBJECT OF
PHYSICS

HARVARD UNIVERSITY
CAMBRIDGE, MASSACHUSETTS
DECEMBER 2020

Coherent Creation of Single Molecules from Single Atoms

Abstract

Molecules, with their rich spectrum of internal states as well as strong and tunable dipolar interactions, are promising candidates for a broad range of experiments including quantum information, quantum chemistry, precision measurement and probing physics beyond the Standard Model, and quantum simulation of interacting many-body systems. At the same time, the complexity that made them attractive also poses a significant challenge to achieve a high level of quantum control that is required in many of their potential applications. Multiple approaches are being pursued for full quantum control of molecules including association of atomic gases and direct cooling of molecules, yet it remains challenging to control molecules at single particle level due to the difficulty in tuning the atom-atom interaction and laser cooling of molecules.

In this thesis, we achieved full control on a single weakly bound ground state molecule created by coherent optical association from single atoms. We first discuss the trapping and imaging of the atoms in the optical tweezer and the cooling into a single quantum state in order to achieve the quantum control of atoms. Combining this control with the resolution and flexibility of tweezers. we developed a versatile platform to study interactions

Thesis advisor: Professor Kang-Kuen Ni   Yichao Yu

between single atoms and properties of single molecules, using precise optical spectroscopy

on pairs of atoms in the tweezer. Based on these studies, we proposed a promising pathway

for coherent all-optical creation of molecules and experimentally demonstrated full control

on the molecule including all degrees of freedom.

Contents

Listing of figures

Acknowledgments

Many thanks are owed to Kang-Kuen Ni, my advisor, for the vision on the experiment and giving me the opportunity to participate in extending the AMO toolbox and our understanding of quantum physics as a graduate student. I also learnt from her the way to do research and to manage an experiment, especially on focusing on the big picture and setting the correct priority.

Of course, none of the work included in this thesis would have been possible without the collaboration and support from many other people in the lab. I would like to thank the following people who have worked on our apparatus: Lee Liu, Nick Hutzler, Till Rosenband, Jessie Zhang, Jonathan Hood, Kenneth Wang and Lewis Picard, as well as all the members of the two other experiments in our lab for their constant support and sharing of equipment. I would like to acknowledge in particular: Lee Liu, our first graduate student (now postdoc at JILA), who was in charge of the building of our experiment and almost single-handedly implemented every preparation steps we have on the Cs atoms; Nick Hutzler, our first postdoc (now Assistant Professor at Caltech), who helped with a lot of the early building work using his abundant experience as experimental physicists and solved the loading problem for Na atoms with a brilliant method (see section 2.3); Till Rosenband, for

providing us with reliably devices and for designing and implementing the first prototype of the computer control system (see section 1); Jonathan Hood, our second postdoc (now Assistant Professor at Purdue), who joint our effort on making molecules after Nick left and, among other things, taught me everything I know now about diatomic molecules; and Kenneth Wang, our current graduate student, who is now leading the experiment to a new level.

Being part of the Harvard-MIT Center for Ultracold Atoms (CUA) is a blessing to our experiment. We were able to share ideas, techniques and hardware with other groups within the CUA and we got many inspirations for the problems we faced during our discussions. Among them, I would like to personally thank the members of my undergraduate experiment BEC-5, Jesse Amato-Grill, Ivana Dimitrova, Niklas Jepsen and Will Lundon and the advisor Wolfgang Ketterle, who introduced me to the field of AMO and taught me lessons that were invaluable throughout my PhD.

Lastly, my mom, Haiying Yan, and my dad, Xi Yu, are my great teachers and introduced me to the wonder world of science since I was a kid. They have also been supporting my decisions during my time in the U.S.. I would also like to thank my cousin, Cheng Qian, whom I have been following the footsteps of in schools. As my only close relative in the U.S., she supported me from New York City when my parents were not able to from across the sea.

0

Introduction

0.1 Ultracold Molecules

Starting with precise optical spectroscopy and the development of laser cooling and trapping technologies, the increasing measurement precision and high level of control has been one of the primary driving forces in the field of atomic physics in the past decades. Systems based on cooling and controlling atoms have been used in a wide range of applications in-

cluding quantum computing [1–5], quantum communication [6–8], precision measurement [9, 10], quantum simulation [11–18] and the study of other many body effects [19–23].

The success of the atom based systems is achieved thanks to the simple internal structures and weak interactions that enable the precise control of the atoms. Molecules, on the other hand, with their richer internal degrees of freedom including electronic orbital, electron spin, nuclear vibration, rotation and spin, have potential for stronger interaction and a larger variety of symmetry classes. Thus, molecules are more challenging to control but they may also be used in more applications including precision measurement [24–31], quantum simulations [32–43], quantum information processing [44–47], and quantum chemistry [48–51]. Moreover, compared to other systems with stronger interaction like ions and Rydberg atoms, the interacting states in molecules are long lived [52] and tunable [53] thanks to the abundance of low energy excitations, which can offer better isolation from the environment and give rise to longer coherence time.

Many applications of molecules require cooling and a high level of control on the quantum state of the molecules. Unfortunately, the properties that make molecules attractive also makes controlling them harder. Laser cooling, the enabling technique for most ultracold atom experiments, typically requires scattering of a large number of photons ($\approx 10^4 \sim 10^8$). This is possible in atomic systems due to the existence of cycling transitions

or near cycling ones that can be completely closed with one or two repumping lasers. However, the lack of selection rules for vibrational states means that such transitions generally do not exist in molecules. As a result, experiments aiming to achieve control of molecules on a similar level with atoms usually take one of the two approaches,

1. Direct laser cooling of special molecules with approximate cycling transitions [54–61].
   These are molecules with optical excited states that have a high probability of decaying down to a single vibrational state. With the help of a few vibrational repumping lasers, scattering of $\approx 10^3 \sim 10^7$ photons can be achieved. Significant progress has been made using this approach in recent years including sub-doppler cooling [62] and trapping of molecules in optical tweezers [63]. The main challenge with this approach is to achieve a better cooling performance given the still limited photon scattering budget.

2. Creation of molecules from ultracold atoms.
   First realized a decade ago [64, 65], this approach takes advantage of the mature cooling and trapping techniques developed for atoms and creates molecules from atoms that are cooled to ultracold temperature. The difficulty with this approach is in the creation of the molecule, which must be done with acceptable efficiency and coherence in order to maintain the cooling and controlling done on the atoms. This approach currently allows a lower temperature to be achieved [66–68] and this is the approach used in our experiment.

0.2 Assembly of Molecules in Optical Tweezers

Previous experiments that take the approach to create ultracold molecules from ultracold atoms do so either in a bulk gases or an optical lattice [69]. In these systems, however, the

transfer efficiency and the density of the created molecules are limited by the overlap between the spatial distribution of the two atomic species. Such overlap is controlled by the combination of the trapping potential and the intra- and inter-species interactions. Thus, a perfect overlap for molecule formation can only be achieved by fine tuning the delicate balance between these parameters and may not always be possible. Additionally, the molecules created in this manner may collide with residual atoms or other molecules causing rapid loss either through chemical reactions or by forming long-lived sticky complexes [70–72].

Since these issues are essentially all caused by the lack of direct control on the position and motion of individual atoms and molecules, we propose a general solution using optical tweezers. Created by focusing the trap light through a high numerical aperture (NA) objective, optical tweezers can trap single atoms and molecules in a flexible geometry. This setup naturally provides the high resolution required for detection and manipulation of individual atoms [73]. Taking advantage of these properties, full quantum control on single atoms has been demonstrated by cooling and rearranging the tweezers based on the loading result [74, 75]. This gives us a good starting point to deterministically create molecules by directly merging pairs of atoms instead of relying on stochastic processes or the fine tuning of parameters in previous experiments. The molecules created using this approach are also well isolated from each other, preventing loss due to collisions.

0.2.1   Two-Step All Optical Creation of Molecules

In order to create rovibronic ground-state molecules from atoms, the ≈ 100 THz binding energy must be removed coherently from the system, which may be done using a two-photon optical transition. However, due to the significant mismatch in the wavefunction size between the atomic motional ground state (≈ 1000Å) and the rovibronic ground state of the molecule (≈ 4Å), it is challenging to achieve a high Rabi frequency or short transition time, causing technical difficulties in maintaining the laser coherence during the transition. Because of this, the transfer to rovibronic ground state is typically done in two steps [30, 64, 65, 76–82]. The atoms are first associated into a weakly bound molecule where the coherence is easier to achieve due to the smaller energy difference. Afterwards, the molecule can be driven to the rovibronic ground state more quickly, relaxing the coherence requirement. See section 7.4 for a more detailed and systematic description of the challenges and the selection of the transfer pathway.

So far, most experiments implemented the first step by magnetoassociation using a magnetic Feshbach scattering resonance [64, 67]. The only exceptions are Sr_2, where narrow-linewidth (≈ 20 kHz) excited states are available and optical association can be driven coherently [83, 84] and $^{87}Rb^{85}Rb$, where the molecular states with $1 \sim 2$ MHz binding energies allow the use of microwave association [68]. With these requirements, molecules involving non-magnetic atoms or atoms without narrow intercombination lines remain difficult to

associate.

In our experiment, we propose a different method using only optical transitions and does not rely on a narrow excited-state linewidth. This is enabled by the confinement of the optical tweezer and careful selection of the transition pathway, which will be covered in more detail in later chapters. We believe the approach we demonstrate in our experiment is more general than the previous ones, and can be applied to most other molecules created from laser-coolable atoms.

0.2.2 EXPERIMENT PLAN

The molecule we use to implement this approach is NaCs. We selected a bialkali molecule in order to take advantage of the wide range of existing techniques developed to cool and manipulate alkali atoms. The molecule is also expected to have a large molecular fixed-frame dipole moment (4.6 Debye) [85, 86] in the singlet rovibronic ground state, making it a good candidate to demonstrate interaction and entanglement after being created in the tweezers.

The steps we propose to create the molecules in the tweezer are shown in Fig. 1 and are listed as follows,

1. Loading and cooling of single atoms in the tweezers.
   This is the step that gives us the full quantum control on the atoms which will be transferred to the molecules later. Image of the atoms taken in this step can be used to rearrange the tweezers to achieve a high filling fraction.
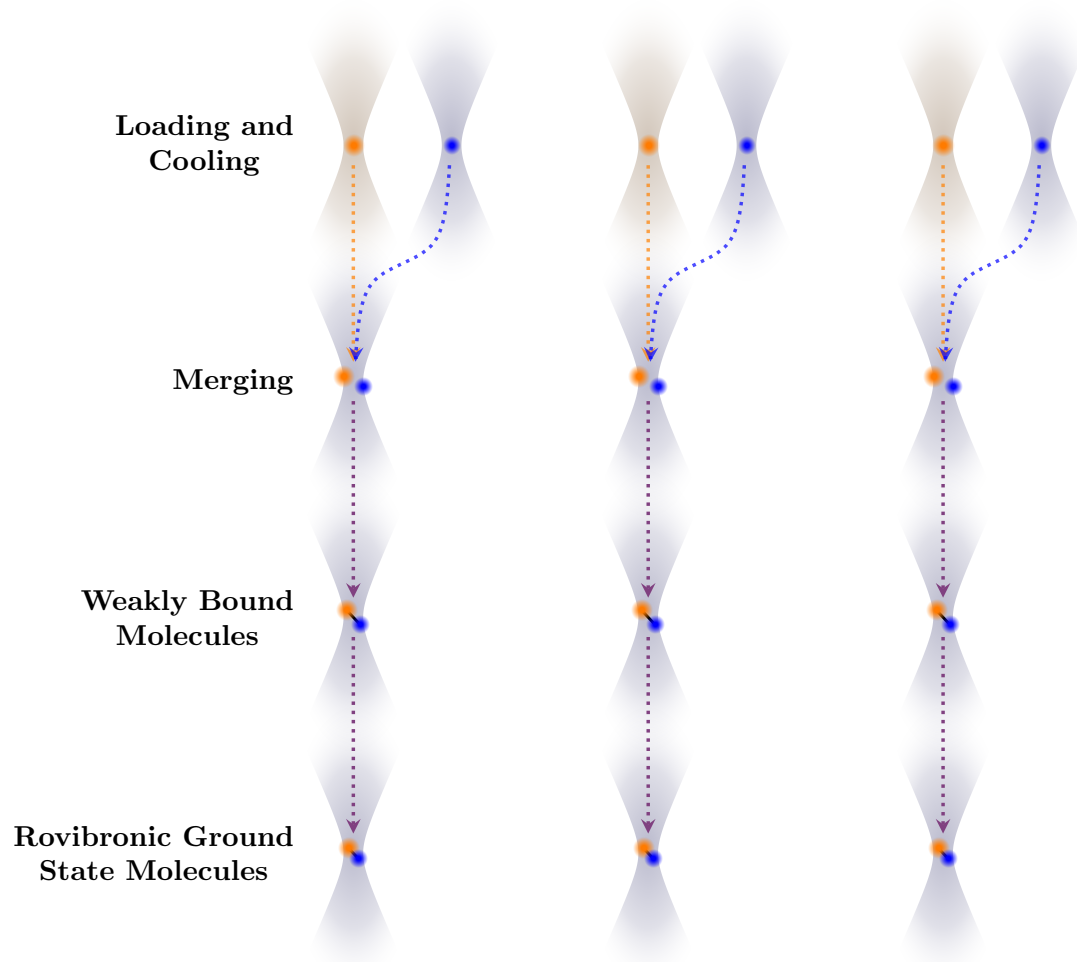
Figure 1: Steps to create single rovibronic ground-state molecules in optical tweezers.

2. Merging of the atoms into a single tweezer.
   Using the precise control of the atoms from optical tweezers, we can merge a single Na and Cs that is trapped and cooled in separate tweezers into a single one deterministically.

3. Creation of weakly bound molecules.
   The pair of atoms in a single tweezer will be coherently associated to a weakly bound molecule using a Raman transition detuned from an excited molecular state. This is the critical step that transfers the control we achieved on the atoms to molecules and will be the main result of this thesis.

4. Creation of rovibronic ground-state molecules.
   Finally, the weakly bound molecule will be driven to the rovibronic ground state using another two-photon transition [87]. This step prepares the molecule in a state with strong dipole interaction and can be used for many previously mentioned applications.

0.3 Contents of this Thesis

In this thesis, we describe the method we use to create a weakly bound ground-state molecule in the optical tweezer and the results leading up to it including the control of atoms and the measurement of the interaction between the atoms and the molecular potential.

Chapter 1 gives a high level description of the custom computer control system we use. This system controls the timing of all the hardware outputs in the experiment and is used to perform all the measurements in the rest of this thesis.

Chapter 2 discusses the loading of the single atoms into the optical tweezer. The discussion includes the preparation steps needed before the loading, e.g. freespace cooling of atoms, and the imaging of the atom in the tweezer, which is the primary detection method used in our experiment. All the experiments in the following chapters are performed using the atoms and molecules in the optical tweezers.

Chapter 3 describes the Raman sideband cooling (RSC) process we used to cool a single Na atom in the optical tweezer. As the lighter atom with a broader optical linewidth, the RSC of Na atom faces additional challenges compared to atoms that were previously cooled using RSC. The tool we developed to overcome these challenges can be applied to other systems as well.

After preparation of the atomic state, chapter 4 starts our investigation of the interaction between atoms by measuring the s-wave scattering length using interaction shift spectroscopy. The measurement result is used to refine the prediction for the Feshbach resonance between Na and Cs atoms and also to improve the atomic state preparation.

Chapter 5 discusses the measurement of the molecular excited states by photoassociation spectroscopy. We also study the effect of the tweezer beam on the molecular states and transitions. The states mapped out in this measurement are used as intermediate states to study the ground molecular states via two-photon transitions.

Following the previous chapter, chapter 6 discusses the properties of the weakly bound

ground molecular states using Raman spectroscopy. We demonstrated the ability to control the rotational states of the molecule and studied the coupling of the molecule with the external field and its hyperfine structure in the weakly bound regime. The measurement identifies candidate target states for our coherent molecule creation.

Chapter 7 combines the preparation and characterization in the previous chapters and describes our all-optical coherent molecule formation process. A detailed comparison between different approaches and selection of states is given to support our choice of experimental parameters. We show our result on the coherent transfer and characterize the molecule we create and the transfer process. We study the limit on the transfer efficiency and list open questions in the transfer process as well as possible future improvements.

1

Computer Control of the Experiment

1.1 INTRODUCTION

The experiment sequence and data taking is managed by computers. In addition to controlling the timing and the actions during a sequence, the computer control system is also the main interface between the people running the experiment (the user), the data and the hardware performing the manipulation and measurements. Because of its central role in

the experiment, it has to satisfy many requirements so that the daily operation of the lab can be performed smoothly and reliably.

1. Full control and utilization of hardware.
   The control system is a layer in between the user and the hardware and will abstract and manage the hardware on behalf of the user. However, the abstraction must still allow the user to take advantage of the full capability of the hardware, e.g. output resolution, timing accuracy etc. This is because there is usually little margin between the capability of the hardware and the requirement in the experiment as the specification of the hardware is often selected based on the requirement to begin with.

2. Usability for all lab members.
   The lab is operated by users with specialty in physics rather than computer science. Although some basic knowledge of computer programming is required for operating the experiment as well as analysing data, the computer control system must be fully usable by people without any experience in building complex software systems. The inevitable complexity of the system must be fully hidden from the user for normal operations although more direct control may still be allowed in certain cases.

3. Modeling of the sequence and scan.
   As an important special case of usability, the computer control system must provide an description for each task close to the users' mental model. More concretely, this means creating abstraction for concepts typically used to describe the task and allow operation on these abstractions matching the users' expectation. We will talk about concrete examples of this requirement in section 1.2 regarding the sequence frontend and section 1.4 regarding scan automation.

4. Reproducibility.
   When exploring something new in the experiment, trial and error is the standard method and troubleshooting is a major part of the process. The ability to do this effectively requires a high degree of reproducibility of all the results. While it is impossible and also not the job of the computer control system to eliminate all the fluctuations and noise in the experiment, it should not add to the randomness of the

system. With few exceptions, identical user input should produce identical output from the control system.

5. Version control.
   Related to and complementing the reproducibility requirement, we must be able to revert to a previous software configuration at a later time in order to reproduce and double-check an earlier result. The use of a proper version control system on the settings and code for the computer control system can allow this with additional features including easy visualization of setting change and parallel development of code by multiple users.

The design of the computer control system is mainly guided by these requirements. In the next sections, we will go into more detail as we describe each part of the system. The application programming interface (API) provided for sequence and scan programming are mostly text based due to the flexibility and version control requirement. Some graphic user interfaces (GUI) are also included for specific tasks built on top of the text interface but will not be covered in this chapter.

The core of the system is divided into the frontend and the backend as shown in Fig. 1.1. Section 1.2 will cover the frontend of the system which is used by the user directly to specify an experimental sequence. Section 1.3 will discuss the backends, which implements the support for various hardware used to run a sequence. After that, section 1.4 describes how multiple sequences can be put together to form a scan and section 1.5 discusses some planned updates to the system.
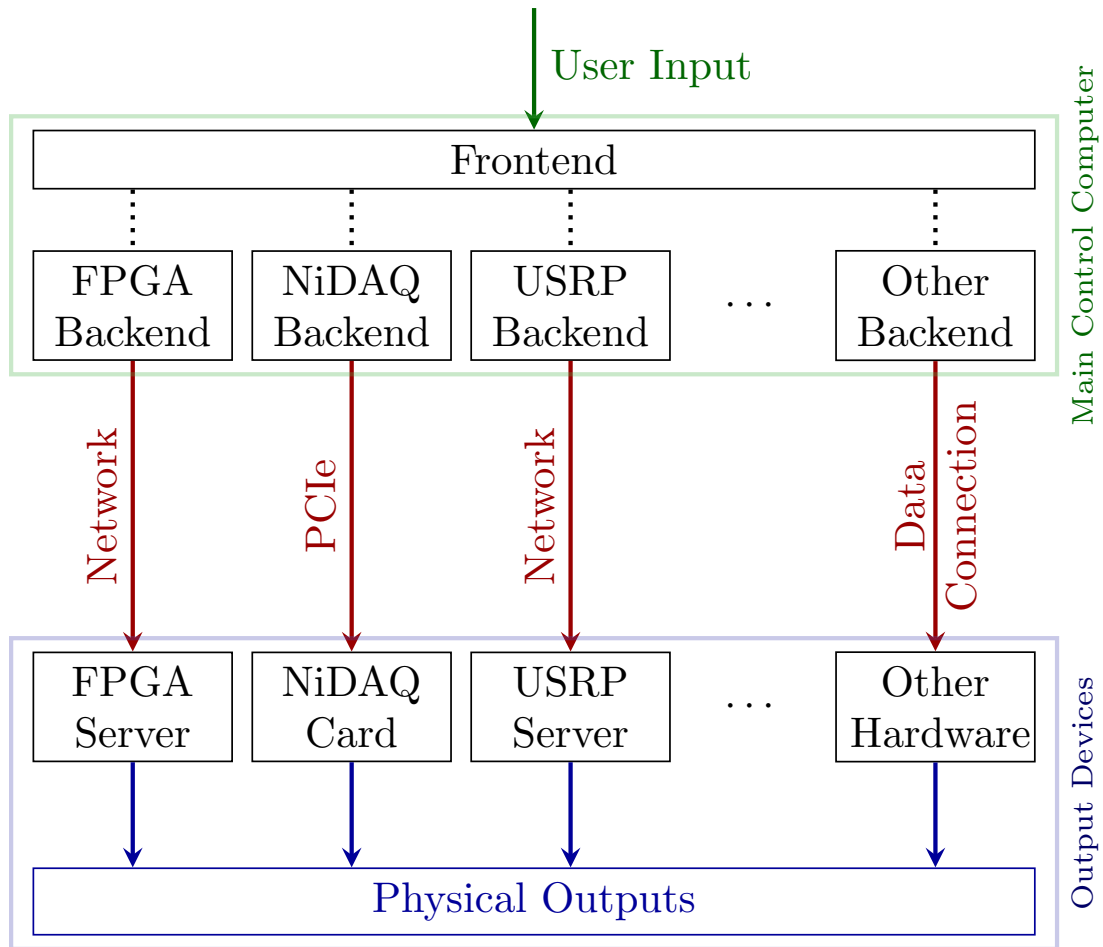
Figure 1.1: Core architecture of the computer control system. The frontend takes the user input and passes it on to different backends. The backends apply the necessary data conversion before sending it to various output devices.

The frontend is the main user interface of the system to specify a sequence. Its API is designed around a few concepts that can be divided into two categories,

1. Timing

   (a) (Sub-)sequence
      This represents a series of events that has fixed relative timing. Sequences can be nested in other sequences with specific time offsets, in which case they are called subsequences. Each sequence can only have at most one parent sequence (the top level one has none) and zero or more subsequences so that all the subsequences in a top level sequence form a tree.

   (b) Time step
      The time or time period in the sequence when one or more events may happen is called a time step. Each time step has a length and a position within a unique parent sequence and are always the leaves on the sequence tree.

2. Output

   (a) Channel
      Each device that can generate an output is abstracted into one or multiple channels that each output a single number. The abstraction depends on the type of the device, e.g. voltage value for a digital to analog converter, or frequency and amplitude for a computer-controlled sine-wave generator.

   (b) Pulse
      This represents the actual output for a particular channel. The pulse itself does not contain the timing information within the sequence, i.e. start and end time. Instead, each pulse belongs to a unique time step that specifies the timing.

Operations on concepts in one category are usually independent of the other which allows most common modifications to the sequence to be done with minimum code change, including,

1. Adding/removing/changing the length of time step or subsequences without affecting the relative timing or output in other parts of the sequence.

2. Enabling/disabling output or changing output values without changing the time and length of the output.

The sequence programming uses MATLAB as the host language. Despite not the best choice from the feature or performance aspect, it offers the following desired properties,

1. Text based language and therefore easier for version control.

2. Familiarity for physics students.
   MATLAB is often used for simulation and data processing. It is one of the few languages that most new students will be familiar with.

3. Built-in feature-rich integrated development environment (IDE).

4. Foreign function interface (FFI).
   Other parts of the system needs to be implemented in other languages for various reasons including higher performance. It is important that we can call into other languages to allow such a hybrid implementation.

5. Good enough feature set.
   MATLAB provides data structures like arrays and hash tables as well as handle classes with object identity which are important to handle the representation of the sequence. It also has a good enough object-oriented programming (OOP) model and operator overload functionality which can simplify the API syntax for the user.

1.2.1 Channel Naming

Each output channel has a unique name attached for identification. This name is always a string of the format `<device_id>/<channel>` where `<device_id>` is a name for the (physical) device and `<channel>` is an identification of the channel within the device. The `<device_id>` may not contain "/" but neither `<device_id>` nor `<channel>` has globally predefined meaning and are completely up to the backend to define. This format allows maximum freedom for the backend to abstract its function into multiple channels in the most fitting way, while allowing the generic code to identify the device, and therefore backend, needed without fully interpreting the channel name.

1.2.2 APIs

The system provides the following APIs for sequence creation that are subject to strict backward compatibility requirements. The most important APIs are listed in this section. Fig. 1.2 provides a short summary of all the classes and methods mentioned in this section.

1.2.2.1 Timing

Subsequences are represented by the `ExpSeqBase` class and time steps are represented by the `TimeStep` class. Both `ExpSeqBase` and `TimeStep` are subclasses of `TimeSeq`, which represent an arbitrary node on the sequence tree.

Class `TimeSeq`

Methods:

- `setTime(time_point, time_ratio=0, offset=0)`
  Set the time for a `TimeSeq` with unspecified time
  (added with `addFloating`).

Class `ExpSeqBase`

Properties:

- `curTime`
  The time within the sequence where
  the next step will be added by
  "default".

Methods:

- `addStep(<time_params>)`
  Add a step or subsequence at `curTime`
  and forward `curTime`. Returns
  `TimeSeq`.

- `addBackground(<time_params>)`
  Add a step or subsequence at `curTime`
  without forwarding `curTime`. Returns
  `TimeSeq`.

- `addAt(time_point, <time_params>)`
  Add a step or subsequence at
  `time_point` without updating
  `curTime`. Returns `TimeSeq`.

- `addFloating(<time_params>)`
  Add a step or subsequence at
  unspecified time without updating
  `curTime`. Returns `TimeSeq`.

- `wait(t)`
  Wait for time `t`.

- `waitAll()`
  Wait for all children `TimeSeq` to finish.

- `waitBackground()`
  Wait for all `TimeSeq` added directly via
  `addBackground` to finish.

- `waitFor(seqs, offset=0)`
  Wait for `seqs` to finish.

- `totalTime()`
  Returns the total length of the
  sequence.

Class `TimeStep`

Methods:

- `add(channel_name, output)`
  Generate `output` on
  `channel_name`.

Class `TimePoint`

Constructor:

- `TimePoint(seq, time_ratio, offset)`
  Create a `TimePoint` corresponding to a time
  within `seq` (class `TimeSeq`).

Figure 1.2: Frontend class inherit diagram and API lists.

18

Most timing related APIs are methods on `ExpSeqBase`. The most important ones are the ones creating new branches in the subsequence tree, i.e. `TimeSeq`. The type of branch created is determined by the parameters passed in (`<time_params>`), which can be either

1. `length, offset=0`
   This creates a new `TimeStep` with a numerical `length` and an optional time `offset` from an API dependent time reference point (see list of APIs below).

2. `offset=0, callback, <callback parameters>`
   This creates a new `ExpSeqBase` with an optional time `offset` the time reference point. The new subsequence will be populated by calling `callback` with the new sequence followed by `<callback parameters>`.

Since most sequences are built in series, `ExpSeqBase` maintains a current time (`curTime`) of the sequence. Various methods are provided that each act differently with respect to `curTime`.

1. `addStep(<time_params>)` method
   This is the most used method to construct the sequence in series. The time reference point is `curTime` and `curTime` will be set to the end of the time step or subsequence created. A check is made to ensure the `curTime` only moves forward and errors if a too negative `offset` large enough in magnitude is specified. This ensures that what is added with `addStep` always appears in the final sequence in the same order as the program execution order which makes the code easier to reason about.

2. `addBackground(<time_params>)` method
   The time reference point is `curTime` and no change to `curTime` is made.

3. `addAt(time_point, <time_params>)` method
   The time reference point is specified by `time_point` which is of type `TimePoint`. See below about `TimePoint`.

19

4. `addFloating(<time_params>)` method
   The time reference point is unspecified. The optional `offset` parameter cannot be specified in `<time_params>`. The time reference point, however, must be specified before the sequence can be run. This can be done by calling the `setTime(time_point, time_ratio=0, offset=0)` method on the `TimeSeq` object returned, where `time_point` is also of type `TimePoint` described below. The optional `time_ratio` specifies the relative time within the subsequence or time step to set the time for where a value of 0 sets the start time and a value of 1 sets the end time.

All methods return the new `TimeSeq` constructed so that they can be operated on.

The `TimePoint` object used in `addAt` and `setTime` can be constructed via `TimePoint(seq, time_ratio, offset)` which represents the time within the sequence or step `seq` with a time `offset`. `time_ratio` specifies the time within the `seq` where 0 is the start time and 1 is the end time.

Due to the support of background steps, the `curTime` of the sequence may not reflect its total time. The `totalTime()` method can be used to obtain the current total length of a sequence that includes the time it takes to finish all (nested) subsequences.

Additional convenience methods for `ExpSeqBase` are also provided to manipulate `curTime`,

1. `wait(t)` method
   Add `t` to `curTime`. This is the only method that can change `curTime` backwards.

2. `waitAll()` method
   Forward `curTime` to the end of all (nested) subsequences and time steps within the current subsequence. This is equivalent to assigning `totalTime()` to `curTime`.

3. `waitBackground()` method
   Similar to `waitAll()` but only wait for the subsequences and time steps directly added to the current subsequence.

4. `waitFor(seqs, offset=0)` method
   Forward `curTime` to the end of subsequences and time steps specified within the array `seqs`. An optional `offset` may be added to the latest end time.

1.2.2.2 OUTPUT

As mentioned before, all the outputs are specified on time steps which are represented by the class `TimeStep`. This is done via a single method `add(channel_name, output)` on `TimeStep`. The `channel_name` is the channel name described above and `output` specifies the output in one of the following ways,

1. A number
   This represents setting the channel to the specified value at the start time of the pulse.

2. A function or callable object
   The function will be used to compute the value to output over the whole duration of the pulse. It will be called with arguments (`t`, `len`, `old_val`) where `t` is the time within the pulse, `len` is the length of the pulse and `old_val` is the previous value of the channel before the current pulse.

Putting both the timing and output APIs together, here is an example sequence that uses most of the features mentioned above. The comments `s.curTime == x`, `s.totalTime () == y` shows the current value of curTime and sequence length at each point in the code.

```
% `s.curTime == 0`, `s.totalTime() == 0`
s.addStep(1) ... % Create a step with length 1
  .add('CH1', 1) ... % Set CH1 to 1 at t=0
  .add('CH2', @(t) 2 * t); % Ramp CH2 from 0 to 2 over t=0 to t=1

% `s.curTime == 1`, `s.totalTime() == 1`
step1 = s.addBackground(1) ... % Create a step with length 1
  without changing `curTime`
  .add('CH2', 0); % Set CH2 to 0 at t=1

% `s.curTime == 1`, `s.totalTime() == 2`
step2 = s.addBackground(2) ... % Create a step with length 1
  without changing `curTime`
  .add('CH1', @(t) 1 - t); % Ramp CH1 from to 1 to -1 over t=1 to t
  =3

% `s.curTime == 1`, `s.totalTime() == 3`
s.waitFor({step1, step2}); % Wait for both background steps to
  finish
% This can also be achieved with one of the following
% s.waitAll();
% s.waitBackground();
% s.wait(2);

function subseq(s2)
  % Function to create a subsequence
  % `s2.curTime == 0`, `s2.totalTime() == 0`
  s2.addStep(5) ...
```

```
      .add('CH3', @(t) -t); % Ramp CH3 from 0 to -5
   % `s2.curTime == 5`, `s2.totalTime() == 5`

   % Note that `s.curTime` is not directly affected
   % while the subsequence is being constructed by the `subseq`
   function.
end

% `s.curTime == 3`, `s.totalTime() == 3`
s2 = s.addFloating(@subseq); % Create a floating subsequence
s.setTime(TimePoint(s, 0, 0)); % and add it to the beginning of `s
   `.
% Equivalently:
% s.addAt(TimePoint(s, 0, 0), @subseq);
% `s.curTime == 3`, `s.totalTime() == 5`
```

1.3 Backends

As discussed in section 1.2, the frontend provides an API to program all the output chan-

nels in the same way no matter the type of the channel or device used. However, this is not

the case for the devices generating the output which often have an API specifically designed

for the device that may be very different from one another. Moreover, the frontend rep-

resents the sequence as a tree structure that is convenient for manipulation whereas the

device API typically uses a flat data structure like an array of numbers or a series of com-

mands. It is therefore the job of the backend to bridge this gap and convert between the

multiple representations of the sequence. The conversion is done in a "generation" step

and the result is cached for each sequence to allow running the sequence multiple times

with minimum overhead.

The specific requirements and implementations for each backend are very different. Nevertheless, there are a few important features or components that are shared among different backends.

1.3.1 Network Communication

With one current exception, the output devices are not directly connected to the computer running the frontend but are only connected to another computer on the same network. This requires network communication between the frontend machine and a service running on the device computer to run the sequence.

We use ZeroMQ Message Transport Protocol (ZMTP) as the main protocol for network communication which offers the following advantages,

1. Binary protocol
   The protocol allows us to send and receive arbitrary data without having to encode it into text first. This saves encoding and decoding time as well as network bandwidth which allows higher performance.

2. Feature rich and flexible
   Compared to using sockets for network communication directly, the message oriented protocol allows easy implementation of remote procedure call (RPC). The ZeroMQ library also provides a flexible interface to process the messages which is useful to implement robust handling of failure and parallel processing of requests.

3. Lightweight

Despite the rich feature set, the library is relatively lightweight. This is important because part of the computer control system needs to be executed in an environment with limited resources.

4. Cross platform
   The library is cross platform and provides identical API on different environments. Windows support is particularly important since most of the development is done on Linux machines.

5. Stable
   Both the protocol and the library are stable. The library versions available on different machines are not always the same and it is important that the same version of code can work on different machines and can communicate with each other in all cases.

1.3.2 Sorting of Pulses

The tree representation of the sequence is useful for construction and manipulation but contains unnecessary information for generating output, for which only the pulses and their start and end time within the top-level sequence is important but not the subsequence structure. Because of this, all the backends start the generation step by flattening the tree to obtain a list of all pulses sorted by their start time. After the sorting of the pulses, the tree structure is discarded by default[‡] to reduce memory usage.

[‡]This behavior can be disabled for debugging purposes.

1.3.3 Representation of Pulses

Several backends require accessing the exact representation of the pulses outside the MAT-LAB code and even on different computers. Since the pulses can be arbitrary functions, this requires the ability to package the code in a format that can be transferred over the network, i.e. serialization, and to restore the code for execution from this format, i.e. deserialization.

In order to do this, we developed a simple intermediate representation (IR) of the code that runs on a register-based virtual machine. The IR supports three different data types, `Bool`, `Int32` and `Float64` and basic arithmetic, control flow and math functions that are sufficient for specifying pulse shapes. The IR can be interpreted by an interpreter written in C++ or be compiled and optimized to native code for faster execution using an LLVM based compiler.

In order to convert MATLAB functions specified in the sequence to the IR, we pass in a special object as the input argument to the MATLAB function. Supported operations on this object will return a new object that records the operation as well as input arguments. The value returned from the function is therefore an object representing all the operations needed to compute the result as a directed acyclic graph (DAG). We then convert each node in the DAG to an IR instruction to finish the conversion. This process only supports pure functions. Conditional branching is supported via an `ifelse` function that returns one of
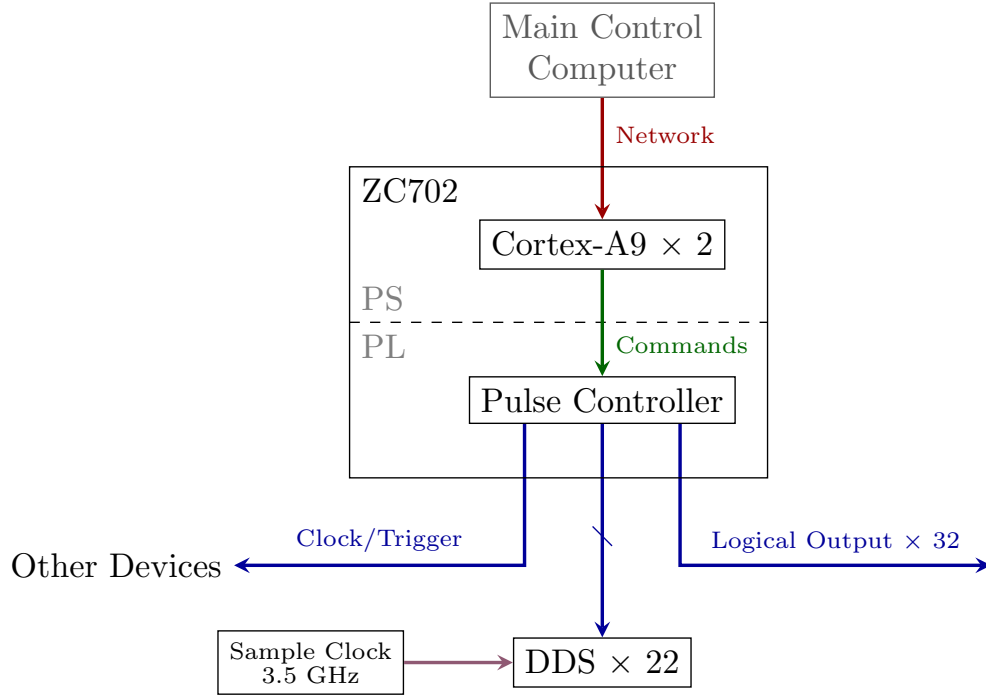
Figure 1.3: FPGA hardware block diagram. The sequence data is sent to the server program running on the CPU through the network. The program then pushes the commands to the pulse controller implemented in the programming logic. The pulse controller executes the commands and generates or changes the outputs for clock/trigger, DDS or logical outputs. The DDS chip uses an external 3.5 GHz clock (section A.2)

the input arguments based on a condition. Loops are not currently supported.

1.3.4 FPGA Backend

The timing of the experiment is controlled by a Xilinx ZC702 FPGA which contains both

a processing system (PS) part, i.e. CPU, and a programmable logic (PL) part, i.e. FPGA (Fig. 1.3).

The PL creates digital control signals for various peripheral devices which generate the out-

puts for the experiment, including direct digital synthesizers (DDS), logical switching signal

and clock or trigger signal for other devices. The PS consists of a dual core Cortex-A9 CPU

which runs an Arch Linux ARMv7 distribution. The server software that runs on the PS communicates with the main control computer via ZeroMQ (section 1.3.1) and generates a custom command stream to control the PL output. Each command corresponds to making one change to the final output, e.g. logical values, DDS output amplitudes or frequencies, etc. The main job of the FPGA backend is therefore to convert the sorted pulses to the command stream. See appendix A.1 and A.2 for more information about the hardware specification.

Due to performance concerns, this conversion is done in C++ code[‡]. The main design considerations and features are,

1. The sequence supports changing and ramping multiple channels at the same time. This is not supported by the hardware due to the limit on the number of I/O ports connecting the PL to the output devices requiring multiplexing of the control signal. The backend manages this by interleaving the commands for different channels when more than one channel is changed at the same time. A set of active pulses is maintained as the conversion proceeds through the sequence time. Pulses are added to the active set when the start time is reached and retired from the set when the end time is reached.

2. For a continuous ramp of a channel, since the output changes are discrete, it may not happen at exactly the end time of the pulse which requires special care to ensure the correctness of the channel value after a pulse. For example, a linear ramp from 0 to 0.5 on a channel from time 0 μs to 5 μs may only receive updates at times 0, 2, 4 μs with values 0.0, 0.2, 0.4 respectively due to discretization. However, the user should expect the value of the channel (in the absence of other pulses) long after the pulse to be 0.5. This is handled in the backend by checking the last update from the pulse

---

[‡]https://github.com/nacs-lab/libnacs/blob/0076e347ff3ba674fbf74872883b40feefd82ce0/lib/seq/bytecode.cpp#L528

28

against its expected ending value before retiring it. A final update to the ending value is generated if the two values are different.

3. The output has finite resolution. If an update changes the value that is unresolved by the hardware (typically during a slow ramp), the update will be omitted.

4. Some commands correspond to more than one action/pulse in the sequence. For example, more than one logical output can be updated at the same time and some commands also accept a variable wait time afterwards (in addition to a special purpose wait command). The backend examines neighboring operations and may merge multiple commands into one. This is especially useful for logical outputs. In fact, logical output changes that are specified to happen at the same time in the sequence are guaranteed to happen at the same time in the experiment as well.

5. The PL commands are fixed length to allow a simpler implementation of command parsing in the PL. However, since not all commands contain the same amount of information, some include padding for alignment. In order to save network bandwidth, a compressed format with variable command length and no padding is used to transfer the commands through the network. The decompression is done when running the sequence on the CPU right before sending to the PL for execution.

1.3.5   NiDAQ Backend

For outputting slowly varying voltage signals, we use a DAQ PCI card (more detail in appendix A.3). The software driver for the card accepts an array of numbers as the voltages to output at each clock cycle for each of the channels. Since the values in these arrays can be computed for each channel independently, the logic for generating them is relatively straightforward.

The API for the card is designed for updating the outputs at regular intervals. However, there are a few issues when it is used this way,

1. The same sampling rate is used when frequent updates to the output are needed and when the outputs are held at a constant value.
   Since output voltages are usually only being varied for a short time compared to the length of the sequence, this causes significant duplication in the data causing a waste of memory.

2. We measured voltage noise at the refresh rate when the output is held constant by outputting samples at the same value.
   While this is a hardware limit that cannot easily be fixed when the values are changing, being able to turn off the refreshing gives us control to minimize its effect on the experiment.

Because of these issues, we control the refresh by gating the clock input to the output card. When there are channels to be updated, the clock is turned to the maximum speed. Otherwise, the clock is kept off so no refreshing is happening. Since the clock signal is generated by the FPGA, the gating is done by passing the clock on/off intervals computed by the NiDAQ backend to the FPGA backend. Since an extra or missing clock cycle may cause the output value during hold time to be significantly different from the desired value, the FPGA backend guarantees that the clock control commands are always scheduled at the exact time so that the exact number of clock cycles can be sent to the output card.

We also observed that the driver of the card may timeout if not enough clock signals are received at the beginning of the sequence. We therefore always send 1 ms of clock signals to the card at the beginning of the sequence to work around this issue.

1.3.6 USRP Backend

In addition to the DDSs attached to the FPGA, we also support generation of radio frequency (RF) signals using universal software radio peripheral (USRP) (more detail in appendix A.3). Compared to the DDS, which can only output a single frequency at a time, USRP supports the output of arbitrary spectra within a certain range. This can be useful when more than one frequency is needed on a single channel, e.g. for fast modulation of the amplitude using beating, or to generate multiple diffraction orders on an acousto optical beam deflector (AOBD).

Since most usage of the USRP output involves creating multiple discrete frequencies, the hardware is modelled in our system accordingly. Instead of mapping the physical output channel to a fixed number of parameters similar to all the previously mentioned backends, a "virtual" output channel is created for each tone in the output, and can be controlled independently similar to all other channels. The `<device_id>` component of the channel name has format `CH<n>/<param>` where `<n>` is a number identifying the virtual channel and `<param>` is the parameter controlling the virtual channel, e.g. `FREQ` for frequency or `AMP` for amplitude.

The driver API for USRP is very similar to that of the NI output card and requires the output value to be provided at a regular time interval. However, due to the constant changing nature of the RF output and the higher sampling rate, the memory requirement would

be too high if we take the same approach as the NiDAQ backend and compute all the output values before the sequences start. Instead, the backend uses a command stream similar to the one used by the FPGA backend to encode the change to the output spectra. Unlike the FPGA backend, however, commands can be issued for all the virtual channels simultaneously, removing the need to interleave updates for different channels.

From the command stream, we generate the output at a sampling rate of 50 MS/s. The samples are computed on the fly which allows maximum flexibility and minimizes the time needed to generate the data before each sequence. The data throughput necessary to generate samples at the high rate is achieved thanks to the AVX2 instructions, which allows computation of multiple sine and cosine functions simultaneously[‡]. In order not to interfere with the user interface tasks and to achieve more reliable performance for the sample generation, the program directly managing the USRP device runs on a separate computer running Linux. The communication with the main computer is done via ZMTP.

The USRP device does not have built-in support for triggering, which is necessary to synchronize its output with other devices. We implement this in software by converting the trigger signal to a COM port signal using an Arduino board and monitoring the COM port in the USRP server program. The trigger has a timing accuracy of 1 ms which is limited either by the timing of the Arduino or the reading of the COM port on the server com-

---

[‡]The AVX2 implementation of the math functions used is based on work by Yu Yang at https://github.com/reyoung/avx_mathfun which is based on work at http://software-lisc.fbk.eu/avx_mathfun/ by garberoglio@fbk.eu.

puter.

1.4 Automation of Scans

The core of the control system, as described in the previous sections, deals with the specification and realization of experimental sequences, which are the building blocks for all measurements we do. However, most experiments require running multiple sequences to reduce statistical uncertainty and measure the effect of varying certain parameters. We add the concept of scans to the system in order to satisfy this requirement. A scan is a set of sequences where one or more experimental parameters are varied across the sequences. When running the scan, the system automatically selects sequences from the scan to run in random order in order to reduce potential systematic effects due to interference between sequences. The scan can be configured to run for a set number of times or until some predetermined conditions are satisfied, which in our experiment typically happens when a certain number of single atom loading events happens.

The scan interacts with the sequence constructing code by storing the parameters for the scan in the sequence object `s` as a nested structure, which is accessed as `s.C`. Each substructure within the parameters can be accessed and passed independently which allows multiple instances of a common subsequence to store their parameters in the same way within the parent structure. As an example, a subsequence construction function may be

33

implemented as

```
function subseq(s, p)
  % Access `parameter1`, with default value 0
  parameter1 = p.parameter1(0);
  % Access `parameter2`, which must be predefined
  parameter2 = p.parameter2();
  % ... Use `parameter1` and `parameter2` to construct s.
end
```

which may be used in the parent sequence as

```
% Construct one instance of the subsequence
% using substructure under Instance1
s.addStep(@subseq, s.C.Instance1);
% ...
% Construct another instance of the subsequence
% using substructure under Instance2
s.addStep(@subseq, s.C.Instance2);
```

We will show examples of how this sequence can be scanned below.

The scan is represented by a `ScanGroup` object, which can store multiple basic scans each containing a multiple dimensional scan (see below) of parameters. The basic scans within a `ScanGroup` `sg` can be accessed through indexing, e.g. `sg(1)`. Multiple `ScanGroup` `sg1`, `sg2`, `sg3`, or the basic scans included can be concatenated into a single `ScanGroup` via the concatenation syntax, e.g.

```
[sg1, sg2, sg3(1), sg3(4)]
```

This allows multiple different scans to run simultaneously, which is useful when running the experiment unattended for a long time, e.g. overnight.

The following APIs are provided in order to construct a basic scan. The examples given

below can be used to scan the sequence give above.

- Within a basic scan, the parameter can be set to a fixed value via assignment, e.g.

```
% Within the second basic scan,
% `parameter1` will be `2` in the first `subseq`
sg(2).Instance1.parameter1 = 2;
```

- Each basic scan allows multiple parameters to be scanned simultaneously forming a multidimensional array of parameters. A scan of the parameter along dimension i can be configured by assigning values to .scan(i) of the parameter, e.g.

```
% Scan along the second dimention within the first basic scan
% `parameter2` will be varied between `1, 2, 3, 4`
% in the first `subseq` for sequences within this basic scan.
sg(1).Instance1.parameter2.scan(2) = [1, 2, 3, 4];
```

- Multiple parameters can also be scanned along the same dimension in which case the length of the parameter values must be the same. E.g.

```
% Scan along the second dimention within the first basic scan
% For each sequence within this basic scan.
% `parameter2` will be varied between `1, 2, 3, 4`
% in the first `subseq`. For each of the values,
% `parameter2` in the second `subseq`
% will take the corresponding value from `2, 3, 4, 5`.
sg(1).Instance1.parameter2.scan(2) = [1, 2, 3, 4];
sg(1).Instance2.parameter2.scan(2) = [2, 3, 4, 5];
```

is supported whereas

```
sg(1).Instance1.parameter2.scan(2) = [1, 2, 3, 4];
% Error: must have the same dimension
sg(1).Instance2.parameter1.scan(2) = [2, 3, 4];
```

will raise an error.

- Parameters, fixed or scanned, can be set for all the basic scans in the ScanGroup by assigning to the empty index, e.g.

```
% For all sequences within scan,
% `parameter1` will be `3` in the first `subseq`
% unless overwritten for a specific basic scan.
sg().Instance1.parameter1 = 3;
% Scan `parameter2` between `2, 3, 4` in the first `subseq`
% in all basic scans (unless overwritten)
sg().Instance1.parameter2.scan(1) = [2, 3, 4];
```

1.5 Summary and Outlook

We have designed a computer control system for the experiment that is power and flexible

yet requires minimum low level knowledge from the user. All the measurements done in

this thesis are implemented using this system.

The design of the system, especially the user API, guarantees that continuous improve-

ment can be made without major changes to existing user code. Examples of further im-

provements that could be made to the system include,

1. Unlike other backends, the FPGA determines the timing of the experiment and only
   one instance of such a device is allowed per experiment. This limits the number of
   output channels we can use that are attached to the FPGA (i.e., DDS and logical
   outputs). Allowing the FPGA to use an external clock could make it possible to use
   more than one FPGA in the experiment and thus increase the number of channels
   available.

2. Support for more devices can be added to the system.
   One such update in progress uses the arbitrary waveform generator (AWG) boards
   from Spectrum Instrumentation. These are very similar to the USRP devices but the
   outputs have higher bandwidth and significantly lower noise.

3. The IR execution is one of the main factors affecting the performance of the sequence compilation. In addition to the compilation to native code mentioned previously, the function can also be vectorized to take advantage of SIMD instructions in order to further improve the performance.

4. The sequence is currently static and cannot depend on measured value during the experiment as feedback. Dynamic or runtime logic can be added to the sequence by recording and encoding the necessary logic that needs to happen at runtime in a similar way we convert MATLAB code to the IR. Such capability will be important for implementing rearrangement of tweezers in order to achieve high filling fractions.

2

Loading of Single Atoms in Optical

Tweezer

2.1 Introduction

The atoms we use in the experiment come from alkali metal dispensers heated using an electric current. Thus, these atoms start with a temperature of $\approx 400 \sim 800$ K and must

be cooled to < 0.1 K before they can be captured by the optical tweezer. In this chapter, we will briefly discuss the cooling steps that bridge this temperature gap. In section 2.2, we will focus on the free space cooling on the atoms without involving the optical tweezer. Since most of the cooling techniques used in our experiment are quite standard, they will not be reviewed in detail here. Instead, we will mainly highlight the important design choices and their performance in our experiment. Section 2.3 will discuss the loading and detection of the atom in the tweezer including a short summary of the unique challenge we face with Na atoms. More details about the apparatus, and the cooling and imaging of the atom in free space can be found in Lee Liu's thesis [88].

2.2   Free Space Cooling of Atoms

Our experiment begins with the loading of a Na-Cs dual species magneto-optical trap (MOT) from the background pressure created by two atom dispensers heated using $3.8 \sim 4.0$ A of current. Fig. 2.1 shows the energy diagrams for the two atoms. The MOT is created using six cooling beams of ≈ 4 mm diameter[‡] with $0.5 \sim 0.9$ mW (Na) and $0.3 \sim 0.5$ mW (Cs) power in each beam, which includes 20 % (Na) and 5 % (Cs) of hyperfine state repump light. The resulting atom cloud has a diameter of $0.1 \sim 0.2$ mm with $10 \sim 50$k (Na) and $3 \sim 20$k (Cs) atoms being trapped and cooled to a temperature of ≈ 400 mK (Na) and ≈ 100 mK (Cs). The atom numbers are significantly smaller than the ones typically seen in

---

[‡]ISO 11146 diameter [92, 93]
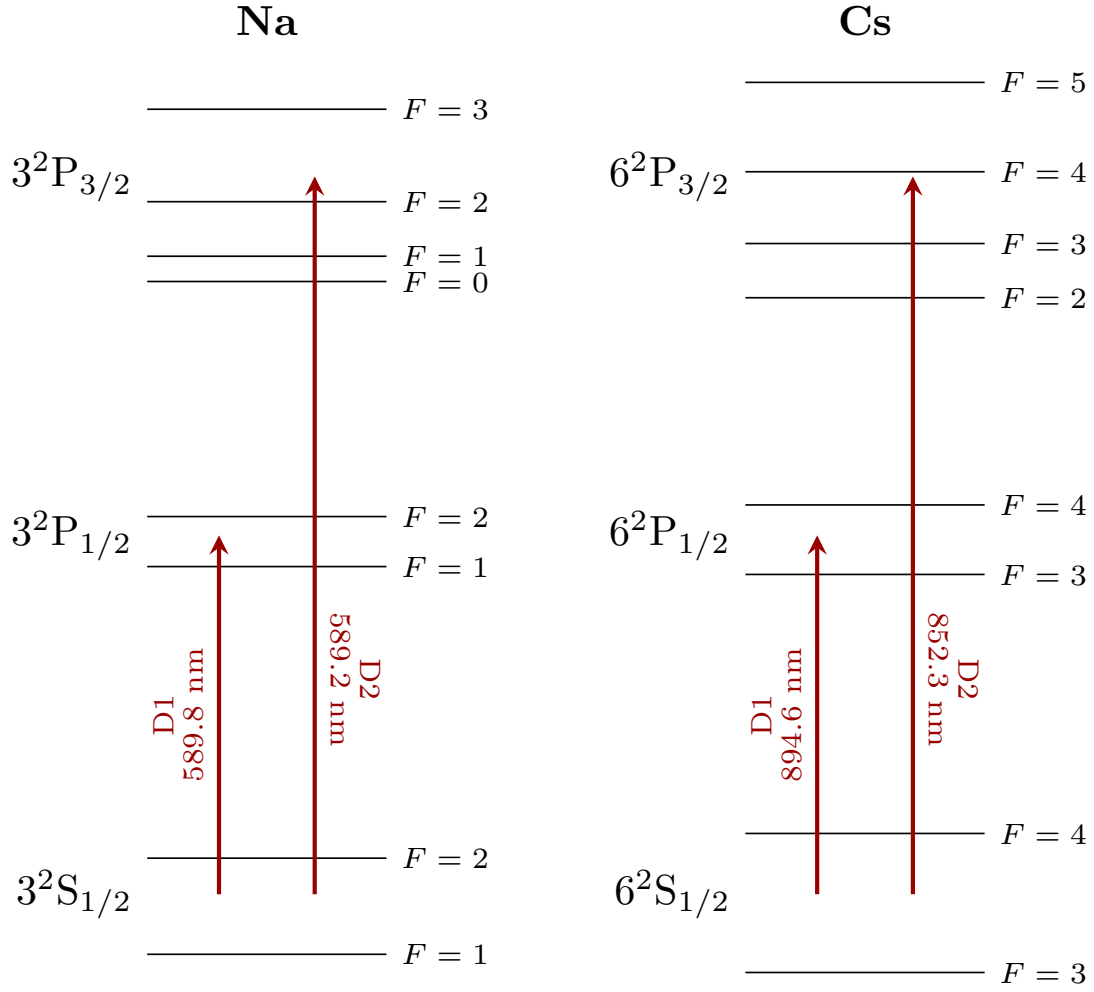
Figure 2.1: Energy diagrams for Na (left) and Cs (right) atoms including fine and hyperfine structures [89, 90]. Most of the cooling, state preparation and imaging steps use the D2 transtion in our experiment with the exception of optical pumping (OP) on the sodium atom which uses both D1 and D2 lines (section 3.2.2).
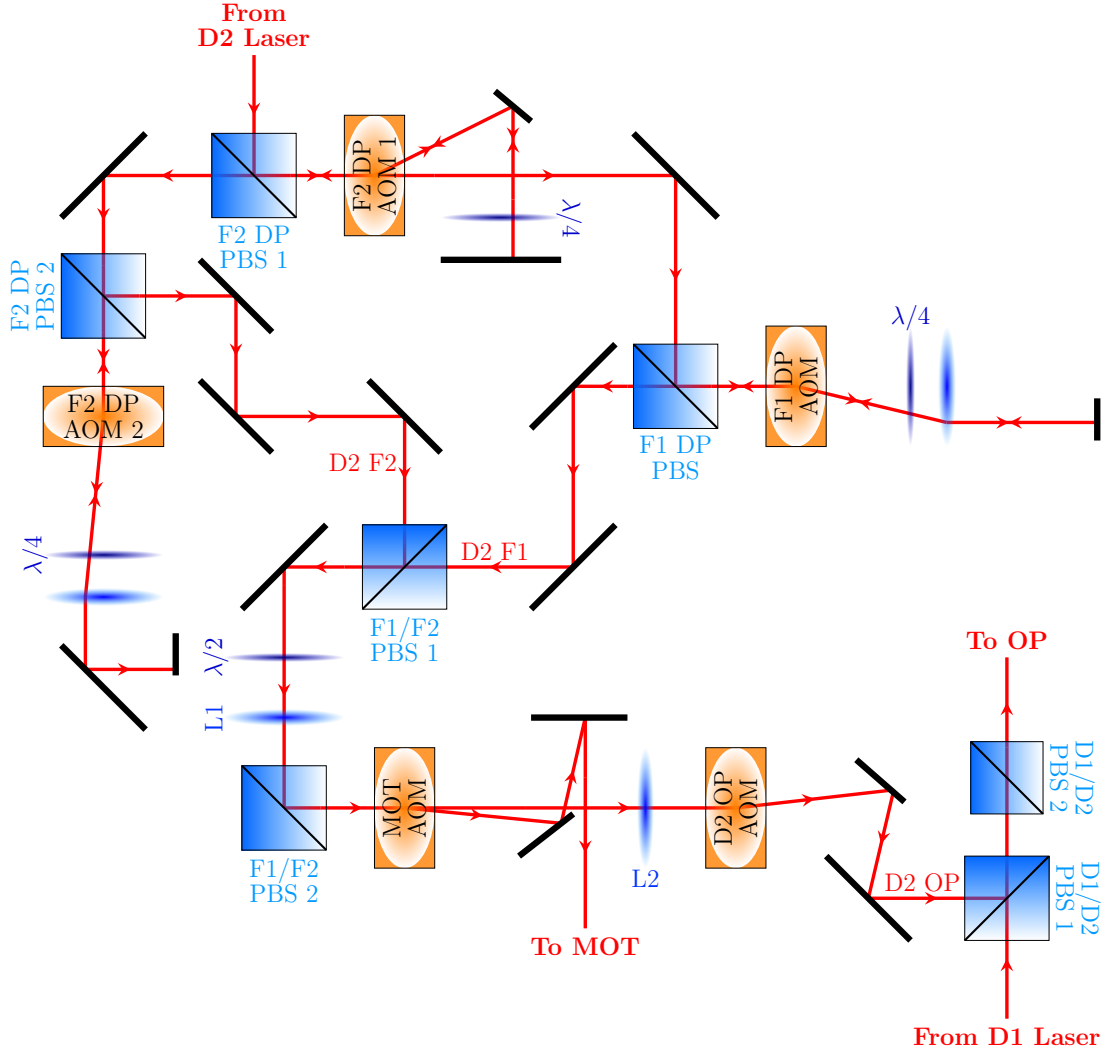
Figure 2.2: Beam path for generating the frequencies for Na MOT and optical pumping (OP). (Beam path for fiber coupling and frequency locking is not shown. The power control for the D1 laser is also omitted.) The D2 laser is locked on the F1/F2 crossover line using saturated absorption locking. It is shifted down by the two F2 double-pass (DP) AOMs to generate the frequency for the Na $F = 2$ state and shifted up by the F1 DP AOM to address the Na $F = 1$ state. The frequencies of the F1/F2 light are controlled by the F1 DP AOM and F2 DP AOM 2 respectively. This set up makes sure that when the F1/F2 DP AOMs are off, the closest frequency in the leaked light is at least detuned by half the F1/F2 separation (≈ 880 MHz) [89] and will have a minimum effect on the atom. The F1 and F2 light are combined on F1/F2 PBS 1 and their power ratio after the F1/F2 PBS 2 is controlled by the half waveplate between the two PBSs. A similar setup is used to combine the D1 and D2 light in the OP output using D1/D2 PBS 1 and the rotating D1/D2 PBS 2. Since we need to switch the Na MOT light on and off out-of-phase with the Na tweezer [91] at a high frequency, the sharpness of the turn on/off edge in the MOT AOM is important. We focus the beam through the AOM using lens L1 to optimize the switching time. This is then collimated by lens L2 for the downstream beam path.
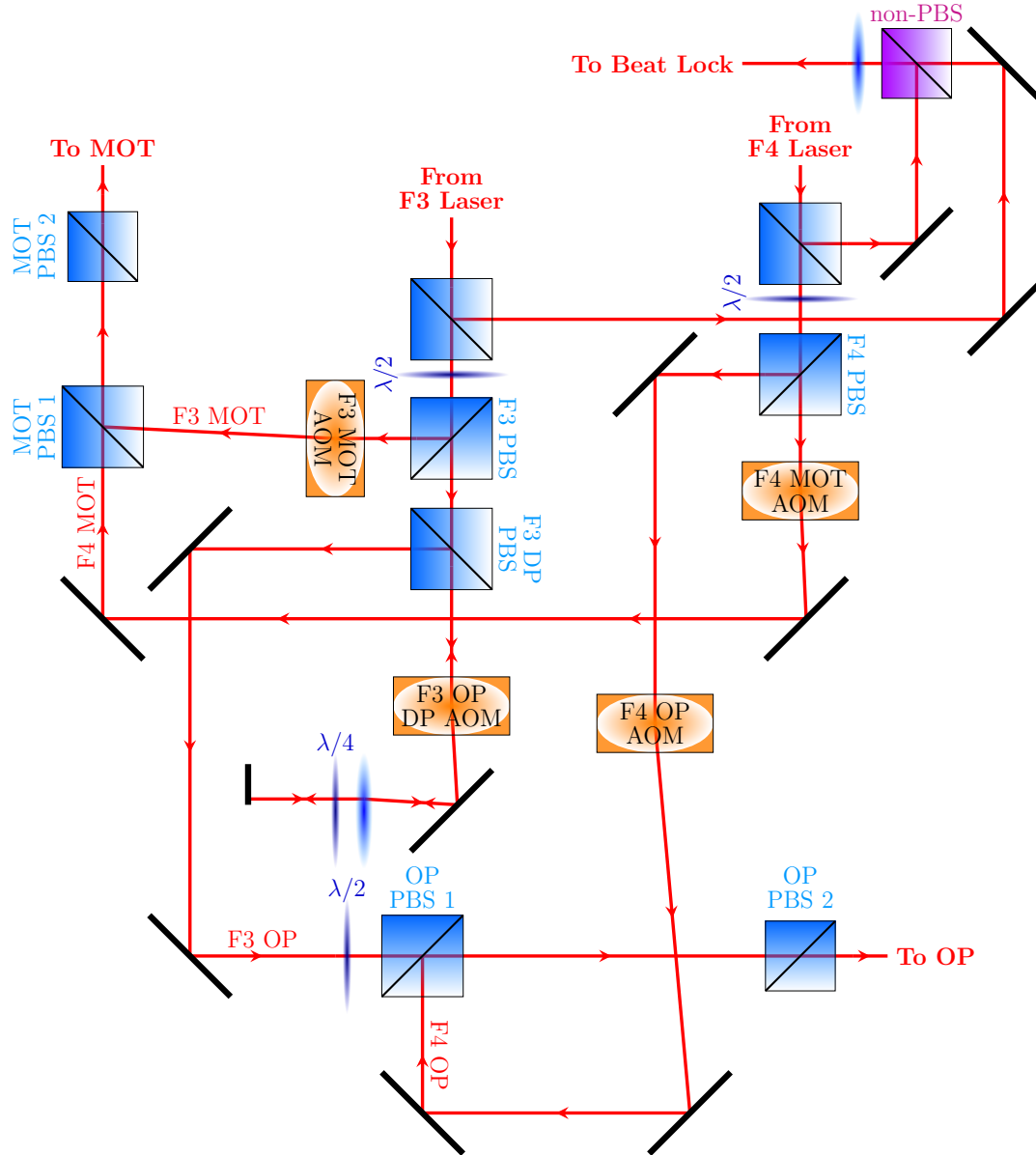
Figure 2.3: Beam path for generating the frequencies for Cs MOT and optical pumping (OP). (Beam path for fiber coupling and locking of the F3 laser to the atomic transition is not shown.) The F3 laser is locked using saturated absorption locking to the F3 atomic transition. The F4 laser is beat-locked to the F3 laser, which also controls its frequency. The F3 and F4 light are combined on MOT PBS 1 and OP PBS 1 and their power ratio in the MOT and OP output are controlled by the rotating MOT PBS 2 and OP PBS 2 respectively. The frequency of the F3 light in the MOT is fixed whereas the frequency of the F3 light in the OP can be changed by the F3 OP DP AOM.

a bulk gas experiment since the goal of the free-space laser cooling is to load atoms into the tweezers which does not require large atom numbers. The small size of the MOT requires a tighter tolerance on the MOT position in order to overlap with the optical tweezer for the loading of single atoms, which in turn increases the sensitivity of the loading to the alignment and power balance of the cooling beams. Because of this, we use four independent fibers to deliver the power for the four horizontal cooling beams which allows independent control of the power and alignment. We observed a more robust MOT and, as a result, single atom loading compared to using retro-reflectors to create counterpropagating horizontal cooling beams. Due to the geometric constraints in the experiment, retro-reflector is used for vertical cooling beams.

The MOT is followed by a compressed-MOT (CMOT) stage for Na which uses light closer to resonant to push the Na atoms closer to the center. After this, the magnetic field is turned off and a polarization gradient cooling (PGC) step is applied on the atoms which cools the atoms to ≈ 80 mK (Na) and ≈ 10 mK (Cs).

The beam paths for generating all the necessary frequencies are shown in Fig. 2.2 (Na) and Fig. 2.3 (Cs). The same beam paths are also used for generating the light for cooling and imaging of single atoms as well as optical pumping for state preparation that will be discussed in later chapters.

We load the tweezer from a laser-cooled cloud of atoms. Since the tweezer provides a conservative potential, trapping of the atom requires its energy to be reduced. This can be done either by changing the trap depth, e.g. turning on the trap when an atom is at the focus to reduce its potential energy, or by a dissipative cooling process. However, due to the low trap volume of the tweezer and the density of the MOT, there is less than 0.01 atom from the MOT in the tweezer, and therefore we need to load the tweezer by cooling the atoms into it. This cooling process also ensures that at most one atom can be loaded into the tweezer due to pairwise loss from light-assisted collisions [73].

Cooling into the tweezer and loading using the free-space cooling beams works well for Cs. However, the cooling of Na atoms in the tweezer is more challenging due to the light shift caused by the tweezer. The higher trap depth necessary to trap the hotter Na atom after freespace cooling and the absence of an accessible magic wavelength cause a large (> 200 MHz) light shift on the cooling transition when the Na atom is in the tweezer. This shift significantly changes the cooling detuning making it ineffective in the tweezer. We fix this issue by alternating the cooling and the tweezer light at 2.5 MHz. The frequency is low enough to allow a few photons to be scattered when the cooling light is on to perform cooling on the atom, yet high enough compared to the highest trapping frequency in the tweezer to prevent parametric heating of the trapped atom [91].

We use fluorescence imaging to detect the atoms in the tweezer which requires cooling to prevent the photon recoil from heating the atom out of the tweezer before enough photons can be collected. This is done using the free-space cooling beam path previously used for the MOT and the PGC with a different power and detuning setting. The light scattered from the atom in the tweezer is collected by the objective which is then focused onto a EM-CCD camera for detection. We achieve an overall photon collection efficiency of 8 % and 5 % for Na and Cs respectively. The difference between the efficiency for the two atoms is mainly caused by the quantum efficiency of the camera.

In our experiment, the tweezer is generated by focusing trap light through an objective with a numerical aperture (NA) of 0.55. The wavelengths used for the tweezers are 700 nm (Na) and 1038 nm (Cs), which give diffraction limited beam waists of 0.6 μm and 0.9 μm respectively. The selection of the wavelength ensures that each atom can only trapped by its respective tweezer since,

1. The Na trap wavelength of 700 nm generates a repulsive potential for the Cs atom and therefore cannot trap Cs.

2. The Cs trap can attract Na. However, the Cs trap is not being toggled out of phase with the Na cooling light and therefore cannot trap Na due to the light shift.

Due to technical limitations, we cannot measure the tweezer power directly. Instead we measure the power upstream in the tweezer beam path where the beam is accessible and correct for the known total transmission efficiency of 23(2) % from all of the optics. The
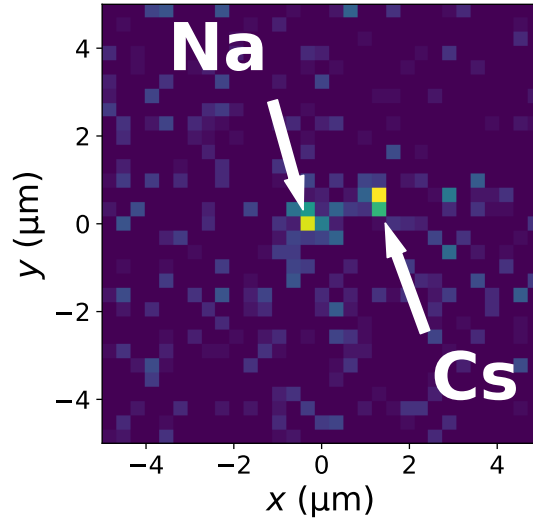
Figure 2.4: Image of a single Na and Cs atoms in their respective tweezers showing a simultaneous loading event.

tweezer powers quoted in this thesis are measured at the upstream location and must be multiplied by the factor 0.23 to obtain the best estimate of the total power at the focus of the tweezer.

The single atom can be observed on the EMCCD camera if the tweezer beam is turned on during MOT loading and the loading efficiency is improved by the additional free-space cooling steps including CMOT and PGC. Fig. 2.4 shows an image of both the Na and Cs atoms. In most experiments, however, the two species are imaged separately in order to reduce the background and to improve the detection fidelity. We take an image for each atom right after the loading step in order to determine which atoms (if any) are loaded and this is repeated at the end of each experimental sequence to determine if the atoms have survived.

By repeating the experiment and sorting the events according to the loading result, we can accurately identify the case when a single atom (Na or Cs) or a pair of atoms is loaded and estimate the corresponding single- and two-body survival probabilities. Most of the measurements in this thesis are based on these probabilities.

2.4   Summary and Outlook

In this chapter we discussed the trapping and imaging of the single atoms in the optical tweezers and the steps leading up to it. We take advantage of many techniques developed and used in previous optical tweezer experiments to boost our control on the atoms in preparation for the control on the molecules.

The atoms trapped in the tweezers and the high fidelity detection of them form the foundation of our experiment. The many capabilities of our system will be discussed in more detail in the coming chapters

3

Raman Sideband Cooling

3.1 INTRODUCTION

The trapping of the single atoms in the optical tweezers in section 2.3 improves our control over the motional degrees of freedom of the atoms by confining it to the focus of the tweezer. However, the temperature of the atoms directly after loading is still relatively high (80 mK for Na and 10 mK for Cs) compared to the trapping frequencies ($80, 600$ kHz

or 4, 30 mK for Na and 20, 160 kHz or 1, 8 mK for Cs) of the tweezer causing a large number of motional states to be occupied ($\approx$ 60 for Na and $\approx$ 20 for Cs). Further cooling of both atoms to the motional ground state of the tweezer is required in our experiment for two reasons:

1. Our assembly approach relies on the preparation of atomic quantum states to realize full control of the molecule. More concretely, the temperature and motional states of the molecule we create is directly controlled by the cooling of the atoms in the tweezer.

2. Cooling to the motional ground state reduces the size of the atomic wavefunction. This increases the interaction between the atoms and improves the coupling to the molecular states as will be shown in later chapters.

The tight confinement and relatively high trapping frequencies provided by the optical tweezer enable the potential use of Raman sideband cooling (RSC) in our experiment to reach the motional ground state. Originally developed for ion systems to take advantage of the tight confinement from ion traps [94, 95], resolved sideband cooling has later been implemented for neutral atomic systems using Raman transitions in both optical lattices and optical tweezers on multiple species [96–98]. However, the application of RSC requires favorable initial cooling conditions and very tight confinement from the trap and remains challenging and underexplored outside this regime (formally known as the Lamb-Dicke regime, which will be defined later in section 3.2.1).

For Cs atoms in our system, the efficient polarization gradient cooling allows RSC to be implemented in a similar fashion [99] as in previous experiments, where we have been able

49

to achieve a ground-state probability of 96(3) %. Unfortunately, the parameters achievable for Na lands outside the Lamb-Dicke regime making the implementation of RSC much more challenging. In this chapter, we will discuss how we overcame these challenges and achieved ground-state cooling using RSC in our experiment. We will start in section 3.2 and 3.3 with a description of the theory for RSC and the related thermometry technique. Section 3.4 describes the experimental setup for RSC. The challenges related to cooling outside the Lamb-Dicke regime are analyzed in detail in section 3.5 followed by section 3.6 and 3.7 listing the solution we developed to overcome these challenges. The experimental realization and result of the cooling sequence are discussed in section 3.8, 3.9 and 3.10 before the summary in section 3.11. The discussion here is based on our publication in [100].

3.2   Basic Theory

The relevant energy diagram and the laser frequencies for RSC are shown in Fig. 3.1. We approximate the trapping potential using a harmonic oscillator. Since this is a separable potential, we can work in terms of the 1D motional state $|n\rangle$ and the result can be easily generalized to the full 3D system.

The cooling sequence consists of two types of pulses. First, a Raman pulse drives the atom to a different hyperfine state while simultaneously reducing the motional energy of the atom. The optical pumping (OP) pulse afterwards then resets the hyperfine state of
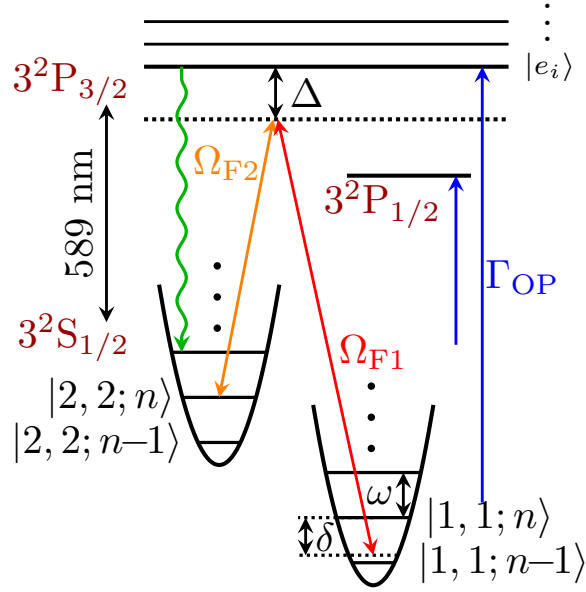
Figure 3.1: Single Na atom Raman sideband cooling scheme. The Raman transitions couples $|2, 2; n\rangle$ and $|1, 1; n + \Delta n\rangle$ through the intermediate states $|e_i\rangle$ in the $3^2P_{3/2}$ electronic state. The transitions have a one-photon detuning $\Delta_i \approx 75$ GHz. Two-photon detuning, δ, is defined relative to the $\Delta n = 0$ carrier transition. For optical pumping, we use two σ^+ polarized transitions, one to pump the atom state out of $|1, 1\rangle$ via $3^2P_{3/2}$ and one to pump atoms out of $|2, 1\rangle$ via $3^2P_{1/2}$ to minimize heating of the $|2, 2\rangle$ state.

the atom and reduces the entropy of the system. This sequence is then repeated until the system reaches the ground motional state where there is no more motional energy to be taken out of the system via the Raman pulse. In this section, we will discuss the theory of each type of pulses individually. We will cover how the pulses affect cooling performance in section 3.5.

3.2.1   RAMAN TRANSITION

As shown in Fig. 3.1, the cooling sequence starts with the sodium atom in the $|s_1\rangle \equiv |2, 2\rangle$ hyperfine state, and a Raman transition is used to drive the atom to the $|s_2\rangle \equiv |1, 1\rangle$ state, where $|F, m_F\rangle$ denotes the F and m_F quantum number for the sodium atom. The full Rabi frequency for such a transition is given by [101]

$$\Omega_R^0 = \sum_i \frac{\Omega_{1i}\Omega_{2i}^*}{2\Delta_i} \tag{3.1}$$

where $\Omega_{ai} \equiv \langle a|\mathbf{d} \cdot \mathbf{E}_a|e_i\rangle$ is the single photon Rabi frequency between $|a\rangle$ and $|e_i\rangle$ and Δ_i is the single photon detuning from excited state $|e_i\rangle$. The sum is over all the excited states $|e_i\rangle$ allowed by the selection rules, which may be different based on the polarization of the Raman beams.

In order to account for the motional degrees of freedom, we need to take the spatial wavefunction of the atom and light into account. As mentioned above, we approximate

the atomic motional wavefunction by the harmonic oscillator eigenstates $|n\rangle$. Coupling

between different n states from the Raman transition is allowed due to the recoil from the

Raman lasers, which corresponds to a spatial phase imprinting of $e^{i\Delta \mathbf{k}\cdot\hat{\mathbf{x}}}$ where $\Delta\mathbf{k}$ is the

wavevector difference between the two Raman beams. Using the creation $(\hat{a}^\dagger)$ and annihila-

tion $(\hat{a})$ operators and the relation $\hat{\mathbf{x}} = \mathbf{x}_0(\hat{a} + \hat{a}^\dagger)$ where $x_0 = \sqrt{\hbar/2m\omega}$ is the harmonic

oscillator length, the phase factor can be expressed as $e^{i\eta^R(\hat{a}+\hat{a}^\dagger)}$ where $\eta^R \equiv \Delta\mathbf{k}\cdot\mathbf{x}_0$ is the

Lamb-Dicke parameter for the Raman transition. The matrix element between motional

state $|n\rangle$ and $|n'\rangle$ is therefore,

$$M_{n,n'} = \langle n|e^{i\eta^R(\hat{a}+\hat{a}^\dagger)}|n'\rangle$$

and the final Raman Rabi frequency between motional states n and n' is given by,

$$\Omega_R^{n,n'} = M_{n,n'}\Omega_R^0$$

For $n = n'$, this is called a carrier transition and the others are called sideband transitions.

If the final state is higher than the initial one, i.e. $n' > n$, it is a heating sideband, while

transitions with $n' < n$ are cooling sidebands.

A closed form result for $M_{n,n'}$ is given in Ref. [102],

$$M_{n,n'} = e^{\left(\eta^R\right)^2/2} \sqrt{\frac{n_<!}{n_>!}} \left(\eta^R\right)^{|n-n'|} \cdot L_{n_<}^{|n-n'|}\left(\left(\eta^R\right)^2\right)$$

where $n_<$ and $n_>$ are the lesser and greater, respectively, of n and n', and L_n^α is the generalized Laguerre polynomial,

$$L_n^\alpha(x) \equiv \sum_{m=0}^{n} (-1)^m \begin{pmatrix} n+\alpha \\ n-m \end{pmatrix} \frac{x^m}{m!}$$

An important limit is the so-called Lamb-Dicke (LD) regime defined as $\left(\eta^R\right)^2(2n+1) \ll 1$. In this case, we can approximate the phase factor in leading order of η^R,

$$e^{i\eta^R\left(\hat{a}+\hat{a}^\dagger\right)} \approx 1 + i\eta^R\left(\hat{a} + \hat{a}^\dagger\right)$$

and the matrix element

$$M_{n,n'} \approx \partial_{n,n'} + i\eta^R\sqrt{n+1}\partial_{n+1,n'} + i\eta^R\sqrt{n}\partial_{n,n'+1}$$

The three terms corresponds to the carrier ($n' = n$), the first order heating sideband ($n' = n+1$) and the first order cooling sideband ($n' = n-1$) with corresponding strength

1, $\eta^{\mathrm{R}}\sqrt{n+1}$ and $\eta^{\mathrm{R}}\sqrt{n}$ respectively. We can clearly see from this approximation that the coupling to other motional states is stronger for a larger η^{R} and higher motional quantum number n. We will discuss this effect outside the LD regime and its implication on the cooling performance in more detail in section 3.5.

3.2.1.1 Scattering from Raman Beams

In addition to driving the Raman transition, the Raman beams can also cause scattering. The rate of the scattering is[‡],

$$\Gamma = \sum_i \frac{\Gamma_{ei}\Omega_{1i}^2}{4\Delta_i^2}$$

where Γ_{ei} is the linewidth of the excited state $|e_i\rangle$. Together with Eq. 3.1, we see that approximately $\Gamma/\Omega_{\mathrm{R}} \propto 1/\Delta$ so a larger detuning should be used in order to reduce the scattering during RSC.

3.2.2 Optical Pumping

Driving the system on a cooling sideband with a Raman transition can reduce the motional energy of the atom. However, this is a fully coherent process that does not reduce the system entropy and therefore is not actually "cooling" the system and does not help us

---

[‡]Here we assume that each Raman beam only couples to their respective ground states. Including coupling to the other ground state increases the scattering rate but does not change the scaling with detuning.

achieve better control over the quantum state of the system. Instead, quantum state control is achieved in RSC via the OP pulse.

The state of the atom after a Raman π-pulse is $|1, 1\rangle$. We first use σ^+ polarized light that is resonant with the $|1, 1\rangle$ to $|2', 2\rangle$ transition on the D2 line to pump the atom out of the $F = 1$ manifold to a mixture of $|2, 1\rangle$ and $|2, 2\rangle$ state. The beam is generated from the same source as the repumper for the MOT, which simplifies our setup.

Since the target spin state for the OP, $|2, 2\rangle$, is a stretched state, we can pump the atom from other $F = 2$ states into this state by simultaneously applying σ^+ light that is resonant with the $F = 2$ states. However, if this is done using a $F = 2$ to $F' = 3$ transition, the OP beam will allow continuous photon cycle between the states $|2, 2\rangle$ and the $|3', 3\rangle$ causing unnecessary motional heating during OP. Therefore, the OP should be done on a $F = 2$ to $F' = 2$ transition to minimize this heating. Unfortunately, for Na, the corresponding transition from $3^2S_{1/2}$ to $3^2P_{3/2}$ that is used for the MOT is not useable due to the small energy difference of 60MHz (or 6 line widths) between the $F' = 2$ and $F' = 3$ states [89]. Instead, we must use the sodium D1 line, i.e. $3^2S_{1/2}$ to $3^2P_{1/2}$ transition, which lacks a $F' = 3$ excited state [96, 103]. We find a reduction in the scattering rate by a factor of $130(20)$, as compared to using OP light resonant with $3^2P_{3/2}$ to address $F = 2$ atoms.

3.3 Raman Sideband Thermometry

From the discussion in section 3.2.1, we see that the strength of the sideband transition depends on the initial motional state as well as the Lamb-Dicke parameter η^{R} of the atom. This dependence allows us to infer the motional state of the atom by measuring the sideband height, i.e. the so-called sideband thermometry [96, 104].

In particular, for an atom with temperature T, the probability for the atom to be in the motional state $|n\rangle$ is,

$$p_n = \left(1 - e^{-\hbar\omega/k_B T}\right) e^{-n\hbar\omega/k_B T}$$

For a Raman pulse with full Rabi frequency Ω_{R}^0 and time t, the peak height for the first order heating (+) and cooling (-) sidebands are,

$$b_{\pm} = \sum_{n=0}^{\infty} p_n \sin^2\left(\frac{\Omega_{\mathrm{R}}^0 t}{2} M_{n,n\pm 1}\right)$$

Note that since $p_{n+1} = p_n e^{-\hbar\omega/k_B T}$, $M_{n,n'} = M_{n',n}$ and $M_{n,-1} = 0$, we have

$$
\begin{aligned}
b_{-} &= \sum_{n=0}^{\infty} p_n \sin^2\left(\frac{\Omega_{\mathrm{R}}^0 t}{2} M_{n,n-1}\right) \\
&= e^{-\hbar\omega/k_B T} \sum_{n=1}^{\infty} p_{n-1} \sin^2\left(\frac{\Omega_{\mathrm{R}}^0 t}{2} M_{n-1,n}\right) \\
&= e^{-\hbar\omega/k_B T} b_{+}
\end{aligned}
$$

Therefore, if we measure the ratio of the cooling and heating sideband heights $\alpha \equiv h_-/h_+$, we can calculate the temperature of the atom with $\mathrm{e}^{-\hbar\omega/k_B T} = \alpha$. The corresponding ground-state probability is,

$$
\begin{aligned}
p_0 &= 1 - \mathrm{e}^{-\hbar\omega/k_B T} \\
&= 1 - \alpha
\end{aligned}
\tag{3.2}
$$

and the average motional state

$$
\begin{aligned}
\bar{n} &= \sum_n n\alpha^n \\
&= \frac{\alpha}{1 - \alpha}
\end{aligned}
\tag{3.3}
$$

We will use these to experimentally characterize the performance of the cooling sequence in the following sections.

3.4 SETUP

The geometry of all the beams and magnetic field involved is shown in Fig. 3.2. In order to make the cooling more efficient and simplify the sideband thermometry, we address the motion along the three principal axes of the tweezer using different pairs of Raman beams. In order to maximize the beam intensity so that a larger single photon detuning can be used
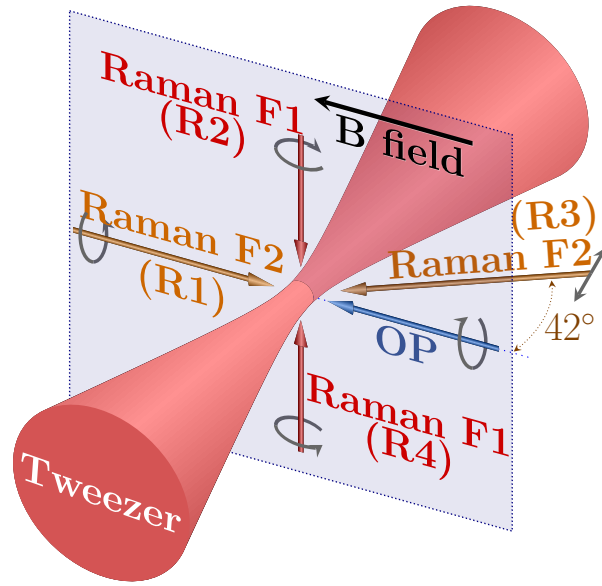
Figure 3.2: Geometry and polarizations of the Raman and optical pumping beams relative to the optical tweezer and bias magnetic field. Raman beams R1 and R4 address the radial x-mode. R1 and R2 address the radial y-mode. R3 and R4 address the axial z-mode, where the beams also couple to radial motion, but this coupling can be neglected when the atoms are cooled to the ground state of motion.

while maintaining the same Raman Rabi frequency, we focus the Raman beam onto the single atom with a waist of ≈ 100 μm. The maximum powers within each Raman beam are between 1 and 6 mW which give us a maximum Raman Rabi frequency of 50 to 200 kHz.

We apply an external bias magnetic field of 8.8 G parallel to the polarization of the tweezer beam (and orthogonal to the tweezer beam propagation direction). This makes the field orthogonal to the effective magnetic field of the tweezer, which minimizes the vector light shifts [105, 106]. Since the optical pumping beam requires σ^+ polarization, it is set up to propagate parallel to the applied magnetic field.

Since both the Raman transition and the optical pumping change the hyperfine state of the atom, the states of the atoms can be used to detect and calibrate these processes. This is done in our experiment using state sensitive "push-out" as follows,

1. Push-out light resonant with the $|F = 2, m_F = 2\rangle$ to $|F' = 3, m_{F'} = 3\rangle$ cycling transition is sent in through the OP beam path. Due to the small differential Zeeman shift, this is also close to resonance for all other Zeeman states with $F = 2$ and will pump them to $|F = 2, m_F = 2\rangle$. Since the cycling transition is protected by F and m_F selection rule as well as the stronger coupling compared to all other transitions, the atom can scatter >10000 photons before decaying to the $F = 1$ state.

2. The push-out light is turned off and the depth of the trap is lowered so that atoms that are heated by the OP light will leave the trap.

3. The trap depth is ramped back up and an image of the leftover atom is taken to measure the probability of atom in the $F = 1$ states.

RSC is typically performed in the LD regime where the coupling to other motional states is small. Due to the light mass, short wavelength, limited trap depth and high initial temperature of the sodium atom however, we have to start our RSC sequence outside the LD regime. This creates unique challenges to our experiment. A detailed understanding of the cooling performance is required to understand and overcome these challenges.

The simplest way to estimate the effectiveness of RSC is by keeping track of the average energy of the atom during the cooling sequence. For a typical RSC sequence in the LD regime, all the cooling is done on the strongest first order cooling sideband. The energy removed from the atom after one driven Raman pulse is therefore, $\Delta E_- = \omega$. In order to reinitialize the hyperfine state, the sodium atom needs to scatter on average 2 photons from the OP pulse which increases the average energy of the driven atom by $\Delta E_+ = 4\omega_{\mathrm{recoil}}$[‡] where $\omega_{\mathrm{recoil}} \equiv \hbar k^2/2m$ is the recoil energy [89] and k is the OP light wave vector. The heating to cooling ratio in one RSC pulse cycle is therefore,

$$\frac{\Delta E_+}{\Delta E_-} = \frac{2\hbar k^2}{m\omega} = 4k^2 x_0^2$$

$$= 4\left(\eta^{\mathrm{OP}}\right)^2$$

[‡]The factor of 4 comes from 2 absorbed photons and 2 re-emitted photons.
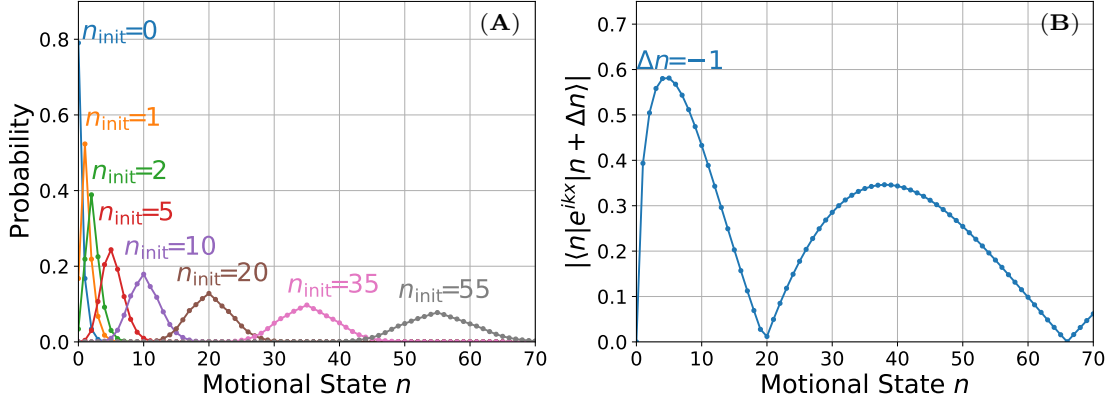
Figure 3.3: Optical pumping motional-state redistribution and Raman coupling for large LD parameters for the axial direction (z) [107]. The range plotted covers 95 % of the initial thermal distribution. (A) Motional-state distribution after one OP cycle for different initial states motion, n_{init}. Due to photon-recoil and the large LD parameter, $\eta_z^{\text{OP}} = 0.55$, there is a high probability of n changing. (B) Matrix elements for Raman transition on the first order cooling sideband deviate from $\sqrt{n}$ scaling with multiple minima.

where $\eta^{\text{OP}} \equiv kx_0$ is the Lamb-Dicke parameter for OP. Therefore, in order to achieve net cooling, we need $\left(\eta^{\text{OP}}\right)^2 < 0.25$. In 3D with cooling along multiple axes with different trapping frequencies, and therefore different η^{OP}, the $\left(\eta^{\text{OP}}\right)^2$ in the requirement is replaced by a weighted average of different axes depending on the frequency each axis is cooled in the sequence.

In our experiment, the OP Lamb-Dicke parameters are $\eta_x^{\text{OP}}, \eta_y^{\text{OP}}, \eta_z^{\text{OP}} = 0.25, 0.25, 0.55$. Based on the metric above, all cooling sequence should have a net cooling effect. This, however, does not guarantee cooling into the ground motional state, nor does it fully characterize the efficiency of the cooling sequence since the averaging hides a few critical aspects of having a large Lamb-Dicke parameter.

One of the important effects can be seen in Fig. 3.3A showing the motional-state dis-

tribution after one OP cycle for different initial motional states n_{init} [107]. Although the average heating is fixed at $4\omega_{\text{recoil}}$, independent of n_{init}, the spread or the uncertainty of n after the OP is significantly higher for high n_{init}. This effect significantly increases the difficulty in controlling the state during the RSC sequence. It can negatively impact the cooling performance and may lead to increased loss during cooling due to atoms escaping to higher motional states.

The other important effect is the dependence of matrix element $M_{n,n+1}$ on the motional level n. While this dependence is not a new effect, since the $\sqrt{n}$ dependence on the cooling sideband strength exists even in the LD regime and must be taken into account with pulse time variation [99, 102] to achieve efficient cooling, the high Lamb-Dicke parameter adds even more complications. As shown in Fig. 3.3B, rather than a simple $\sqrt{n}$ dependence, it is a non-monotonic function and more importantly has multiple minima, so-called "dead-zone", within the range of motional states we are interested in [107]. The coupling strength for states in the dead-zones can be reduced by more than ten times which can significantly affect the efficiency of the cooling pulse and even makes it virtually impossible to drive Raman transitions on atoms in these states in order to cool them further. A cooling sequence can therefore accumulate population in the dead-zones rather than the ground state. Their small coupling strengths also reduce their signal level during Raman sideband spectroscopy making these states nearly invisible to sideband thermometry which further complicates the
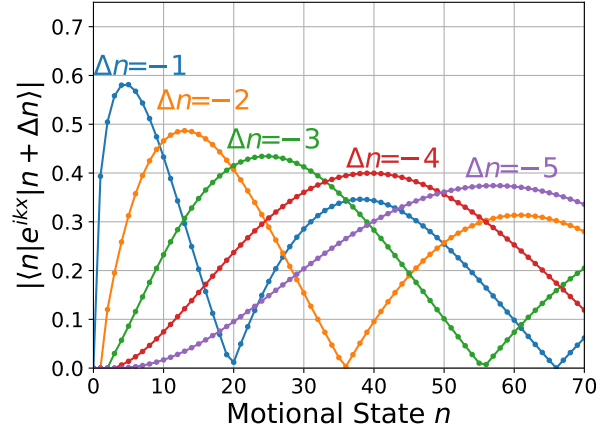
Figure 3.4: Matrix elements for Raman transition including high order sidebands. During cooling, we utilize the fact that high motional states couple most effectively to sidebands with large $|\Delta n|$ in order to overcome the issue with variation and dead zone in the coupling strengths.

optimization of the cooling sequence.

3.6   Solution: High Order Sidebands

The main solution to the issues related to the large Lamb-Dicke parameter is in fact the

large Lamb-Dicke parameter itself. The increased coupling to other motional states for

large Lamb-Dicke parameter and high motional states applies not only to $|\Delta n| = 1$ but to

higher Δn as well. Fig. 3.4 shows the coupling to higher order cooling sidebands which all

have comparable strengths as the first order sidebands in different ranges of motional states.

Because of this, it is now possible, and in some cases preferred, to apply Raman cooling

pulse on the higher order sidebands instead of only the first order one. These pulses reduce

more energy from the system per pulse which directly improves the cooling to heating ratio
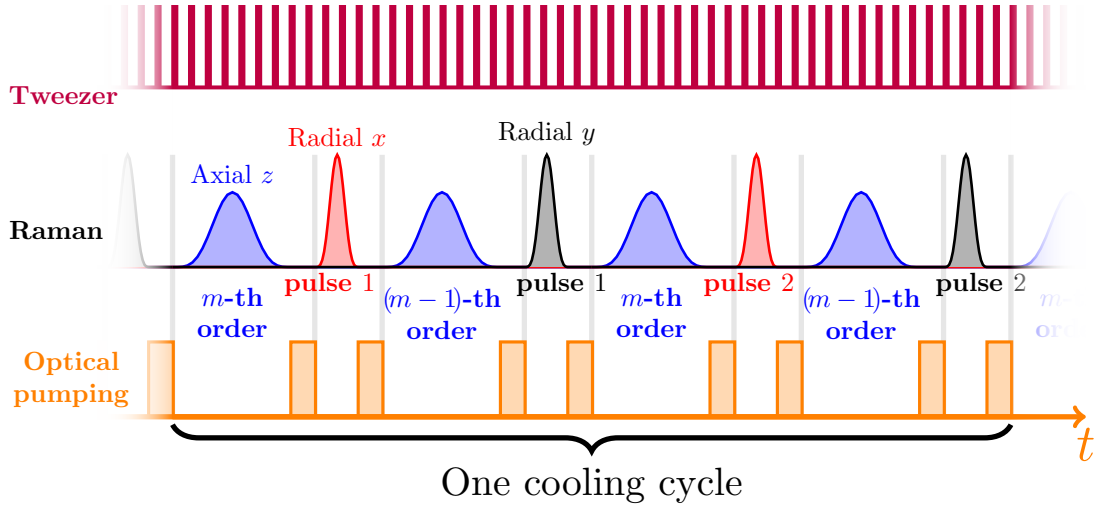
Figure 3.5: Schematic of the cooling pulse sequence. The tweezer is strobed at 3 MHz to reduce light shifts during optical pumping [91]. Each cooling cycle consists of 8 sideband pulses. The four axial pulses address two sideband orders. The two pulses in each radial direction either address $\Delta n = -2$ and $\Delta n = -1$ or have different durations to drive $\Delta n = -1$, at the end of the cooling sequence when most of the population is below $n = 3$. The Raman cooling and spectroscopy pulses have Blackman envelopes [108] to reduce off-resonant coupling, while the measurement Rabi pulses in Fig. 3.7 have square envelopes to simplify analysis.

and allows better control on the motional state given the uncertainty after an OP pulse.

More importantly, depending on the motional level, there is always a sideband order with

significant coupling strength that can be used to cool it, therefore completely removing

the coupling dead-zones. Moreover, by using each sideband order only near their coupling

maxima, the coupling strength variation is also greatly reduced which removes the need to

vary the pulse times for all but the pulses on the first order sideband.

The change in cooling technique by including higher order sidebands, however, does not remove the effect of coupling variation on the sideband thermometry. If a non-thermal distribution of motional states is produced by the cooling sequence, the ratio of the first order sideband height still cannot be trusted to calculate the temperature or the ground-state probability. Including higher order sidebands in the sideband thermometry could in principle give us enough information about the state distribution but doing so for a non-thermal distribution is not easy or reliable. We therefore use a Monte-Carlo simulation[‡] to guide our search for the optimal sequence [109, 110]. The simulation includes accurate scattering rates and branching ratios from the tweezer, Raman and OP beams. For best simulation performance, the atom is assumed to be in a single motional state, i.e. with a certain n_x, n_y and n_z, after each Raman or OP step[§]. It is also assumed that each Raman pulse drives only the intended sideband order, which is a property that needs to be ensured in the experiment (section 3.9.1). For each cooling sequence simulated, the Raman beam powers and frequencies, and the OP beam power and polarization purity are varied slightly around the respective expected values in order to confirm the robustness of the sequence against

---

[‡]See https://github.com/nacs-lab/yyc-data/blob/9edda7f7cfa111e17deb82e1518ef3aeca048875/calculations/sideband/sideband.jl and https://github.com/nacs-lab/yyc-data/tree/9edda7f7cfa111e17deb82e1518ef3aeca048875/lib/NaCsSim/src for the code.

[§]This assumes no coherence between different motional states, which is the case as long as the Raman pulses are separated from each other by OP pulses.

fluctuations in the experiment. Fig. 3.5 demonstrates the resulting optimal sequence from the simulation. In particular, we find that alternating the cooling pulses between two neighboring orders for the axial direction and $\Delta n = -2$ and $\Delta n = -1$ for the radial directions eliminates the accumulation of population in motional states with small Raman coupling. The simulation also confirms that setting the coupling strength of each sideband to drive a Rabi π-pulse corresponding to the maximum matrix element motional state (i.e. the maxima in Fig. 3.4) yields efficient cooling, initially, as we expected from section 3.6. The efficiency of cooling on higher-order sidebands diminishes as the atom approaches the ground state, so the final cycles utilize only the $\Delta n = -1$ sideband while alternating between the three axes.

3.8   Alignment of Raman and OP Beams

Due to the small waists of the Raman beams, it is important to align the Raman beam to the single atom with high precision in order to maximize the Raman Rabi frequency as well as to minimize the intensity fluctuation of the Raman beam experienced by the atom due to pointing instability. Such precision cannot easily be achieved using an external reference and must be done by using the single atom itself as the alignment target.

In our experiment, we have developed two different methods to align or verify the alignment of the Raman beams, both relying on the scattering from the Raman beams. For ini-

Table 3.1: Single photon Rabi frequency and scattering rate for the Na Raman beams. Since in general each beam couples to more than one excited state, the single photon Rabi frequency is listed for the reduced matrix element $\langle J = 1/2 || er || J' = 3/2 \rangle$ [89]. The scattering is calculated for the $|F = 2, m_F = 2\rangle$ ground state since this is the dark state in the cooling scheme where the scattering matters the most. The polarization of the beams can be seen in Fig. 3.2. R5 is the F1 beam that is co-propagating with R3 with orthogonal polarization that is used to drive sideband-free Raman transitions (not used for cooling). We also assume 10 % power of the R1 beam is in the opposite circular polarization (σ^+) instead of being purely σ^-.

Beam	R1 (F2)	R2 (F1)	R3 (F2)	R4 (F1)	R5 (F1)
Rabi Frequency ($2\pi \times$ MHz)	41.2(23)	16.4(26)	45.5(31)	34.8(21)	41.4(26)
Scattering Rate ($2\pi \times$ Hz)	5.41(62)	1.50(48)	11.0(15)	6.74(82)	9.5(12)

tial alignment, or when the beam position is off-center by more than a beam waist, we couple resonant Sodium D2 light into the Raman beam path in order to enhance the scattering rate. The coarse alignment is done based on maximizing the displacement and depleting of the MOT due to radiation pressure. After that, the fine alignment of the Raman beams is done by reducing the power in the Raman beam path and maximizing the heating effect on the single atom. When the Raman beam is focused on the tweezer position, we can observe a depletion of the single atom live loading signal while the MOT is not affected as significantly. This process is then repeated with increasingly lower power in the Raman beam path until the desired position sensitivity is reached.

In order to verify the alignment of the tweezer without any physical change to the beam path, we use a second method to calibrate the single photon Rabi frequency of the Raman light. This method requires a working OP to initialize the spin state of the atom so it is less convenient for aligning from scratch. To use this method, the atom is first loaded in the

tweezer and initialized in the $|2, 2\rangle$ state. We then turn on a single Raman beam at maximum power for a variable length of time. The off resonance scattering from the Raman beam will cause the spin state of the atom to change and the population in $F = 1$ state is measured by removing the $F = 2$ population using a pushout pulse. The rate of the spin change is fitted to a theory model to derive the Rabi frequency of the Raman light. The results of the fits are shown in table 3.1. The table also includes the total scattering rates from each of the Raman beams which correspond to a cumulative of 3 scattering events on average during the whole cooling sequence and should not be a limiting factor for the cooling performance.

The OP beam has a much larger waist (≈ 1 mm) and therefore requires less alignment in the beam position. However, since the OP beam needs to be resonant with the excited state, the strong light shift from the tweezer can significantly affect the OP efficiency. Fortunately, the method described in section 2.3 that fixes this problem for the loading of the atom in the tweezer can also be used here. In this case, however, only the tweezer light is being switched on and off at 2.5 MHz and not the OP light for simplicity. Due to the low intensity and Rabi frequency of the OP light, the OP will be completely stopped during the on-cycle of the tweezer causing the OP to happen only during the off-cycle when there is zero light shift.

In order to take advantage of the dark-state optical pumping and minimize unnecessary

scattering for atoms in the $|2, 2\rangle$ state, the OP beam needs to have a pure σ^+ polarization. This requires the OP beam to propagate parallel to the magnetic field in addition to having the correct circular polarization. The alignment is done by minimizing "depumping" of the atom spin state caused by the OP beam, similar to the technique we used to calibrate the Raman beam Rabi frequency. After the atom is initialized in the $|2, 2\rangle$ state, we turn on the D1 OP light for a certain time which should not address the atom when perfectly aligned. The misalignment of the beam, however, will cause the atom to scatter from the OP beam and change to $F = 1$ state, i.e. "depumped", with a certain probability. We then change the alignment of the beam and minimize the depumping rate. Due to a similar requirement for Cesium OP, the propagation direction of the OP beam for Sodium and Cesium are aligned to each other by overlapping them using mechanical target to better than $0.08°$ first before the magnetic field direction is aligned to the OP beams by minimizing depumping. For polarization alignment, we first clean up the linear polarization of the light using the LPVISC050-MP2 nanoparticle linear film polarizer from Thorlabs with better than $100,000 : 1$ extinction ratio. After that we use both a half waveplate and a quarter waveplate to generate a circularly polarized light. We observed that both the polarization cleanup and the half waveplate is necessary to obtain the best polarization alignment in order to compensate for the polarization fluctuation caused by the fiber as well as the birefringence of the optics and windows within the OP beam path. After alignment, the OP

intensity is calibrated by measuring the OP rate for an atom prepared in $|2, 1\rangle$ state using Raman transitions[‡]. From this measurement we determined that the power impurity of the OP polarization to be ≈ 100 ppm.

Other than the alignment procedure above, we have also observed that reflection of the OP beam can contribute significantly to the polarization impurity and must be avoided. In particular, since the Raman beam R1 counter propagates with the OP beam, it is possible for the OP beam to be coupled into the Raman fiber and then retro-reflected to be focused onto the atom through the Raman beam path at a wrong polarization. Since the Raman beam size is much smaller, we have observed as much as 3 % polarization impurity caused by this mechanism despite only a small amount of power being reflected. This issue, along with other reflections, are reduced by avoiding optics with normal incident on the exit path of the OP beam as well as changing the propagation direction of the R1 Raman beam to have a small angle with the OP beam which reduces the OP power coupled into the Raman beam fiber.

3.9   Implementing Optimized RSC Sequence

In order to achieve the optimal cooling performance, a few more considerations are important for implementing the sequence from section 3.7.

[‡]One from $|2, 2\rangle$ to $|1, 1\rangle$ and a second one from $|1, 1\rangle$ to $|2, 1\rangle$.

3.9.1 Pulse shaping

In order to achieve optimal performance from the cooling sequence, it is important to accurately drive the intended sideband order. In fact, in the absence of undesired scattering, the frequency resolution of the Raman transition limits the final achievable temperature. This is particularly important when driving the first order cooling sidebands since any coupling to the carrier may change the spin state of the atom without removing any motional energy therefore causing a net heating effect after the OP pulse.

The obvious way to achieve this is to narrow the linewidth of the Raman transition, e.g. by using a lower power or Raman Rabi frequency. However, reducing the linewidth of the transition also increases the susceptibility to resonance fluctuations. Therefore the desired solution is to reduce the off-resonance coupling of the Raman beam for large detuning while increasing or maintaining the coupling for small detuning. We achieve this by using a Blackman pulse shape for the Raman transition [108][‡].

3.9.2 Calibration

The Raman sideband frequencies are calibrated by measuring the Raman spectrum before cooling (an example of which is shown in the initial spectrum in Fig. 3.6). However, since

---

[‡]While more complex pulses can be constructed to achieve an even sharper detuning cutoff [111], such pulses generally significantly increase the pulse time and can cause more heating during cooling due to scattering and other heating mechanisms. The Blackman pulse we use offers a balance between the pulse time and off-resonance coupling reduction.

higher sideband orders are mainly used to cool atoms in higher motional states, the resonance frequencies for these sidebands are not equally-spacing anymore due to the anharmonicity of the trapping potential. In order to estimate the effect on the sideband frequencies, we can define anharmonicity as $A_{i,n} = (E_{i,n+1} - E_{i,n})/h - \omega_i/(2\pi)$ for each trap axis i where ω_i is the trapping frequency for the ground motional state, and calculated from the quartic term of the optical tweezers via perturbation theory. In the paraxial approximation, we find $A_{i,n} = -3n\hbar/4\pi m d_i^2$, where d_i equals the beam radius for the radial directions and $d_z \approx \pi w_{0,x} w_{0,y}/\lambda_{\text{trap}}$. Numerically, $\{A_{x,n}, A_{y,n}, A_{z,n}\} = \{-1.4, -1.4, -0.16\}n$ kHz. For the states addressed by higher order sidebands, this broadens and shifts the resonant frequencies due to the n-dependence of the transitions.

To mitigate this, we calibrate the frequency of each sideband order individually at the initial temperature. However, since the first order sideband is mainly used to cool atoms that are close to the ground state, their resonance frequency is recalibrated using partially cooled atoms after the initial calibration. The use of high Rabi frequencies and the Blackman pulse shape also reduces the effect of anharmonicity by broadening the spectrum as much as possible.

Although we can calibrate the single photon Rabi frequency of the Raman beams from the scattering rate (section 3.8), we also calibrate the Raman Rabi frequency on the carrier and different sideband orders. This offers a more direct and sensitive measurement of the

73

cooling sequence parameters. Unlike resonance frequency, the anharmonicity only has a second order effect on the Rabi frequency and is therefore ignored. The calibration measures only the carrier and first order heating sideband which has the highest signal after cooling (an example of which is shown in the cooled Rabi flopping signal in Fig. 3.7). The Raman Rabi frequencies measured on these two transitions are used to calculate the full Rabi frequency Ω_R^0 and the Lamb-Dicke parameter, which are in-turn used to calculate the Rabi frequency on other sideband orders.

Since the final calibration of both the Raman Rabi frequency and resonance requires a working cooling sequence, when optimizing the sequence from scratch, the calibration process is applied iteratively as the cooling performance is improved.

3.10 Cooling Performance

Our final cooling results are shown in Fig. 3.6 and 3.7. In total, 540 cooling pulses (total duration 53 ms) are applied along three axes with cooling beginning on the radial second order and axial fifth order sidebands. The full sequence including calibrated parameters can be found in appendix B.

For the more tightly confined radial directions, we observe clear $\Delta n = 1$, $\Delta n = -1$, and $\Delta n = -2$ sidebands before RSC, as shown in Fig. 3.6A and B. After RSC, the $\Delta n = -1$ and $\Delta n = -2$ sidebands on both radial axes are strongly reduced. Using Eq. 3.2 and 3.3,

74
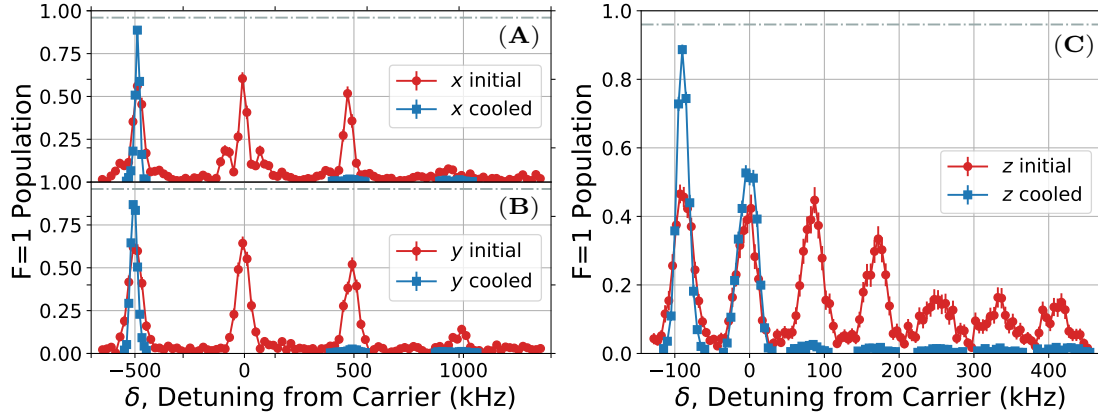
Figure 3.6: Raman sideband spectra for (A) x, (B) y, (C) z axis before (red circle) and after (blue square) applying Raman sideband cooling sequence. The height of the cooling sidebands (positive detuning) are strongly suppressed after cooling which suggests most of the atoms are cooled to the motional ground state in the trap. The horizontal dashed lines in all the plots correspond to the 4 % probability of imaging loss.

we obtain $\bar{n}_x = 0.019(4)$ and $\bar{n}_y = 0.024(3)$ from the spectrum which correspond to ground-state fractions of $98.1(5)$ % and $97.6(3)$ %, in agreement with fitted values of $98(1)$ % and $95(3)$ % from the Rabi flopping curves [104] in Fig. 3.7A-D. The initial temperature of 80 μK before RSC is obtained from similar fits.

For the weak axial direction where cooling is challenging because the atom starts outside the LD regime, we observe up to 5th-order Raman cooling sidebands initially, which indicates population in highly-excited motional states. Nevertheless, our cooling sequence works efficiently as all the $\Delta n < 0$ sidebands are reduced after RSC (Fig. 3.6C). Using the ratio of first-order sideband heights, we obtain $\bar{n}_z = 0.024(5)$, which corresponds to a ground-state population of $97.6(5)$ %, in agreement with a ground-state population of $95(4)$ % extracted from Rabi flopping when $\Delta n = 0$ (Fig. 3.7E). For the $\Delta n = 1$ side-
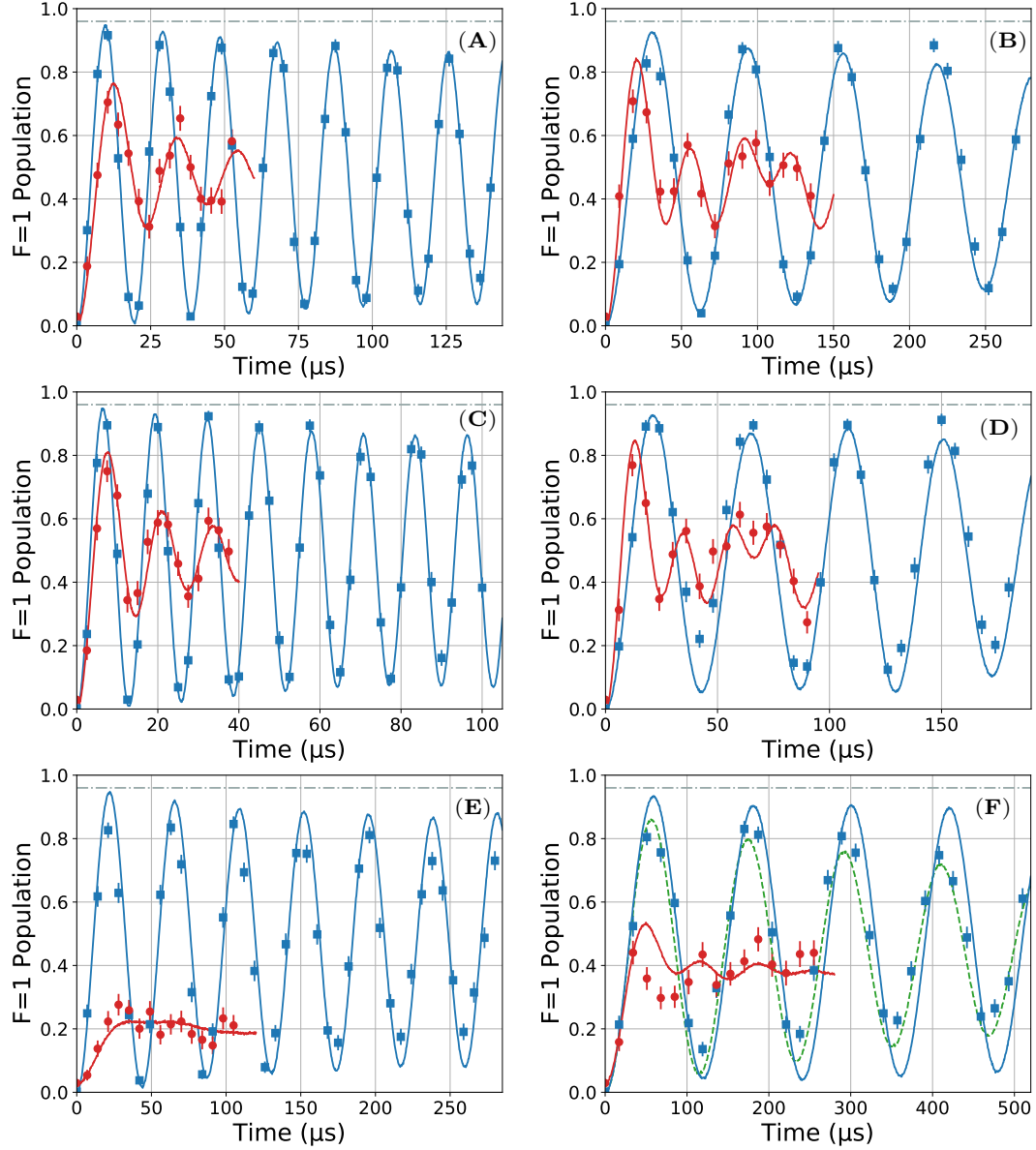
Figure 3.7: Rabi flopping on radial axis x (A) carrier and (B) $\Delta n_x = 1$ sideband, radial axis y (C) carrier and (D) $\Delta n_x = 1$ sideband, axial axis z (E) carrier and (F) $\Delta n_x = 1$ sideband, before (red circle) and after (blue square) Raman sideband cooling. Solid lines (both red and blue) in all plots are fit to a Rabi-flopping that include a thermal distribution of motional states [104] as well as off-resonant scattering from the Raman beams. The blue lines correspond to a ground-state probability of (A-D) 98.1 % along the radial axes and (E-F) 95 % along the axial axis after cooling. The red lines correspond to a thermal distribution of 80 μK before RSC. The horizontal dashed lines in all the plots correspond to the 4 % probability of imaging loss. The green dashed line in (F) includes the additional decoherence due to a fluctuation of the hyperfine splitting of magnitude 3 kHz. We see that the decoherence effect is strongest for the post-cooling data on the axial $\Delta n_z = 1$ sideband where the Rabi frequency is the lowest.

band (Fig. 3.7F), we observe additional decoherence that is more pronounced due to the slower Rabi frequency. The decoherence rate is consistent with magnetic field fluctuations of 1.5 mG measured independently in the lab, which would produce a Zeeman shift of $\approx 3\,\text{kHz}$.

Combining the axial and radial cooling results, a single Na atom is in the 3D ground state with a probability of 93.5(7) % after RSC. The cooling efficiency is limited by spontaneous scattering rate $(0.1 \sim 0.2\,\text{kHz})$ from the Raman beams, as well as spectral broadening from magnetic field fluctuations.

We measure a heating rate that corresponds to decreasing 3D ground-state population at a rate of $\approx 0.9\,\%/\text{ms}$. The rate is consistent with off-resonant scattering of the trapping light [112], and is predominantly in the axial direction where the trapping beam propagates.

Monte-Carlo simulations show that the ground-state probability after RSC could be enhanced by increasing the detuning of the Raman beams and implementing better control of the magnetic field. Another improvement could come from grey molasses cooling, to achieve a lower starting temperature before RSC [113].

We have shown that despite the difficulty in achieving a low optical cooling temperature of low mass sodium atoms, three dimensional cooling with significant ground-state population can be achieved by using high-order Raman sidebands in an optimized cooling sequence. The challenges we face with the cooling of Na atom is shared with a large variety of other systems including exotic atoms and molecules, where the initial temperature and available trapping potential may be limited. The techniques we used are well-suited for these systems and open up a route to ground-state cooling.

In our experiment, the RSC step concludes our full control of the atom quantum states. The atoms are then merged into the same trap adiabatically so that they remain in a single quantum state [99]. This is the starting point for our study of the atom-atom interactions and molecular potentials, as well as the coherent formation of molecules, which will be the focus of the following chapters.

4

Interaction of Single Atoms

The interaction between the atoms is governed by the short range molecular potential. For low energy processes involving atoms with long de Broglie wavelengths, however, the complex short range part of the interaction can be ignored and the collision is approximately described by a single number, the s-wave scattering length a. Measuring the scattering length

79

between the atoms allows us to probe the properties of the molecular potential and refine predictions needed for molecule formation, e.g. the binding energy, without direct observation of the molecular states. Traditionally, such measurements are done either by scattering in bulk gases [19] or by spectroscopy in optical lattices [114–118], both of which require the preparation of many atoms in quantum degeneracy. The preparation of two single atoms in the motional ground state in a single tweezer, however, allows us to cleanly perform this measurement using only two atoms and not be affected by many-body effects that inevitably exist using the traditional approach.

In this chapter, we will discuss our measurement of the interspecies scattering lengths between multiple Na and Cs spin states using interaction shift spectroscopy. We will start in section 4.2 with a theoretical description of two interacting atoms in an optical tweezer. The experimental techniques and the result of the measurement will be described in section 4.3. The discussion here is based on our publication in [119].

4.2   Two Interacting Atoms in Optical Tweezer

The Hamiltonian for two atoms in an harmonic potential with interaction is,

$$
H = \sum_{i=x,y,z} \left(\frac{m_1 \omega_{1,i}^2 r_{1,i}^2}{2} + \frac{p_{1,i}^2}{2m_1} \right) + \sum_{i=x,y,z} \left(\frac{m_2 \omega_{2,i}^2 r_{2,i}^2}{2} + \frac{p_{2,i}^2}{2m_2} \right) + V_{\text{int}}(\mathbf{r}_1 - \mathbf{r}_2) \quad (4.1)
$$

where m_j is the mass of the j-th atom, $r_{j,i}, p_{j,i}, \omega_{j,i}$ are the coordinate, momentum and trapping frequency for the j-th atom along the i-th axis. V_{int} is the interaction potential between the two atoms which is only a function of the relative coordinate between the atoms $\mathbf{r}_1 - \mathbf{r}_2$.

Since the two atoms experience the same trapping light field, their trapping potential has the same center and the same shape. However, due to the difference in the polarizability between the atoms, the trap depth can be different. Nevertheless, in our experiment, depending on the trapping wavelength, we have $\omega_{1,i} \approx \omega_{2,i}$ to within 10 % to 20 % and this is the regime we will mainly focus on in this section.

In order to calculate the interaction term, we can change from the coordinates for the two individual atoms to the center of mass (COM) and relative coordinates.

$$R_i = \frac{m_1 r_{1,i} + m_2 r_{2,i}}{m_1 + m_2} \qquad\qquad r_{\text{rel},i} = r_{1,i} - r_{2,i}$$

$$P_i = p_{1,i} + p_{2,i} \qquad\qquad p_{\text{rel},i} = \frac{m_2 p_{1,i} - m_1 p_{2,i}}{m_1 + m_2}$$

The corresponding masses and trapping frequencies are,

$$M = m_1 + m_2 \qquad\qquad \mu = \frac{m_1 m_2}{m_1 + m_2}$$

$$\Omega_i^2 = \frac{m_1 \omega_{1,i}^2 + m_2 \omega_{2,i}^2}{m_1 + m_2} \qquad\qquad \omega_{\text{rel},i}^2 = \frac{m_2 \omega_{1,i}^2 + m_1 \omega_{2,i}^2}{m_1 + m_2}$$

81

and the Hamiltonian can be expressed as,

$$H = \sum_{i=x,y,z} \left(\frac{M\Omega_i^2 R_i^2}{2} + \frac{P_i^2}{2M} \right) + \left[\sum_{i=x,y,z} \left(\frac{\mu\omega_{\mathrm{rel},i}^2 r_{\mathrm{rel},i}^2}{2} + \frac{p_{\mathrm{rel},i}^2}{2\mu} \right) + V_{\mathrm{int}}(\mathbf{r}_{\mathrm{rel}}) \right]$$
$$+ \sum_{i=x,y,z} \mu\left(\omega_{1,i}^2 - \omega_{2,i}^2\right) R_i r_{\mathrm{rel},i} \tag{4.2}$$

The first term and the second term only rely on the COM motion and relative motion respectively and can be solved independently. The third term mixes the COM and relative motion and is proportional to the difference in trapping frequency. If the trapping frequencies are the same for the two atoms, the third term is 0 and the solution is fully separable. As mentioned above, since the trapping frequencies for the two atoms are similar, we will assume the mixing term is small and treat it as a small correction in the calculation.

The interaction potential V_{int} gives rise to the molecular bound states and its exact form will be discussed in chapter 5, 6 and 7. However, since the range of the potential is much smaller than the size of the atomic wavefunction, we can ignore the short range details of the potential and treat it as a contact interaction characterized only by the scattering length a [120],

$$V_{\mathrm{int}}(\mathbf{r}) = \frac{2\pi\hbar^2 a}{\mu} \delta_{\mathrm{reg}}(\mathbf{r})$$

where $\mu = m_1 m_2/(m_1 + m_2)$ is the reduced mass and $\delta_{\mathrm{reg}}(\mathbf{r}) \equiv \delta^{(3)}(\mathbf{r})(\partial/\partial r)r$ is the regularized delta-function. This pseudo-potential is valid when the van der Waals length $\beta_6 =$

$(2\mu C_6/\hbar^2)^{1/4}$ is much smaller than the relative harmonic oscillator lengths $\beta_{\mathrm{rel},i}$ [121, 122]. In our experiment, these are $\beta_6 \approx 6$ nm, $\beta_{\mathrm{rel},x} \approx \beta_{\mathrm{rel},y} \approx 66$ nm for the radial axes, and $\beta_{\mathrm{rel},z} \approx 158$ nm for the axial axis.

4.2.1   PERTURBATIVE CALCULATION

For weak interaction, i.e. a small scattering length a, the effect of the interaction on the energies can be calculated perturbatively. The result from this calculation is useful for checking the validity of the full calculation, as well as providing an intuitive understanding of the shift and its dependence on different parameters.

For simplicity, we will assume all the trapping frequencies are the same, i.e. $\omega_{1,i} = \omega_{2,i} = \omega_{\mathrm{rel},i} = \Omega_i = \omega_i$, so that we only need to consider the relative motion,

$$H_{\mathrm{rel}} = \sum_{i=x,y,z} \left(\frac{\mu \omega_i^2 r_{\mathrm{rel},i}^2}{2} + \frac{p_{\mathrm{rel},i}^2}{2\mu} \right) + V_{\mathrm{int}}(\mathbf{r}_{\mathrm{rel}})$$

When treating the interaction as perturbation, the base solution is the harmonic oscillator

states for the relative motion $|n_{\mathrm{rel},x}, n_{\mathrm{rel},y}, n_{\mathrm{rel},z}\rangle$. The energy level perturbation is then,

$$
\begin{aligned}
\Delta_{n_{\mathrm{rel},x},n_{\mathrm{rel},y},n_{\mathrm{rel},z}} &= \langle n_{\mathrm{rel},x}, n_{\mathrm{rel},y}, n_{\mathrm{rel},z} | V_{\mathrm{int}}(\mathbf{r}_{\mathrm{rel}}) | n_{\mathrm{rel},x}, n_{\mathrm{rel},y}, n_{\mathrm{rel},z} \rangle \\
&= \frac{2\pi\hbar^2 a}{\mu} \langle n_{\mathrm{rel},x}, n_{\mathrm{rel},y}, n_{\mathrm{rel},z} | \delta_{reg}(\mathbf{r}_{\mathrm{rel}}) | n_{\mathrm{rel},x}, n_{\mathrm{rel},y}, n_{\mathrm{rel},z} \rangle \\
&= \frac{2\pi\hbar^2 a}{\mu} \left| \psi_{n_{\mathrm{rel},x},n_{\mathrm{rel},y},n_{\mathrm{rel},z}}(0) \right|^2
\end{aligned}
\tag{4.3}
$$

where $\left| \psi_{n_{\mathrm{rel},x},n_{\mathrm{rel},y},n_{\mathrm{rel},z}}(0) \right|^2$ is the probability density for zero distance between the atoms.

For the motional ground state, the shift is,

$$
\Delta_{0,0,0} = a\frac{2\hbar^2}{\mu\sqrt{\pi}} \prod_{i=x,y,z} \frac{1}{\beta_{\mathrm{rel},i}}
$$

where $\beta_{\mathrm{rel},i} \equiv \sqrt{\hbar/\mu\omega_{\mathrm{rel},i}}$ is the relative motion oscillator length along the i-th axis. The shift is proportional to the strength of the interaction a, and is also bigger for stronger confinement where the wavefunction density is higher.

We can see from Eq. 4.3 that the shift is only non-zero when all of $n_{\mathrm{rel},i}$'s are even. The shift is also smaller for higher motional excited states with lower wavefunction density at $\mathbf{r}_{\mathrm{rel}} = 0$. This means that the shift will only be observable if the atom is cooled to close to the motional ground state and will be small or zero for other states.

4.2.2 NON-PERTURBATIVE CALCULATION

The first order perturbative result breaks down for large a when the energy shift approaches the motional energy scale $\omega_{\mathrm{rel},i}$. Moreover, due to the divergent nature of the delta-function in the contact interaction potential, higher order perturbative calculations do not converge. It is therefore necessary to use a non-perturbative solution of the interacting atoms in order to interpret measurements of the shift for strong interaction. To do this, we first ignore the last term in the Hamiltonian 4.2 so that it is fully separable into COM and relative motion. This term, along with a few other corrections, will be added later numerically to obtain the full solution.

For the relative Hamiltonian, we use the analytical cylindrical solutions from Ref. [123]. These solutions require the potential to be cylindrically symmetric and that the ratio between the radial trapping frequency and the axial trapping frequency $\eta \equiv \omega_{\mathrm{radial}}/\omega_z$ to be an integer. We therefore define $\eta = 6$, which is close to the actual values of 5.6 and ignores the 7 % difference between the two radial trapping frequencies in order to use these solutions. These differences from the real Hamiltonian will be included later as a correction [124, 125].

Moreover, Ref. [123] does not provide the wavefunctions for the full solution, but only include the ones for the interacting states. In order to use the solution, we must expand it to include the non-interacting states as well. We have identified these states from the pertur-

bative calculation in section 4.2.1 which are the ones witch at least one odd $n_{rel,i}$. In order to match the analytical solution, we can transform to the cylindrical harmonic oscillator basis. The eigenenergies becomes

$$\frac{E_{n,l,m_z}}{\hbar\omega_z} = (2n + |l| + 1)\eta + (m_z + 1/2) \tag{4.4}$$

where n is the principal quantum number for the radial part, l is the angular momentum quantum numbers for the radial part, and m_z is quantum number for the axial 1D harmonic oscillator. The condition for non-interacting states becomes $l \neq 0$ or odd m_z. However, when η is an integer, as is required by the solution of the interacting states, there is a subspace of cylindrical harmonic oscillator states with $l = 0$ and even m_z that are degenerate from Eq. 4.4. This accidental degeneracy reduces the number of interacting states such that within each degenerate subspace with N_{deg} states, there is only one interacting state and the rest $N_{deg} - 1$ states are non-interacting. We can express a non-interacting state $\psi_{non-int}$ within this subspace as a superposition of the cylindrical harmonic oscillator states $\psi_{non-int} = \sum_i c_i \psi_i$, where the sum is over all the spaces in the degenerate subspace. The state must satisfy the condition $V_{int}\psi_{non-int} = 0$ or $\psi_{non-int}(\mathbf{r}_{rel} = 0) = 0$. We find these amplitudes c_i using a Gram-Schmidt procedure, based on the requirement $\sum_{i=1}^{N_{deg}} c_i \psi_i(\mathbf{r}_{rel} = 0) = 0$. The procedure identifies $N_{deg} - 1$ non-interacting states within the subspace which is combined with the interacting state from Ref. [123] to form the full

solution.

For the interacting states, the energies are given by the transcendental equations [123]

$$\mathcal{F}\left(-\frac{(E-E_0)}{2}, \eta\right) = -\frac{\sqrt{2\pi}}{a}$$

where $\mathcal{F}(x, \eta)$ is given by

$$\mathcal{F}(x, \eta) = \frac{\sqrt{\pi}\Gamma(x)}{\Gamma(x + \frac{1}{2})} \sum_{m=1}^{n-1} F\left(1, x; x + \frac{1}{2}; e^{\mathrm{i}(2\pi m/\eta)}\right) - \frac{2\sqrt{\pi}\Gamma(x)}{\Gamma(x - \frac{1}{2})}$$

Here $F(a, b; c, x)$ denotes the hypergeometric function and $\Gamma(x)$ is the Euler gamma function. The energy E and E_0 are in units of the axial trapping frequency ω_z, and so the ground-state energy $E_0 = \eta + 1/2$.

The COM Hamiltonian is a cylindrical harmonic oscillator and the energy is given by Eq. 4.4.

Now that we have the solution in the separable and cylindrical case, the next step is to include the correction terms from the effects that were ignored above. These include the COM and relative motion mixing term from the Hamiltonian 4.2, the asymmetry of the two radial axis, and the effect of non-integer η. The total matrix is diagonalized in the combined COM and relative cylindrical bases. Compared to treating the interaction term in Eq. 4.1 as a perturbation, the correction terms included here all have the form of harmonic
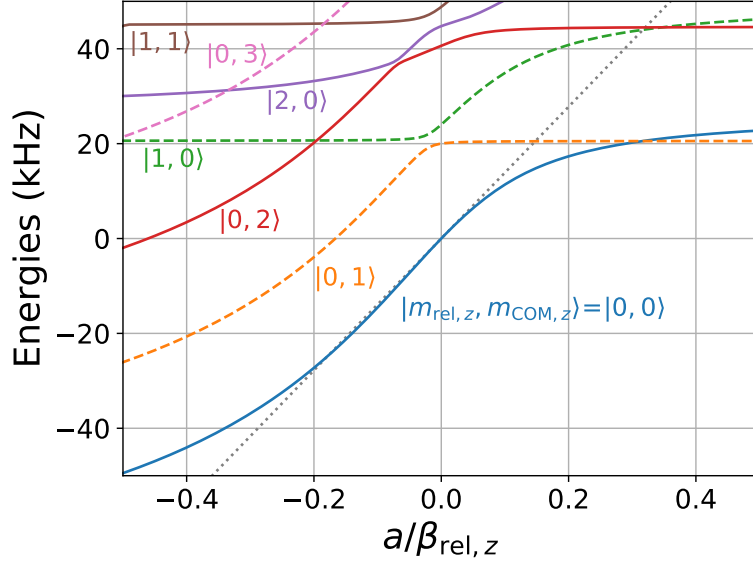
Figure 4.1: Energy levels as a function of scattering length (in unit of the axial relative motion oscillator length $\beta_{rel,z}$) from the non-perturbative calculation. The dashed straight light is the result from first order perturbation for the motional ground state which shows good agreement with the exact calculation at small scattering length. Only states that are in the radial motional (both relative and COM) ground state are shown because of the high radial motional energy scale (100 kHz). The states are labeled with their relative and COM axial motional quantum numbers $m_{rel,z}$ and $m_{COM,z}$. Due to the relative and COM motion mixing term and the resulting avoided crossings in the energy levels, these are not the true quantum numbers and are not constants along the same line. The numbers shown in the plot are for the state at large negative scattering length. States with even total parity, i.e. $m_{rel,z} + m_{COM,z}$, are plotted in solid lines whereas ones with odd total parity are plotted in dashed lines. Since the Hamiltonian conserves total parity, there is no coupling between the two sets of states which results in the level crossing shown in the plot.

potentials and therefore have much better convergence behavior. We include all states with energies up to $20\omega_{\mathrm{rel},z}$ in the calculation. The matrix elements are calculated numerically using the cylindrical wavefunctions, which for completeness are given here:

$$\Psi_{n,l,m_z}(\rho,\theta,z) = \Psi_{n,l}^{\mathrm{radial}}(\rho,\theta)\Psi_{m_z}^{\mathrm{axial}}(z)$$

with the normalized radial harmonic oscillator wavefunction,

$$\Psi_{n,l}^{\mathrm{radial}}(\rho,\theta) = \sqrt{\frac{2n!}{a_\perp^2(n+|l|)!}}\,e^{-r^2/(2a_\perp^2)}\left(\frac{r}{a_\perp}\right)^{|l|}L_n^{|l|}\left(\frac{r^2}{a_\perp^2}\right)\frac{e^{il\theta}}{\sqrt{2\pi}}$$

and the normalized 1D harmonic wavefunction,

$$\Psi_{m_z}^{\mathrm{axial}}(z) = \frac{1}{\sqrt{2^{m_z}m_z!}}\frac{1}{\sqrt{a_z}(\pi)^{1/4}}e^{-z^2/(2a_z)}H_{m_z}(z/a_z)$$

Here the radial and axial oscillator lengths are defined as $a_\perp = \sqrt{\hbar/(\mu\omega_\perp)}$ and $a_z = \sqrt{\hbar/(\mu\omega_z)}$. H_{m_z} are the Hermite-Gaussian functions, and $L_n^{|l|}$ are the generalized Laguerre polynomials.

The eigenenergies of the matrix are calculated as a function of the scattering length. The results for the lowest energy ones are shown in Fig. 4.1.

Figure 4.2: Schematics of interaction shift spectroscopy using Raman transitions. Left: Raman resonance for atomic spin flip with only one atom in the tweezer. Right: The energy shifts by a spin state dependent amount with the present of the second (red) atom. This causes a shift in the spin flip resonance frequency for the first (green) atom compared to the one atom case. The shift corresponds to the difference in the interaction shift between the two spin states.

4.3   Interaction Shift Spectroscopy

4.3.1   Experiment Sequence

The absolute energies shown in Fig. 4.1 have an arbitrary global offset and are therefore

not directly measurable. Instead, the measurable quantities are the energy differences be-

tween different states, which can be done either by changing the scattering length, i.e. mov-

ing along the x axis in Fig. 4.1, or by changing the motional state of the atoms, i.e. moving

along the y axis.

In our experiment, we measure the interaction shifts by flipping the spin state of one but

not the other atom using Raman transitions. Since the scattering length depends on the spin state, the interaction shift may be different between the initial and final spin states. We measure this difference by comparing the resonance frequency in the absence of the other atom (Fig. 4.2). The spin flip is done in the same 8.8 G we use for Raman sideband cooling (section 3.4). We drive the transition using two Raman beams that are co-propagating which imprints no phase gradient on the atomic wavefunction (section 3.2.1). This reduces the number of observable resonances and provides a cleaner spectrum since,

1. Parity is conserved during the transition.
   Starting from the motional ground state, this means that all dashed lines in Fig. 4.1 are uncoupled.

2. Coupling to different motional states are surppressed.
   In particular, this reduces the coupling to COM motional excitation in the strong interaction limit. Note that since the interaction between the atoms modifies the wavefunction, there is still non zero overlap between different motional states especially for the relative motion.

4.3.2 Results

The spectrum for the $|Na(2, 2), Cs(4, 4)\rangle$ to $|Na(2, 2), Cs(3, 3)\rangle$ transition is shown in Fig. 4.3A. The orange line shows the bare $|Cs(4, 4)\rangle$ to $|Cs(3, 3)\rangle$ resonance without the presence of the Na atom whereas the blue line shows the resonances including the interaction with the Na atom. The largest peak on the left is the shifted ground motional
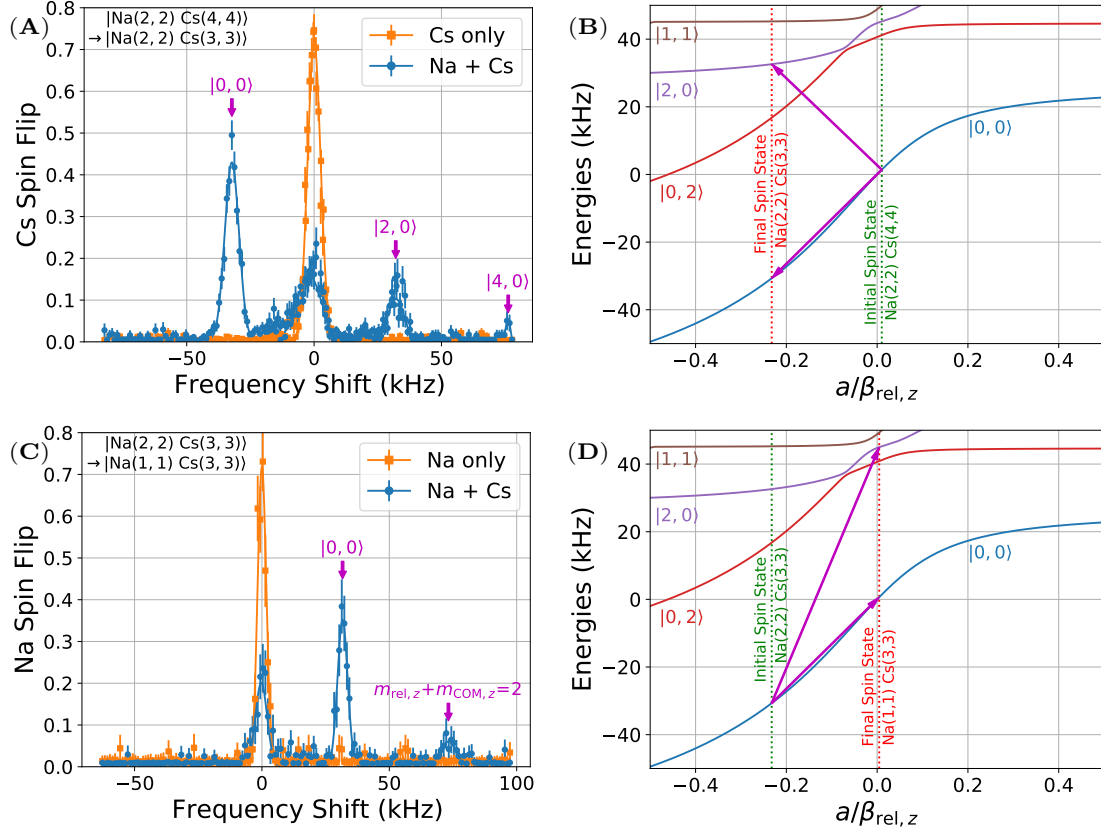
Figure 4.3: Interaction shift measurement for (A) $|Na(2,2), Cs(4,4)\rangle \rightarrow |Na(2,2), Cs(3,3)\rangle$ and (C) $|Na(2,2), Cs(3,3)\rangle \rightarrow |Na(1,1), Cs(3,3)\rangle$ with the corresponding transition shown on the energy map from theoretical calculation in (B) and (D) respectively. The orange line shows the bare resonance with only one atom in the trap and the blue line shows the spectrum including interaction shift. A resonance appearing at positive frequency shift corresponds to the final state having a more positive energy (more repulsive interaction or higher motional energy). More than one shifted peaks can be observed due to the motional state mixing caused by the interaction. The corresponding motional state is marked as $|m_{rel,z}, m_{COM,z}\rangle$ on the resonance. For the $|Na(2,2), Cs(3,3)\rangle \rightarrow |Na(1,1), Cs(3,3)\rangle$ transition (C and D), the states with two quanta of total axial excitation are unresolved. Since the Raman transition preserves parity, only states with even parity are shown in (B) and (D).

Table 4.1: Interaction shift and scattering lengths for different spin states. The number for the $|\mathrm{Na}(2,2),\mathrm{Cs}(4,4)\rangle$ is computed from the binding energy of the molecular state whereas the other numbers are measured by the interaction spectroscopy.

Spin state	Interaction Shift (kHz)	Scattering Length
$|\mathrm{Na}(2,2),\mathrm{Cs}(4,4)\rangle$	1.40	$30.4a_0$
$|\mathrm{Na}(2,2),\mathrm{Cs}(3,3)\rangle$	-30.7	$-693.8a_0$
$|\mathrm{Na}(1,1),\mathrm{Cs}(3,3)\rangle$	0.62	$13.7a_0$

state $|m_{\mathrm{rel},z}, m_{\mathrm{COM},z}\rangle = |0,0\rangle$ and the smaller peak on the right corresponds to the $|2,0\rangle$

state (Fig. 4.3B). A even smaller resonance for $|4,0\rangle$ is also visible further right (not shown

in Fig. 4.3B). The $|0,0\rangle$ resonance gives the difference of the interaction shifts of the initial

and final spin states, $E(\mathrm{Na}(2,2),\mathrm{Cs}(3,3)) - E(\mathrm{Na}(2,2),\mathrm{Cs}(4,4)) = -32.1(2)$kHz.

The peak near zero frequency corresponds to the initial Na and Cs population that is not

prepared in the motional ground state or an interacting state. The fitted height 0.46 of the

$|0,0\rangle$ peak serves as a lower bound for the relative motional ground-state population. Sim-

ilarly, Fig. 4.3C shows the result for the $|\mathrm{Na}(2,2),\mathrm{Cs}(3,3)\rangle$ to $|\mathrm{Na}(1,1),\mathrm{Cs}(3,3)\rangle$ mea-

sured by driving a Na Raman transition. Two interaction shifted resonances were observed

which corresponds to the motional ground state and unresolved states with two total Na

and Cs motional excitation (Fig. 4.3D).

Since the measurement only gives the energy difference between spin state combina-

tions with different scattering lengths, we determine an absolute interaction shift of the

$|\mathrm{Na}(2,2),\mathrm{Cs}(4,4)\rangle$ using the binding energy of the least bound state $v'' = -1$ (sec-

tion 6.2.2). The absence of spin mixing for this state allows its binding energy to be related

to the scattering length directly through single-channel quantum defect theory (QDT) [126–128] but extended to two-scale by including the $-C_8/r^8$ potential. For the van der Waals coefficients, we use $C_6 = 3227$ a.u. and $C_8 = 3.681 \times 10^5$ a.u. from Refs. [129–131]. From here, we can use the result of the calculation above to obtain all the absolute interaction shifts and scattering lengths, summarized in table 4.1.

4.4 Summary and Outlook

Optical tweezers provide a clean platform to study the interaction between exactly two atoms. Here, we started our exploration of the interaction by measuring the most important quantity for s-wave scattering process at ultracold temperature, the scattering length a. The results from these measurements can be used to refine the theoretical model of the NaCs molecule, including predictions of the molecule binding energy and Feshbach resonances [119]. More properties of the interaction will be studied in the following chapters.

Additionally, the combination of the tight confinement from the optical tweezer and the interaction between the atoms also gives us further control of the motional states of the atom. As we have seen in this chapter, the degeneracy of carrier Raman transition for different motional states is lifted by the interaction. As a result, driving on the interaction shifted resonance allows us to prepare a system that is completely in the ground state of the relative motion. This will be used when we coherently create the molecules (chapter 7) to

lower the requirement for the cooling and reduce the background caused by hot atoms.

5

Photoassociation of Single Atoms

5.1 Introduction

The method we use to coherently create a single molecule from atoms uses a two-photon optical transition (chapter 7). Before we can drive such a transition, however, we must locate and characterize the intermediate excited states of the molecule to be used in the two-photon transition. This can be measured using photoassociation (PA) spectroscopy where

two atoms are driven from the atomic state to an excited molecular state via an optical transition. The flexibility of the optical tweezer platform allows us to prepare a clean initial state with only two atoms and accurately detect when PA has happened with a high signal to noise ratio (section 5.3.2).

In this chapter, we describe the molecular energy structure (section 5.2) and how we use PA spectroscopy to locate and identify the molecular excited states (section 5.3). We give details on the beam path for the measurement including the alignment procedure for the PA beam (section 5.3.1) and discuss about factors that can affect the PA linewidth (section 5.3.3).

5.2 Energy Levels

First we will discuss the energy levels in a diatomic molecule as well as the labeling convention for the states. We will focus mainly on the electronic excited states measured in this chapter but most of the discussion here applies to ground electronic states as well and will be useful for chapter 6 and 7.

5.2.1 Angular Momentum States

Compared to an atom, a diatomic molecule has many more degrees of freedom. In addition to the quantum numbers for each atom in the molecule, molecules also have nuclear motion. In order to reduce the complexity, it is therefore very important to consider the

symmetries of the system, and in particular the angular momentum, which corresponds to rotational symmetry, and the coupling between them. The angular momenta in a diatomic molecule include electron orbit $\mathbf{L}^{\ddagger}$, electron spin $\mathbf{S}_1$ and $\mathbf{S}_2$, nuclear orbital $\mathbf{N}$ and nuclear spin $\mathbf{I}_1$ and $\mathbf{I}_2$. Although the total angular momentum $\mathbf{F} \equiv \mathbf{L} + \mathbf{S}_1 + \mathbf{S}_2 + \mathbf{N} + \mathbf{I}_1 + \mathbf{I}_2$ is the only true conserved quantity in the absence of external fields, depending on the coupling strengths between the angular momenta, there are additional approximately conserved quantities in the molecule.

For the NaCs molecule and our experiment, there are two important regimes where the coupling strength can be easily ordered.

5.2.1.1 Deeply Bound States

This is described by the Hund's case (a) [132, p. 523-626]. Molecular states with large binding energies mostly experience interactions between the atoms at short range where the electrostatic interaction is very strong. This couples the two electron spins into a total electronic spin $\mathbf{S} \equiv \mathbf{S}_1 + \mathbf{S}_2$ via a very strong effective interaction of the form $\mathbf{S}_1 \cdot \mathbf{S}_2$ which originates from the resulting symmetry of the electron orbital wavefunction. Similar to atoms, the nuclear spin interaction is also very weak compared to other energy scales so we can ignore the hyperfine structure and only need to consider $\mathbf{J} \equiv \mathbf{L} + \mathbf{S} + \mathbf{N}$.

---

‡There are $\mathbf{L}_1$ and $\mathbf{L}_2$ for the two electrons but since we only consider states with at most one $\mathbf{L}_i \neq 0$ we will only use one quantum number here
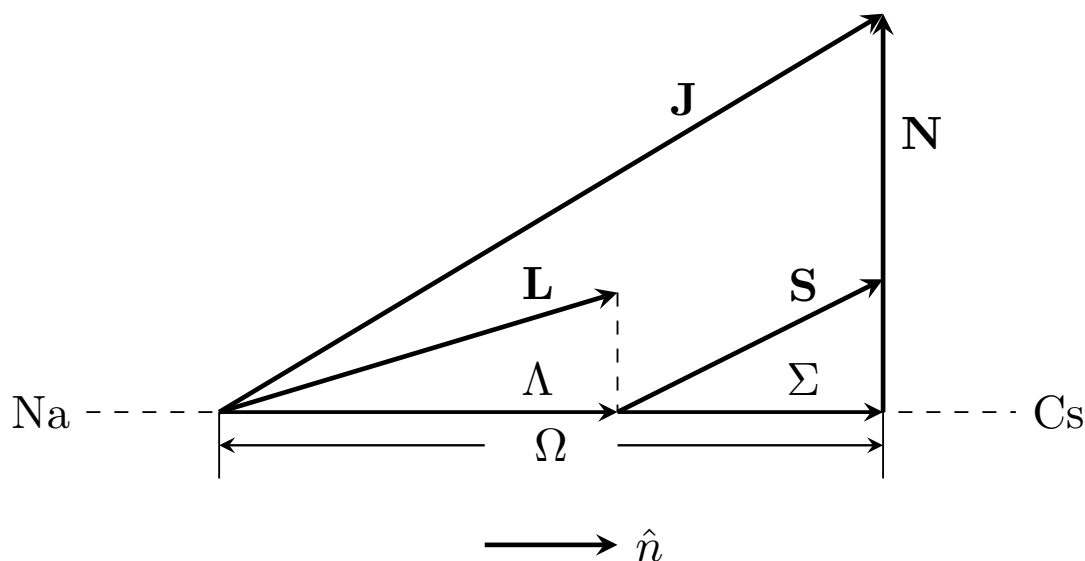
Figure 5.1: Angular momentum coupling for Hund's case (a). **L** and **S** are coupled to the internuclear axis $\hat{n}$ and the sum of the projections $\Omega = \Lambda + \Sigma$ is then added with the orthogonal component **N** to form **J**.

The strong electrostatic interaction also creates an effective coupling between the **L** and **S** with the internuclear axis $\hat{n}$ causing **L** and **S** to process rapidly around $\hat{n}$. This creates two new conserved quantities Λ and Σ as the projection of **L** and **S** along $\hat{n}$ respectively. The total angular momentum along $\hat{n}$ is therefore $\Omega \equiv \Lambda + \Sigma$ and it is added to the **N** which is orthogonal to $\hat{n}$ to form the total angular momentum **J** (Fig. 5.1).

The angular momentum state of the molecule is therefore fully characterized by $|L, \Lambda, S, \Omega, J\rangle$. Λ can be $0, 1, \ldots, L$, Ω ranges from $|\Lambda - S|$ to $\Lambda + S$ and $J \geqslant \Omega$. The L quantum number is specified by the electronic state and will be discussed in section 5.2.2. The rest of the an-

gular momentum quantum numbers are represented by the Hund's case (a) term symbol,

$$^{2S+1}\Lambda_\Omega$$

similar to the atomic term symbol $^{2S+1}L_J$. Just as the use of capital English letters $S, P, D, \ldots$ are used to represent $L = 0, 1, 2, \ldots$, capital Greek letters $\Sigma, \Pi, \Delta, \ldots$ are used to denote $\Lambda = 0, 1, 2, \ldots$ in the term symbol. An additional symmetry to consider is the reflection about a plane that includes the internuclear axis. For $\Lambda > 0$ states, the reflection produces a new state at the same energy creating the so-called Λ-doubling. For $\Lambda = 0$ states, i.e. Σ states, the reflection produces the same state with a phase of ± 1. This phase is also included in the term symbol to fully specify the symmetry of a Σ states as

$$^{2S+1}\Sigma_\Omega^\pm$$

Note the Σ state here should not be confused with the quantum number Σ.

From the angular momentum relation in Fig. 5.1, we can also determine the energies of different rotational states. The nuclear rotational energy is given by,

$$E_{rot} = B\langle \mathbf{N}^2 \rangle$$

where B is the rotational constant of the molecule. For Hund's case (a) this is,

$$E_{rot} = B\langle \mathbf{J}^2 - \Omega^2 \rangle$$
$$= B\langle \mathbf{J}^2 - \Omega^2 \rangle$$
$$= B\big(J(J+1) - \Omega^2\big)$$

For the last step, note that Ω is not an angular momentum vector but a projection. We can easily see that for a given Ω, we have $J \geqslant \Omega$. Unlike a rigid rotor where $E_{rot} = BN(N+1)$, the limit on the J means that the spacing between the rotational levels depend on Ω,

$$2\Omega + 2, \ 2\Omega + 4, \ 2\Omega + 6, \ \ldots$$

This allows us to determine the Ω of the state we are addressing by measuring the state spacing for the lowest few rotational states.

5.2.1.2 Near Threshold Bound States

For molecular states with a small binding energy, the interaction between the two atoms is small compared to the internal coupling in the atoms and the angular momentum coupling is "atom like". In this limit, the total angular momentum $\mathbf{F}_1$ and $\mathbf{F}_2$ for the individual atoms forms $\mathbf{F}_{atom} = \mathbf{F}_1 + \mathbf{F}_2$ which is then coupled to the nuclear rotation $\mathbf{N}$ to form

$\mathbf{F} = \mathbf{F}_{\text{atom}} + \mathbf{N}$. We will discuss this regime in more detail when we characterize the weakly bound ground states in chapter 6.

5.2.2 Potential Energy Surface

Due to the different angular momentum coupling in different regimes, there is not a consistent way to label the interaction between the two atoms at both short and long distance. Nevertheless, by convention, we use the Hund's case (a) term symbol since it more accurately represents the state when the interaction energy dominates.

The Hamiltonian (excluding spin for simplicity[‡]) is,

$$H = H_e + T_n$$

where the electronic term H_e and the nuclear kinetic term T_n are given by

$$H_e = -\sum_i \frac{\hbar}{2m_e}\nabla_i^2 + \frac{e^2}{4\pi\varepsilon_0}\left(\sum_{i>j}\frac{1}{|\mathbf{r}_i - \mathbf{r}_j|} - \sum_{A=\text{Na,Cs}}\sum_i \frac{Z_A}{|\mathbf{r}_i - \mathbf{R}_A|} + \frac{Z_{\text{Na}}Z_{\text{Cs}}}{|\mathbf{R}_{\text{Cs}} - \mathbf{R}_{\text{Na}}|}\right)$$

$$(5.1)$$

$$T_n = -\sum_{A=\text{Na,Cs}} \frac{\hbar^2}{2m_A}\nabla_A^2$$

and the sum is over all the electrons in the molecule.

[‡]Electron spin is implicitly included, however, via the symmetry of the electronic wavefunction.

5.2.2.1 Born-Oppenheimer Approximation

The Hamiltonian is solved using the Born-Oppenheimer (BO) approximation. Because of the large mass difference between the nuclei and the electrons, we can assume that the electron motion follows the position of the nuclei instantaneously so that the motion of the nuclei and the electrons can be treated separately. Formally, this means that the electron wavefunctions is solved using the electronic term H_e for a given nuclear position $\mathbf{R}_{Na}$ and $\mathbf{R}_{Cs}$. This results in an effective potential $V_{eff}(|\mathbf{R}_{Na} - \mathbf{R}_{Cs}|)$ called the potential energy surfaces (PES) for each electronic states. The solutions to the approximate Hamiltonians $T_n + V_{eff}$ provide the vibrational and rotational states of the molecule.

5.2.2.2 Franck-Condon Factor

In addition to the energy of the molecular bound state, the solution of the nuclear motion also provides information on the selection rules and coupling strength of transitions between the states. For an electronic electric dipole transition between states $|e_1, v_1, j_1\rangle$ and $|e_2, v_2, j_2\rangle$, where e_i, v_i and j_i denotes electronic, vibrational and angular momentum states, respectively the Rabi frequency under the BO approximation is,

$$\begin{aligned}
\Omega &= \langle e_1, v_1, j_1 | e\mathbf{r}_e \cdot \mathbf{E}e^{i\mathbf{k}\cdot\mathbf{r}} | e_2, v_2, j_2 \rangle \\
&= \langle e_1(\mathbf{r}) | e\mathbf{r}_e \cdot \mathbf{E} | e_2(\mathbf{r}) \rangle \langle v_1, j_1 | e^{i\mathbf{k}\cdot\mathbf{r}} | v_2, j_2 \rangle
\end{aligned}$$

where $\mathbf{r}$ and $\mathbf{r}_e$ are the molecule and electron coordinates. For most of the transitions, we can treat the nuclear coordinate dependent transition dipole moment $\mathbf{D}(\mathbf{r}) \equiv \langle e_1(\mathbf{r})|e\mathbf{r}_e|e_2(\mathbf{r})\rangle$ as a constant $\mathbf{D}$. Since the size of the molecular wavefunction is also usually much smaller than the wavelength of the transition, we can also assume $e^{i\mathbf{k}\cdot\mathbf{r}} \approx 1$, so we have,

$$\Omega = \mathbf{D} \cdot \mathbf{E}\langle j_1|j_2\rangle\langle v_1|v_2\rangle$$

The term $\langle j_1|j_2\rangle$ determines the angular momentum selection rule which is $\Delta\Lambda = 0, \pm1$, $\Delta S = \Delta\Sigma = 0, \Delta\Omega = 0, \pm1$ and $\Delta J = 0, \pm1$ for Hund's case (a) [133, p. 14-15]. The term $\langle v_1|v_2\rangle$ gives the coupling strength between vibrational states[‡]. This is called the Franck-Condon principle and the square of the wavefunction overlap is defined as the Franck-Condon factor (FCF),

$$\text{FCF} \equiv |\langle v_1|v_2\rangle|^2$$

For incoherent transition, the transition rate is proportional to $\Omega^2 \propto \text{FCF}$.

[‡]Note that $\langle v_1|v_2\rangle$ does not simplify to orthogonality relation when $e_1 \neq e_2$ since the vibrational wavefunctions belong to different PES.
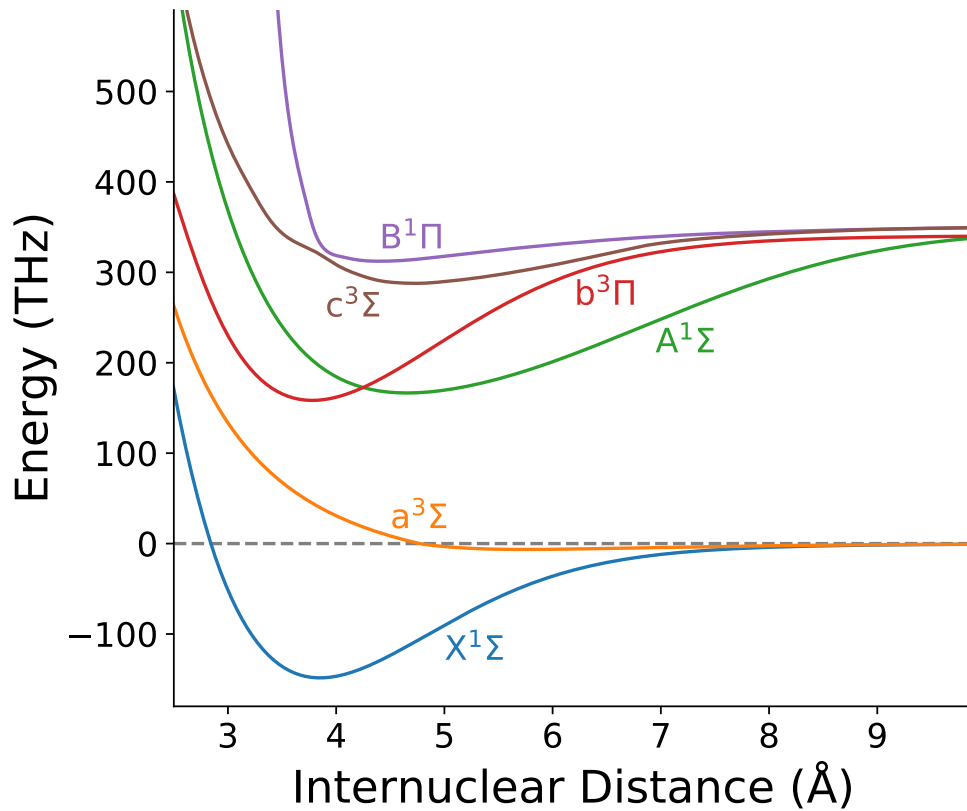
Figure 5.2: Potential energy surfaces of NaCs with Hund's case (a) labels [129, 134–136]. Due to spin-orbit coupling, the potentials are not independent of each other. The real energy eigenstates of the molecule may be a superposition of multiple electronic and spin states.

5.2.2.3 Energy Levels of NaCs

Fig. 5.2 shows the relevant PESs for NaCs. Although the spin-less electronic Hamiltonian 5.1 makes it easier to understand the molecule structure and provides good approximations for the transition dipole moment and FCF, the absence of spin and the difficulty in exactly solving a multi-electron system makes it unsuitable to calculate energy levels for spectroscopy purposes. Because of this, prediction of the molecular-state energies are calculated using PESs fitted to experimental data [129, 134–136].

5.3 Photoassociation Spectroscopy

5.3.1 Beam Path

The excited molecular state we would like to address has a bond length of $3 \sim 8$ Å. The initial atomic state, however, has an average inter-nuclear distance of ≈ 1000 Å. This size mismatch between the wavefunctions of the initial and final state means the transition typically has a very small FCF ($10^{-10} \sim 10^{-8}$). Because of this, we focus our PA beam onto the tweezer with a beam waist between 10 μm and 30 μm (Fig. 5.3) in order to increase the laser intensity and improve the signal contrast. The tight focus also increases the astigmatism when passing through the glass cell window at an angle which limits the minimum focus size we can achieve. Therefore, we added a correction glass plate to fix the astigmatism in order to minimize the focus size and maximize the beam intensity.
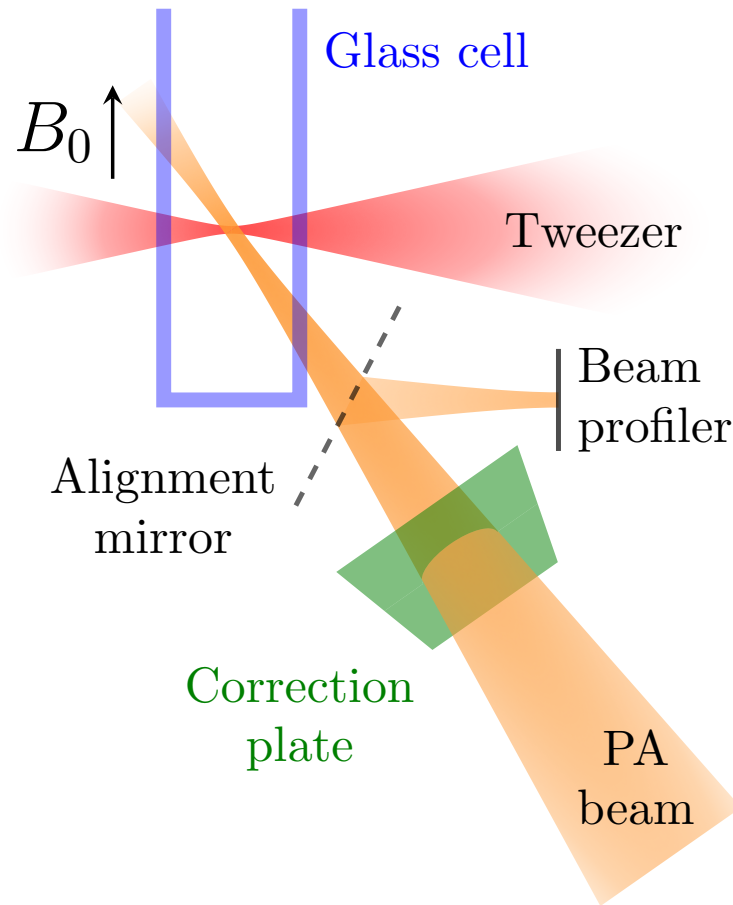
Figure 5.3: PA beam path including the relative passing with the 8.8 G magnetic field, the glass vacuum cell and the tweezer. In order to compensate for the astigmatism from passing through the glass cell window at an angle, we added a correction glass plate into the PA beam path. The correction plate has the same thickness and angle of incident with the glass cell window but is angled vertically instead of horizontally. The alignment mirror and the beam profiler can also be added to the beam path in order to measure the chromatic error during alignment.
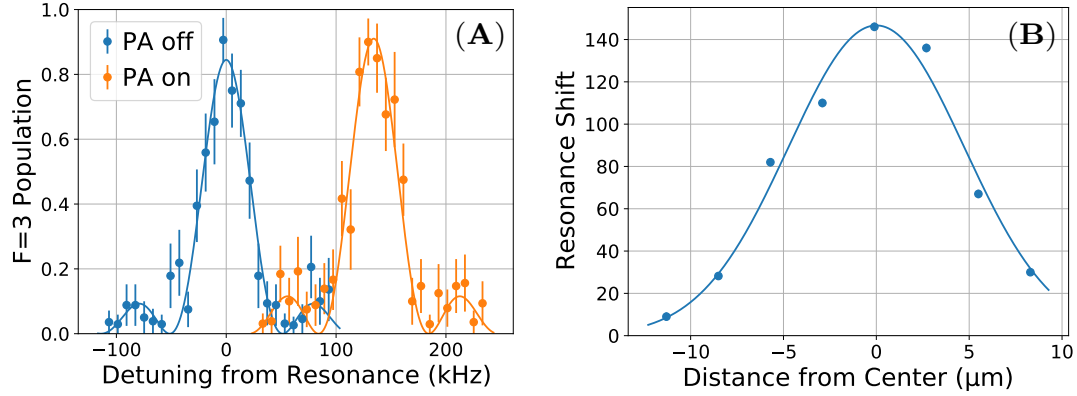
Figure 5.4: Measurement of Cs vector light shift from the PA beam for final alignment. (A) The effective magnetic field from the circularly polarized PA beam causes a shift on the Raman resonance between the $|4, 4\rangle$ and $|3, 3\rangle$ states. (B) Vector light shift as a function of PA beam position used to determine the beam center. The $1/e$ diameter of the beam is measured to be $13.40(72)$ μm.

In order to align the PA beam to the tweezer, we use the following alignment procedure,

1. Light resonant with the Cs atomic transition is sent into the PA beam path. This allows us to do the alignment using the procedure we used to align the atomic Raman sideband cooling beams as described in section 3.8. However, unlike the alignment for the atomic Raman beams, due to the larger frequency difference between the PA transition and the Cs atomic transition as well as the smaller beam size, we cannot use the alignment result from this step directly for the PA beam due to the chromatic aberration from the optics in the PA beam path.

2. In order to translate the alignment result from resonance Cs light to that of the PA light, we insert a mirror to reflect the PA beam after the last optics in the beam path and place a beam profiler at the equivalent location of the tweezer (Fig. 5.3). This allows us to directly measure location of the focal point for the two wavelengths and correct for the chromatic aberration by shifting the focus from the PA light to the original focus position from the resonant Cs light.

3. As the final alignment step and to correct for the chromatic aberration of the glass window that was not corrected for in the last step, we align the PA beam to the atom

Table 5.1: Prediction of $|\mathrm{Na}(2,2),\mathrm{Cs}(4,4)\rangle$ PA resonance frequency based on Dunham expansion [135, 137].

Vibrational State	$v' = 0$	$v' = 12$	$v' = 13$	$v' = 14$
Resonance Prediction (GHz)	288722	306491	307876	309252

using signal directly from the atom. Due to the large detuning, the scattering rate from the PA beams is too low to be used for alignment. However, when the PA beam is set to circular polarization, it creates an effective magnetic field parallel to the beam propagation direction of the form [106],

$$B_{\mathrm{eff}} = -U_0 \frac{\partial_2 - \partial_1}{\partial_2 + 2\partial_1} \mathbf{C}$$

where U_0 is the scalar light shift, ∂_1 and ∂_2 are the detuning from the D_1 and D_2 line respectively, ε is the polarization vector and

$$\mathbf{C} \equiv \mathrm{Im}(\varepsilon \times \varepsilon^*) \tag{5.2}$$

qualifies the ellipticity of the polarization with $|C| = 1$ for pure circular polarization and $|C| = 0$ for linear polarization. This effective magnetic field causes a relative shift between the $|4, 4\rangle$ and the $|3, 3\rangle$ states which can be measured using a Raman transition (Fig. 5.4A). By measuring the shift as a function of the beam position, we can determine the size and the center of the PA beam and align the beam to the atom (Fig. 5.4B).

5.3.2   Experiment Sequence and Resonance Frequencies

For the PA spectroscopy, we mainly focus on states with large binding energies which are

expected to be good candidates as the intermediate state for Raman transfer (section 7.2).

In particular, we scanned the PA light frequency around the $v' = 0$ and $v' = 12 - 14$

vibrational states in the $c^3\Sigma_{\Omega=1}$ potential. Table 5.1 shows the predicted resonance frequencies for the PA resonance from $|\mathrm{Na}(2,2), \mathrm{Cs}(4,4)\rangle$ based on fitting to previous measurements [135]. The frequencies are calculated from a Dunham expansion [137] that is corrected for the hyperfine structure for the atoms.

In order to observe PA, we first prepare both the Na and Cs atoms in the motional ground states in the same tweezer [138]. We then turn on the PA beam for a set time followed by separating the atoms into their respective tweezers and imaging the atoms. When we hit a PA resonance, the excited molecular state will typically decay down to either a molecular ground state, which will remain in at most one of the tweezers after the separation, or an atomic state with high relative motional energy and escape the trap. In either case, this leads to at least one empty tweezer after the separation. By measuring the probability of having both the Na and Cs atoms after the PA pulse conditioned on both atoms being initially loaded, we can capture the probability of PA event and locate the resonances.

The initial atomic state we used is $|\mathrm{Na}(2,2), \mathrm{Cs}(4,4)\rangle$ which has $L = 0$ and $S = 1$. For atoms in the motional ground state we also have $N = 0$ and therefore $J = 1$ which should be coupled to $J = 0, 1, 2$ excited states base on the $\Delta J = 0, \pm 1$ selection rule. However, since the cooling is not perfect, we expect some atoms to be initially in the $N = 1$ state which can allow a weaker transition to the $J = 3$ states. Moreover, since the PA beam polarization is circular and has maximum overlap with the σ^+ polarization, the $J = 2$ excited
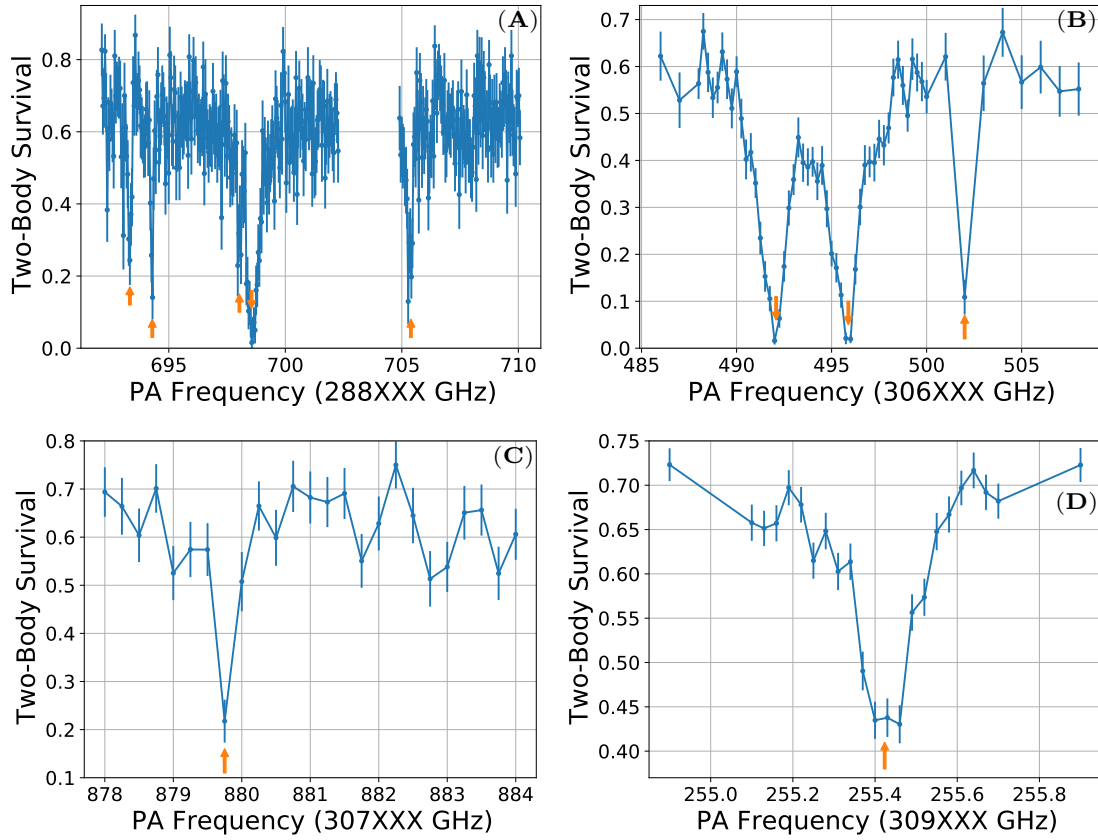
Figure 5.5: PA spectrum for (A) $v' = 0$, (B) $v' = 12$, (C) $v' = 13$, (D) $v' = 14$. The PA frequency is shown in GHz with an offset. Multiple rotational states can be observed for $v' = 0$ and $v' = 12$. $v' = 0$ also shows multiple peaks that correspond to the hyperfine structure of the molecule. The $v' = 13$ and $v' = 14$ transitions are relatively weak and as a result only the strongest line in each transition is measured.

state is expected to have the strongest coupling.

Fig. 5.5 shows the PA spectra measured for different vibrational states with the frequencies summarized in table 5.2. The spectra for $v' = 0$ and $v' = 12$ shows three rotational states whereas only the strongest rotational state is measured for $v' = 13$ and $v' = 14$. The $v' = 0$ spectrum also shows the hyperfine structure for the lowest two rotational states.

The rotational states of the molecule can be determined from the energy gap between

Table 5.2: PA resonance frequencies for $v' = 0, 12 - 14$. The J numbers for $v' = 0$ and $v' = 12$ are assigned based on the rotational state spacing. For $v' = 13$ and $v' = 14$, we assume the observed line is $J = 2$ which is expected to have the strongest coupling. More the one lines have been observed for certain rotational and vibrational state due to the hyperfine structure.

Vibrational State		$v' = 0$	$v' = 12$	$v' = 13$	$v' = 14$
Resonance (GHz)	$J = 1$	288693.3	306492.1	-	-
		288694.3	-	-	-
	$J = 2$	288698.0	306495.9	307879.8	309255.4
		288698.5	-	-	-
	$J = 3$	288705.4	306502.0	-	-

the states based on the discussion in section 5.2.1.1. The ratio of the spacing between the lowest J states we measured are 1.64 and 1.61 for $v' = 0$ ‡ and $v' = 12$ respectively. This is very closed to the ratio of $3/2$ for $\Omega = 1$ states. The main source of the deviation is likely the hyperfine structure that was ignored in the discussion above.

5.3.3 Linewidth

In addition to the energy, another property of the excited state that is important for driving a two-photon transition using the state is the linewidth. This determines the scattering or decoherence rate of the two-photon transition which then determines the transfer efficiency (chapter 7). The linewidth, or decay rate, due to electric dipole transitions is [132, p. 197],

$$\Gamma = \sum_i \frac{\omega_i^3 d_i^2 \text{FCF}_i}{3\pi\varepsilon_0 \hbar c^3}$$

---

‡The energy of the strongest hyperfine line is used

where ω_i is the decay frequency, d_i is the transition dipole moment, and the sum is over all the decay channels. Since the size of the excited-state electronic wavefunction is similar to that of an unbound excited atomic state pair, the molecule has a similar transition dipole moment as the corresponding atomic transition $d_i \approx d_{Cs}$. Moreover, since $\sum_i FCF_i = 1$ and $\omega_i \approx \omega_{Cs}$ we have

$$\Gamma \approx \frac{\omega_{Cs}^3 d_{Cs}^2}{3\pi\varepsilon_0 \hbar c^3}$$

$$= \Gamma_{Cs} \approx 2\pi \times 5 \text{ MHz}$$

Since the PA laser is locked using a wavemeter with a precision ≈ 20 MHz, we expect the PA linewidth we measured to be limited by our frequency resolution.

This is, however, not what is observed in the experiment. Fig. 5.6A shows the narrowest spectrum of the $v' = 12, J = 2$ PA line we measured when the tweezer frequency is set to 306344.5 GHz with 10 mW of power. The linewidth is determined to be $167(32)$ MHz which is much greater than the theory prediction. Furthermore, the observed linewidth appears to be dependent on the tweezer power. The same PA line measured with 1 mW tweezer power is shown in Fig. 5.6B with a significantly narrower linewidth of $27.3(97)$ MHz. In fact, the linewidth appears to be proportional to the tweezer power as shown in Fig. 5.6C, which suggests that the linewidth may be broadened by a two-photon process.
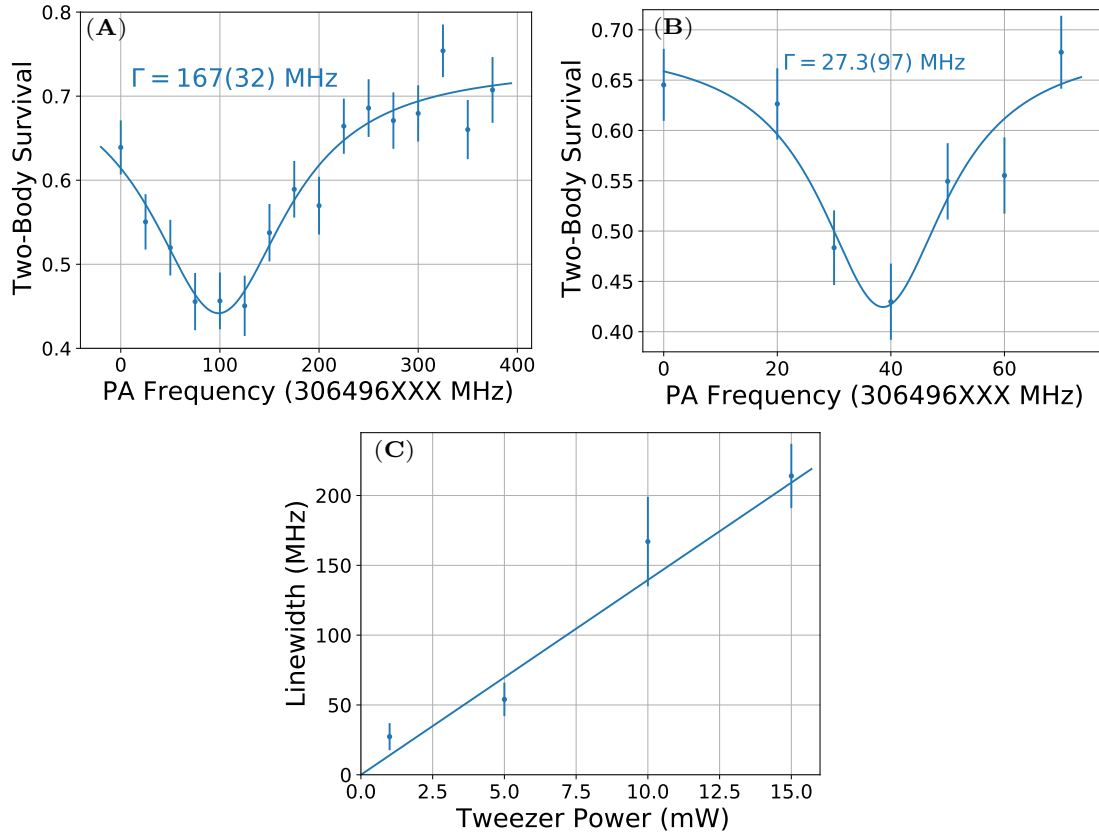
Figure 5.6: Fitting of PA linewidth for (A) 10 mW, (B) 1 mW tweezer power, showing a broad linewidth and a significant difference between the two. (C) Fitting of the PA linewidth as a function of tweezer power suggests a proportional relation between the two.
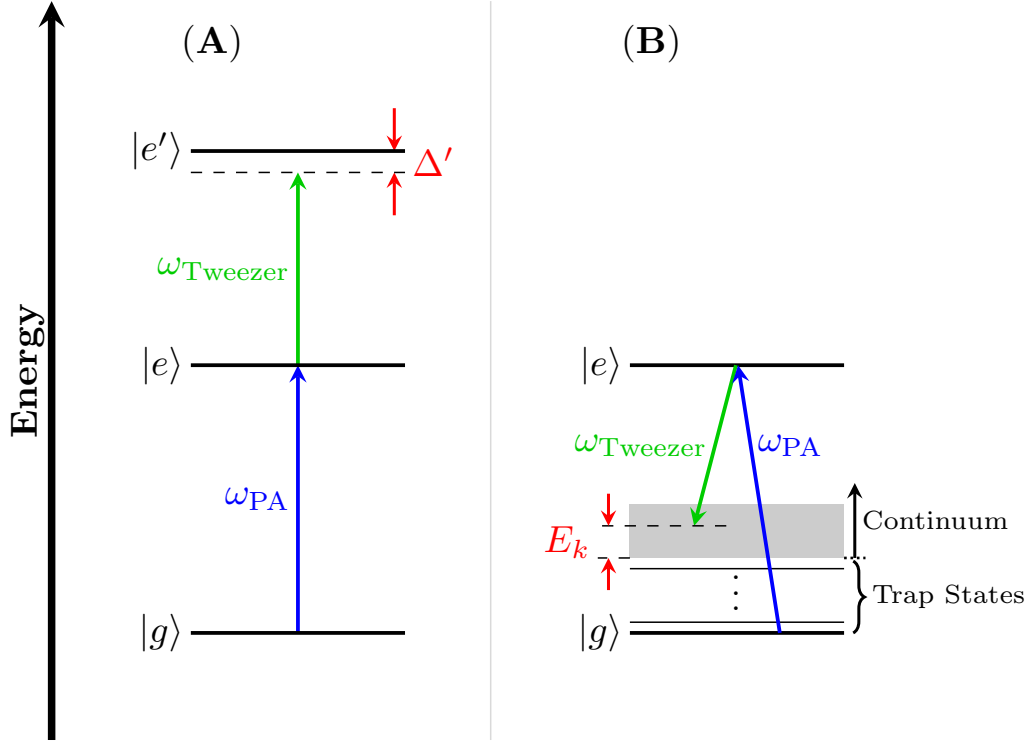
Figure 5.7: Potential two-photon broadening mechanism for PA by coupling the excited state $|e\rangle$ via the tweezer to (A) a higher excited state $|e'\rangle$ or (B) the atomic motional continuum. (A) For coupling to a higher excited state, the broadening depends on the two-photon detuning Δ' from $|e'\rangle$. (B) For coupling to the atomic motional continuum, the broadening is a function of the kinetic energy E_k of the atomic state.

We initially suspected that the source of this broadening is due to the tweezer light coupling the excited molecular state to another state at a higher energy (Fig. 5.7A). If this is the case, we would expect the broadening to be a function of the sum of the tweezer and PA light frequency depending on the detuning from the nearest two-photon excited state. However, the broadening does not change significantly when the tweezer frequency is changed by ≈ 10 GHz and is also observed for other excited states including $v' = 0$ and $v' = 14$ which have very different resonance frequencies. It is therefore unlikely that this is the broadening mechanism we observe. Instead, we believe the effect is caused by a Λ type two-photon process coupling the excited state to the atomic ground states. This mechanism was suggested to us by Olivier Dulieu. In the following section, I will provide an estimation for such a broadening process.

5.3.3.1 Two-Photon Coupling to the Atomic Motional Continuum

The broadening of the PA line requires the coupling of the excited state to a continuum of states. For the ground atomic state, since the state is stable with respect to radiative decay, this continuum cannot be the photon continuum. Instead, the excited state is coupled to the relative motional continuum of the atoms. Physically, this corresponds to a photodissociation process whereby the atoms fly away with high kinetic energies corresponding to the detuning of the tweezer (Fig. 5.7B).
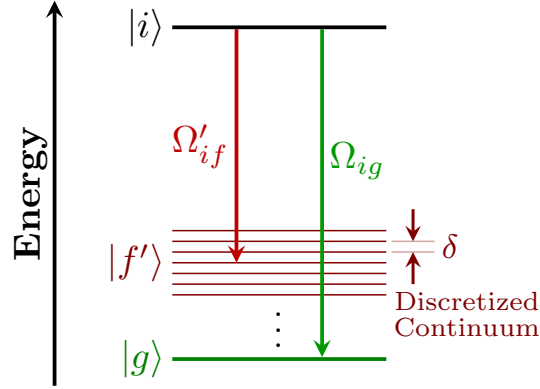
Figure 5.8: Calculation of decay rate to the motional excitation from the ground motional state $|g\rangle$. The continuum is discretized to $|f'\rangle$ with state spacing δ. This section focuses on the case where the initial state $|i\rangle$ is the electronic excited state $|e\rangle$ in Fig. 5.7B. However, the discussion can be generalized to other initial states with different coupling to the motional continuum.

The photodissociation rate is determined by Fermi's golden rule,

$$\Gamma = 2\pi \Omega_{if}^2 \rho_f$$

where Ω_{if} is the matrix element between the initial state $|i\rangle = |e\rangle$ and the final continuum state, ρ_f is the density of states near the final state. We calculate this by first discretizing the continuum (Fig. 5.8) and the rate becomes

$$\Gamma = 2\pi \frac{\Omega_{if}'^2}{\delta}$$

where Ω_{if}' is the Rabi frequency between the initial and final state and δ is the spacing between the discretized final states.

The Rabi frequency Ω'_{if} is proportional to the square root of FCF, which we can calculate for the atomic ground motional states by exact diagonalization of the atomic wavefunction. However, due to the high energy (> 10 GHz) of the final state, calculating FCF for the target state using this method requires an unrealistic number of states to be included. Instead, we approximate it using the results for the atomic ground state by assuming the FCF to be proportional to the probability density of the non-interacting atomic wavefunction at zero relative distance so that,

$$\Omega'_{if} = \Omega_{ig} \frac{\psi_f(r_{rel} = 0)}{\psi_g(r_{rel} = 0)}$$

where Ω_{ig} is the Rabi frequency between the initial state and the atomic motional ground state and ψ_f and ψ_g are the wavefunctions of the final and ground motional atomic state without the molecular potential. This approximation is justified because,

1. The molecular potential is short ranged and the excited molecular state is small.

2. Only the final atomic wavefunction within the molecular potential contributes to the FCF. For relatively low motional energy this wavefunction is proportional to the value of the wavefunction at the edge of the molecular potential which is well approximated by the atomic wavefunction without the molecular potential.

This approximation remains valid until the de Broglie wavelength for the atomic state is comparable to the size of the molecular potential which corresponds to a motional energy of ≈ 40 GHz and even then the result can still be used as an order of magnitude estimation

for higher motional energies.

For atomic motional ground state, we have,

$$\psi_g(r_{rel} = 0) = \prod_{i=1}^{3} \left(\frac{\mu\omega_i}{\pi}\right)^{1/4}$$

$$= \left(\frac{\mu^3 \omega_1 \omega_2 \omega_3}{\pi^3}\right)^{1/4}$$

where μ is the reduced mass $\mu \equiv m_{Na} m_{Cs}/(m_{Na} + m_{Cs})$, and ω_i's are the trapping frequencies for the relative motion along the three trap axes. We discretize the continuum state by adding an infinitely deep spherical potential well of radius R around the center. The radial wavefunctions of the eigenstates within the well with quantum number $n = 1, 2, \ldots$ is,

$$\psi_n = \frac{1}{\sqrt{4\pi r_{rel}}} \sqrt{\frac{2}{R}} \sin\left(\frac{\pi n r_{rel}}{R}\right)$$

and the corresponding energy,

$$E_n = \frac{\pi^2 n^2}{2\mu R^2}$$

The energy gap between neighboring states is

$$\delta_n \approx \frac{\pi^2 n}{\mu R^2}$$

and the wavefunction value at $r_{rel} = 0$ is,

$$\psi_n(r_{rel} = 0) = \sqrt{\frac{1}{2\pi R}} \frac{\mathrm{d}}{\mathrm{d}r_{rel}} \sin\left(\frac{\pi n r_{rel}}{R}\right)\Bigg|_{r_{rel}=0}$$

$$= \frac{\pi n}{\sqrt{2\pi R}R}$$

Substituting into Γ and taking the limit of $R \to \infty$ we have

$$\Gamma = 2\pi \frac{\Omega_{ig}^2}{\eth} \frac{\psi_f^2(r_{rel} = 0)}{\psi_g^2(r_{rel} = 0)}$$

$$= 2\pi\Omega_{ig}^2 \frac{\mu R^2}{\pi^2 n} \frac{\pi^2 n^2}{2\pi R^3} \sqrt{\frac{\pi^3}{\mu^3 \omega_1 \omega_2 \omega_3}}$$

$$= \Omega_{ig}^2 \frac{n}{R} \sqrt{\frac{\pi^3}{\mu \omega_1 \omega_2 \omega_3}}$$

$$= \Omega_{ig}^2 \sqrt{\frac{2\pi E}{\omega_1 \omega_2 \omega_3}} \tag{5.3}$$

For the condition in Fig. 5.6A we have $\Omega_{ig} \approx 2\pi \times 1\,\mathrm{MHz}^\ddagger$, $E = 2\pi \times 151\,\mathrm{GHz}$ and $\omega_{1,2,3} = 2\pi \times \{20, 100, 100\}\,\mathrm{kHz}$ which predicts a broadened linewidth of $\Gamma = 2\pi \times 70\,\mathrm{GHz}$. This prediction is only an estimate due to the breakdown of the approximation for the coupling strength we used and is in fact much broader than the observed value. Nevertheless, it confirms that this broadening mechanism can indeed cause a significant broadening comparable to the observed linewidth.
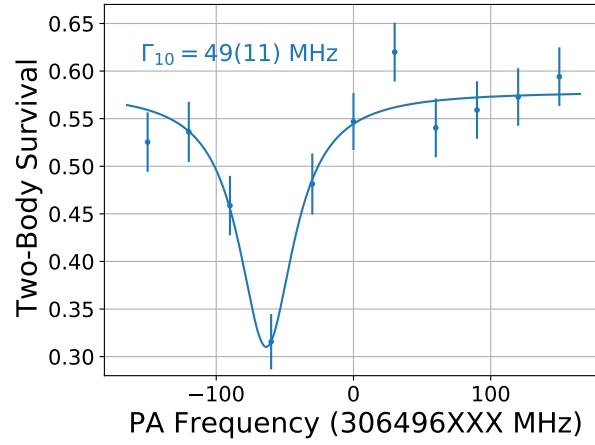
Figure 5.9: Fitting of PA linewidth for 10 mW tweezer power at 306612 GHz. The linewidth is significantly narrower than the value measured when the tweezer is red detuned from the PA resonance (Fig. 5.6).

5.3.3.2 ELIMINATING THE BROADENING WITH BLUE DETUNED TWEEZER

Another prediction from the theory is that if the tweezer light is blue detuned from the

PA line, the two-photon process will not couple to the motional continuum anymore

and there should be no broadening of the line[‡]. We can confirm this by measuring the

linewidth of the same PA line with the tweezer frequency set to 306612 GHz, which is

121 GHz blue detuned from the PA resonance. The result shown in Fig. 5.9 confirms that

the linewidth is indeed narrower for this tweezer frequency.

[‡]Note that the tweezer is still red detuned from the atomic state which provides most of the trapping potential
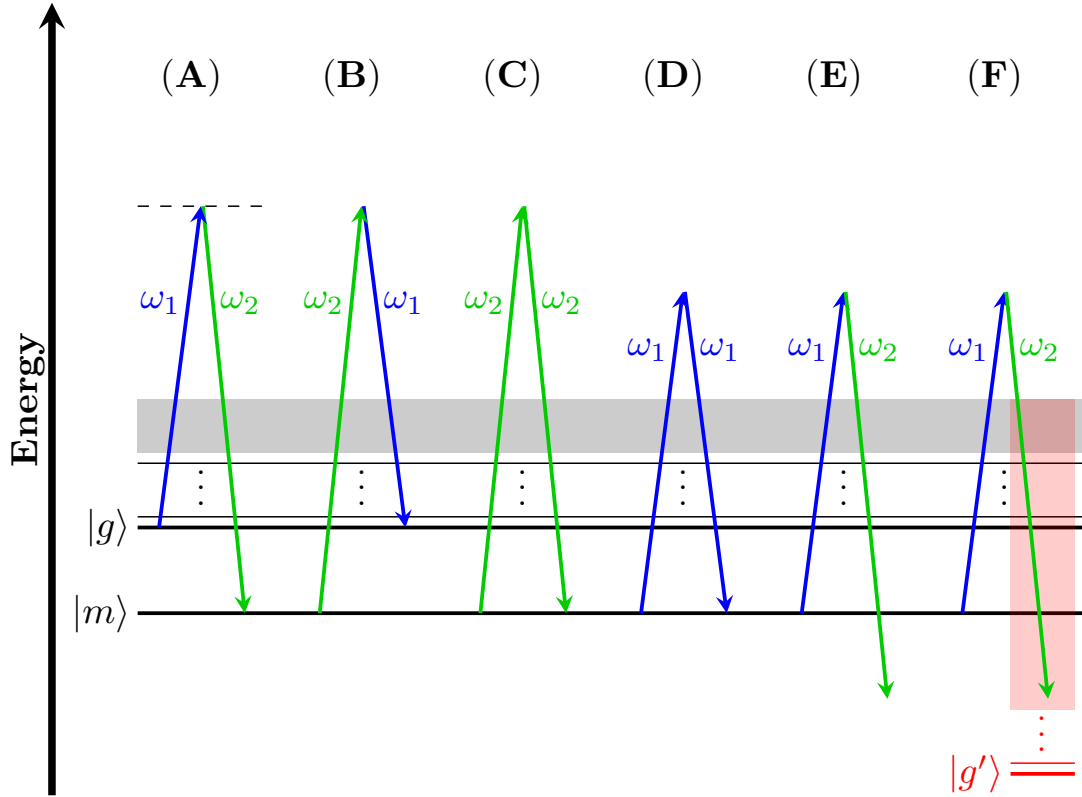
Figure 5.10: Effect of two-photon coupling to atomic continuum on molecular state. (A) Raman transition from the atomic ground state $|g\rangle$ to the molecular bound state $|m\rangle$ using two Raman beams with frequencies ω_1 and ω_2. (B-E) Two photon transitions starting from the molecular state $|m\rangle$ with different frequency combinations without additional atomic spin states. (B) This is the reverse Raman transition and reaches the initial atomic state. (C,D) The frequency pairs couples back to $|m\rangle$. (E) This couples to an energy below $|m\rangle$. Note that none of the two-photon transitions from $|m\rangle$ in (B-E) ends up in the atomic motional continuum and therefore unaffected by the broadening mechanism discussed in this section. (F) The present of another atomic spin state $|g'\rangle$ with lower energy allows the two-photon transition from $|m\rangle$ to be coupled to the motional continuum corresponding to the new spin state. Note that only the frequency combination similar to (E) is shown for simplicity. Coupling channel corresponding to (B-D) also exists which could allow coupling to the same continuum at different motional energies.

5.3.3.3 IMPLICATION ON TWO-PHOTON TRANSITION TO GROUND MOLECULAR STATES

Since the broadening is caused by two-photon coupling to high energy atomic motional states, the observed linewidth in a PA measurement cannot be directly translated to the scattering rate during a two-photon transition that uses a different set of laser frequencies.

In fact, with a single ground atomic spin state, the scattering rate for the final molecular state during a two-photon transition is not affected by this effect. As shown in Fig. 5.10B-E, the molecular state cannot reach the atomic motional continuum via a two-photon transition. The atomic state, on the other hand, can reach the continuum though the loss rate is in general much lower than the molecular state and is usually not the limiting factor for the transfer efficiency.

The molecular state can also couple to a different motional continuum if there are other atomic spin states with lower energies (Fig. 5.10F). Since the stable atomic state has the lowest energy among all the ones with the same total m_F, such a state must have a different total m_F than the initial state. Therefore, such coupling is forbidden if the two Raman beams both have π polarization, as is the case for the Raman transition in chapter 6 and 7, and will not cause any loss due to this mechanism. Polarization impurity, however, can allow such coupling and enable this loss process.

5.4 Summary and Outlook

We continued our study of the interaction between two atoms in the optical tweezer. We characterized the excited molecular potential by measuring the energy of bound states using photoassociation spectroscopy and identified the states based on their rotational structure. On the other hand, the high intensity of the optical tweezer also creates unique challenges that can lead to dissociation or loss of the atoms or molecules. We studied one of the effects and confirmed our model for the loss process with additional measurements and discussed its implication for future experiments. The identification of the excited molecular state opens up the pathway to the formation of a single ground-state molecule via two-photon process and will be the focus of later chapters.

6

Two-photon Spectroscopy of NaCs

Ground State

6.1 Introduction

The excited molecular states measured and characterized in chapter 5 provide us a pathway

to couple to the ground electronic molecular states using two-photon transitions. While it

is in principle possible to drive from the atomic state to any desired molecular ground state for various applications, doing so directly has many technical challenges due to the wave-function size mismatch. We have observed such an effect in section 5.3.1 where it causes a very small FCF between the excited molecular states and the ground atomic state requiring a high PA intensity to improve the signal strength. Because of this, we follow the approach of using a two-step process to form rovibronic ground-state molecules, as discussed in section 0.2.1. The first step transfer to a weakly bound molecular state makes it easier to maintain laser coherence during the slow transition starting from the atomic state.

In this chapter, we will discuss the use of Raman spectroscopy to measure the properties of the weakly bound molecular ground states needed for driving a coherent transition to form the molecule. In section 6.2 we will describe the states involved and the setup for the Raman spectroscopy as well as the measured binding energy for the $N = 0$ states. In section 6.3 we study the coupling between angular momenta for near threshold molecular states by characterizing the $N = 2$ states.

6.2 Weakly Bound NaCs Ground States

As mentioned in section 5.2.1.2, the angular momentum coupling for weakly bound molecular states is similar to that of the atoms. Therefore, instead of using the term symbol for the Hund's case (a) to identify the molecular potential and bound states, we use the hy-
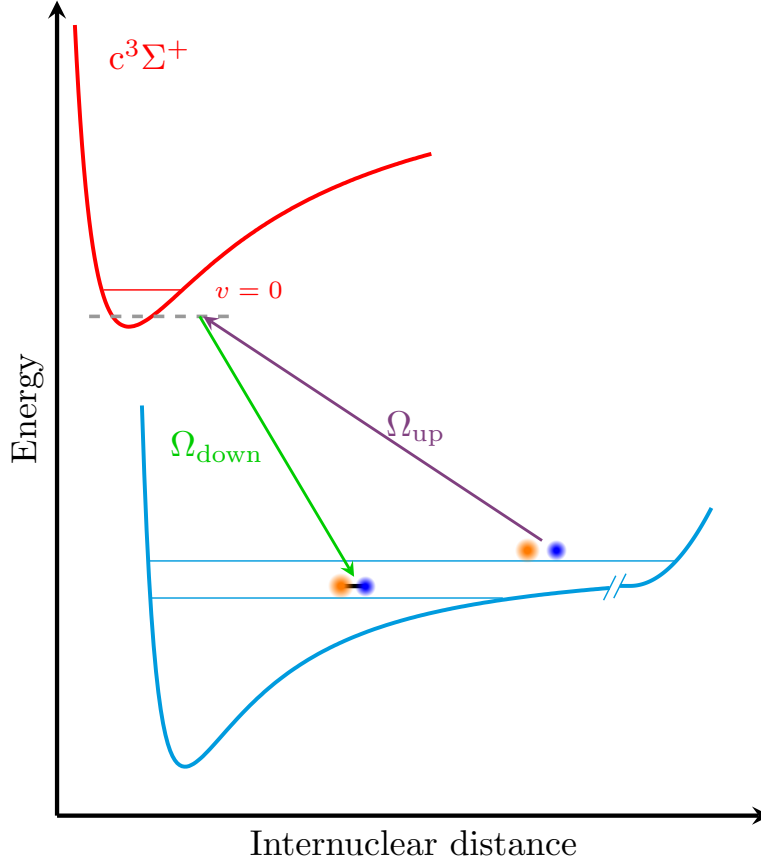
Figure 6.1: States and beams in the Raman transition. From the initial atomic motional ground state, we drive a Raman transition to a weakly bound molecular ground state by detuning from the $c^3\Sigma(v' = 0)$ state.

perfine state $(F_{\mathrm{Na}}, F_{\mathrm{Cs}})$ for the atoms instead. Similarly, since the vibrational states of the molecule do not always correspond to a particular short range potential, we also label the vibrational states from the atomic state threshold. Under this system, the atomic motional ground state is $v'' = 0$ and the first (lowest binding energy) molecular bound state is $v'' = -1$.

In order to measure the binding energy of a molecular state, we first prepare the atom

in the corresponding hyperfine state and drive a Raman transition to the molecular state. We use a Raman transition that is detuned from the $c^3\Sigma(v'=0)$ state measured in section 5.3 (Fig. 6.1). When the Na and Cs are in the same tweezer, they can undergo fast spin-exchange collisions that change the hyperfine state of the atoms. This process can cause the hyperfine energy (>1 GHz) of the atoms to be transferred to the motional energy and eject the atoms from the tweezer (<100 MHz deep). As a result, the measurement can only be done when the spin-exchange collision is suppressed, which includes the following spin combinations,

1. $F_{\mathrm{Na}}=1$ and $F_{\mathrm{Cs}}=3$

    This is the spin state with the lowest energy and therefore the spin-exchange interaction is energetically forbidden. In the experiment, we use the state $|\mathrm{Na}(1,1),\mathrm{Cs}(3,3)\rangle$ which can be prepared from the $|\mathrm{Na}(2,2),\mathrm{Cs}(4,4)\rangle$ state from OP easily by driving a Raman transition for both the Na and Cs atoms. This state also remains the lowest energy atomic state in the presence of a weak magnetic field.

2. $|\mathrm{Na}(2,2),\mathrm{Cs}(4,4)\rangle$ and $|\mathrm{Na}(2,2),\mathrm{Cs}(3,3)\rangle$[‡]

    These spin states are stable because the spin-exchange collision conserves the total m_F of the two atoms and the two states are the lowest energy states that have the same total m_F. An inelastic collision that changes the total m_F happens at a lower rate since it requires transferring angular momentum between the spin and motion of the atom.

[‡]States with opposite m_F, i.e. $|\mathrm{Na}(2,-2),\mathrm{Cs}(4,-4)\rangle$ and $|\mathrm{Na}(2,-2),\mathrm{Cs}(3,-3)\rangle$ are also stable but are omitted here since these cannot be easily prepared in our experiment.
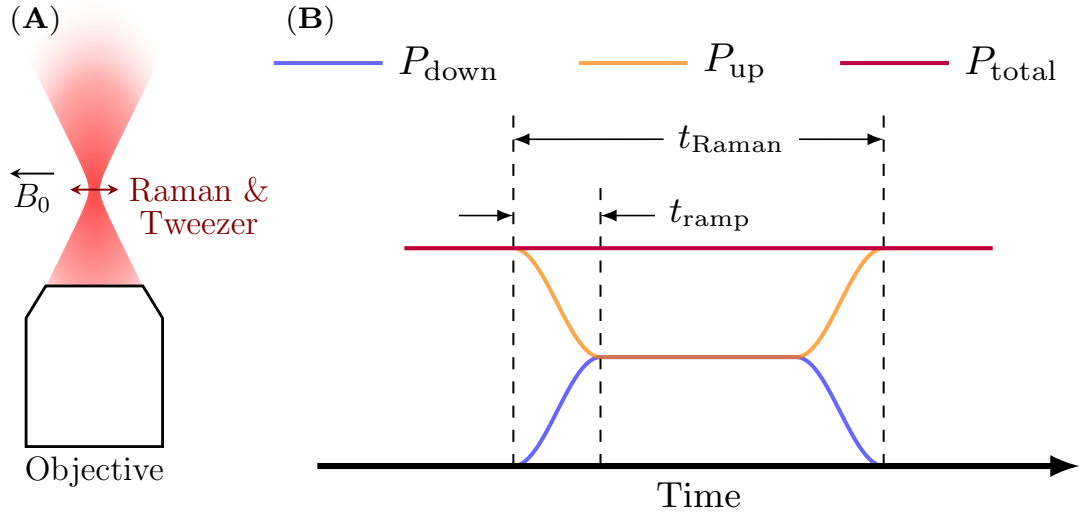
Figure 6.2: (A) Geometry and polarization of trap and Raman beam relative to the bias magnetic field. We use a bias B field of $B_0 = 8.8 \, \text{G}$ alone the tweezer polarization to define the quantization axis which is the same as the one used for Raman sideband cooling in Fig. 3.2. As a result, the atoms experience predominantly π polarization from the tweezer. (B) Raman transition pulse sequence. The tweezer initially consists of only up leg power. When driving the Raman transition, the up leg power is smoothly ramped down and the down leg power ramped up over $t_{\text{ramp}} = 10 \, \mu\text{s}$ while maintaining the total power of the tweezer. This minimizes the heating on the atoms due to power fluctuation while maximizing the time with maximum Raman Rabi frequency when the up and down leg powers are equal.
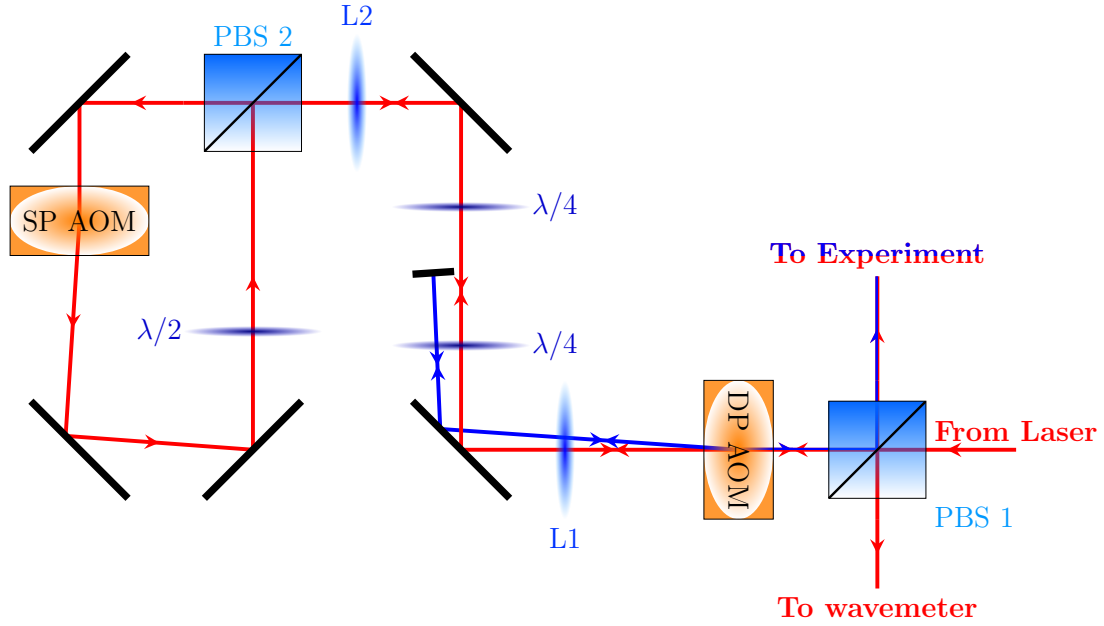
Figure 6.3: Beam path for generating the frequency for Raman transition in the tweezer. (Beam path for fiber coupling and overall power control is not shown.) The red beam path is the 0-th order of the double pass (DP) AOM which is used for the tweezer. When the DP AOM is turned on, some power is redirected to the first order (blue beam path) which generates the required frequency difference to drive the Raman transition. The two frequencies are recombined on the DP AOM. The 0-th order light is shifted by another single pass (SP) AOM running on a different frequency before recombining. Without this AOM, the leak light from the DP AOM will be at the same frequency as the 0-th order light which can cause a significant power fluctuation due to interference. The SP AOM ensures that none of the leaking light frequencies coincide with either intended frequencies therefore avoiding this issue. Different selection of the SP and DP AOM as well as their orders can be used to cover a wide range of two photons detuning for Raman transition. The experiment typically starts with the SP AOM on and the DP AOM off. When driving the Raman transition, the powers on both AOMs are ramped simultaneously to achieve the desired power at both frequencies.

6.2.1   Driving Raman Transition using the Optical Tweezer

In order to increase the intensity of the Raman beams to overcome the small FCF, we use the tweezer beam to drive the Raman transition (Fig. 6.2A), which maximizes the intensity due to the small focal size of the tweezer. In addition, since the atoms are trapped at the maximum of the tweezer beam, this also ensures that the Raman beam is aligned automatically to the atoms and suppresses sensitivity to mechanical fluctuation that is usually associated with a small beam size. Moreover, this also minimizes the number of beams the atoms experience during the Raman transition which, in turns, minimizes the scattering. As a result, the coherence of the transition is also improved which is important for achieving coherent creation of molecules (chapter 7).

The beam path to generate the required frequencies in the tweezer is shown in Fig. 6.3. Due to back reflection of the acoustic wave and imperfect order separation from the AOM, each beam may contain small frequency sidebands that are shifted from the desired one by integer multiple of the AOM driving frequency. Since we are combining two beams into one, such light in one beam that coincides with the frequency of the other beam can cause large power fluctuation due to interference. We added a single pass AOM in the beam path to shift the frequency of the red beam away from all possible frequencies in the blue beam to avoid this issue. The additional AOM also increases the frequency tuning range compared to using only one double pass AOM. The powers in each beam are calibrated as a
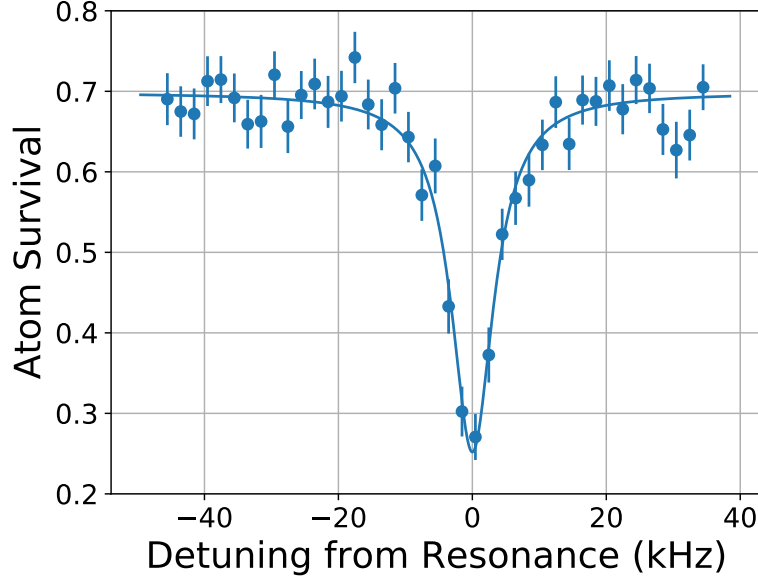
Figure 6.4: Raman resonance for $v'' = -1$, $N = 0$ state from $|\text{Na}(2,2), \text{Cs}(4,4)\rangle$.

function of AOM powers so that we can select the desired power ratio during the experiment. When driving the Raman transition, instead of turning on a separate beam, we ramp down the power of the original tweezer and ramp up the power in the second frequency while maintaining the total power to minimize heating of the atoms (Fig. 6.2B).

6.2.2 Raman Resonance on $N = 0$ Ground State

We first measure the binding energy for the $v'' = -1$, $N = 0$ state from the atomic states $|\text{Na}(2,2), \text{Cs}(4,4)\rangle$, $|\text{Na}(1,1), \text{Cs}(3,3)\rangle$, and $|\text{Na}(2,2), \text{Cs}(3,3)\rangle$. The theory prediction of the binding energies are shown in table 6.1. Fig. 6.4 shows the measured Raman resonance from $|\text{Na}(2,2), \text{Cs}(4,4)\rangle$ using 10 mW of tweezer power at a detuning of

Table 6.1: Binding energies and Zeeman shift for $v'' = -1$, $N = 0$ states. The theory prediction for $|\text{Na}(2,2), \text{Cs}(4,4)\rangle$ was calculated from the potential in [129]. The prediction for the other two spin states are calculated by Jeremy Hutson using a coupled-channel model calibrated based on the measured binding energy for $|\text{Na}(2,2), \text{Cs}(4,4)\rangle$ and the scattering length measured from section 4.3.2 and Ref. [119]. The experimentally measured resonances have a AC Stark shift in the range of 10 kHz to 10 MHz that depends on the tweezer power and frequency. We obtain the bare resonant frequency by measuring the resonance at different tweezer powers and extrapolate to zero trap power. An example of such analysis is given in section 7.5.2.

Spin state	Resonance (MHz)			Zeeman shift (kHz/G)
	Theory	8.8 G	0 G	
$|\text{Na}(2,2), \text{Cs}(4,4)\rangle$	284	297.8472(28)	297.8510(28)	$-0.43(10)$
$|\text{Na}(1,1), \text{Cs}(3,3)\rangle$	369	367.7892(25)	369.63(29)	$-209(33)$
$|\text{Na}(2,2), \text{Cs}(3,3)\rangle$	771	770.200516(24)	769.8294(22)	42.17(24)

-100 GHz from the $v' = 0$ excited state and a 2 ms pulse time.

The tweezer also shifts the resonance frequency due to AC Stark shift. We remove this effect by measuring the resonance at different tweezer powers and extrapolate to zero trap power. Similarly, we measure the Zeeman shift and the resonance frequency at zero magnetic field. The summary of the results are also shown in table 6.1. The result shows good agreement with theory prediction, especially for the $|\text{Na}(1,1), \text{Cs}(3,3)\rangle$, and $|\text{Na}(2,2), \text{Cs}(3,3)\rangle$ spin states for which the theory has been calibrated using previous results from our experiment.

Note that the Zeeman shift for the $|\text{Na}(2,2), \text{Cs}(4,4)\rangle$ state is significantly smaller than that for other spin states. The reason for this is spin mixing due to magnetic coupling between states with the same total m_F[‡]. The $|\text{Na}(2,2), \text{Cs}(3,3)\rangle$ spin state is coupled to the $|\text{Na}(2,2), \text{Cs}(4,3)\rangle$, $|\text{Na}(1,1), \text{Cs}(4,4)\rangle$ and $|\text{Na}(2,1), \text{Cs}(4,4)\rangle$ states whereas

---

[‡]The same coupling that leads to spin exchange collision.
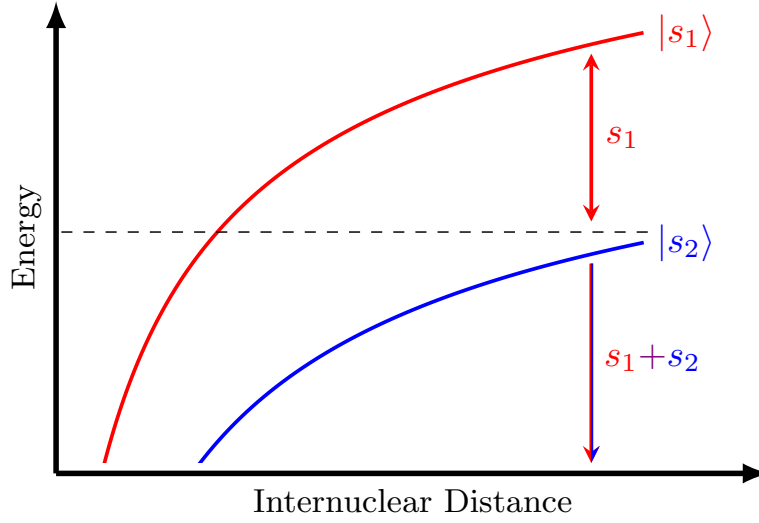
Figure 6.5: Spin state mixing near the atomic threshold. Energy above the s_2 threshold only supports one molecular spin state so the bound state within the s_1 potential in this region is almost purely s_1. Energy below the s_2 threshold supports both s_1 and s_2 molecular states so bound states in this region may have a mixture of s_1 and s_2 if the two spin states are coupled. This includes all the s_2 bound states and some of the s_1 bound states.

$|\text{Na}(1,1),\text{Cs}(3,3)\rangle$ is coupled to the $|\text{Na}(2,0),\text{Cs}(4,4)\rangle$, $|\text{Na}(1,0),\text{Cs}(4,4)\rangle$, $|\text{Na}(2,1),\text{Cs}(3,3)\rangle$, $|\text{Na}(1,1),\text{Cs}(4,3)\rangle$, $|\text{Na}(2,1),\text{Cs}(4,3)\rangle$, $|\text{Na}(2,2),\text{Cs}(3,2)\rangle$ and $|\text{Na}(2,2),\text{Cs}(4,2)\rangle$ states. All of these states listed above has higher energy so their bound states may cause spin mixing with the $|\text{Na}(2,2),\text{Cs}(3,3)\rangle$ and $|\text{Na}(1,1),\text{Cs}(3,3)\rangle$ bound states (Fig. 6.5) causing them to have a different magnetic field dependence from the corresponding atomic state resulting in a non-zero differential Zeeman shift. On the other hand, the $|\text{Na}(2,2),\text{Cs}(4,4)\rangle$ bound state is above all the other spin states and therefore has a mostly pure spin state and the transition has little Zeeman shift.

6.3 Rotational Excited NaCs Ground State

In addition to the $N = 0$ state, we also measure the energies of rotational excited states, which verifies the rotational state for our previous results. The precision of the Raman spectroscopy also allows us to study the rich interaction between the nuclear rotation and atomic spin.

Due to parity conservation in the Raman transition, the final molecular state must have an even N so the lowest rotational excited state we can address is $N = 2$. We use $|\mathrm{Na}(2, 2), \mathrm{Cs}(4, 4)\rangle$ as the initial state since, as we saw in the previous section, the corresponding molecular bound state has the least mixing with other molecular potentials. Similarly, we select $F_{\mathrm{atom}} = 6$ as the final total atomic spin state since this is the state we address in the corresponding $N = 0$ spectroscopy and it includes the $m_{F_{\mathrm{atom}}} = 6$ state which has minimum Zeeman shift as discussed in the previous section.

6.3.1 Angular Momentum Coupling in $N = 2$ Ground State

Since the full Hamiltonian is rotationally symmetric for rotation around the field direction, $m_F \equiv m_{F_{\mathrm{atom}}} + m_N = 6$ is conserved in the Raman transition, which includes a total of three states. However, the exact states we are coupling to and the good quantum numbers depends on the strength of the external fields.

At zero or very low external field, the good quantum numbers are F and m_F due to cou-
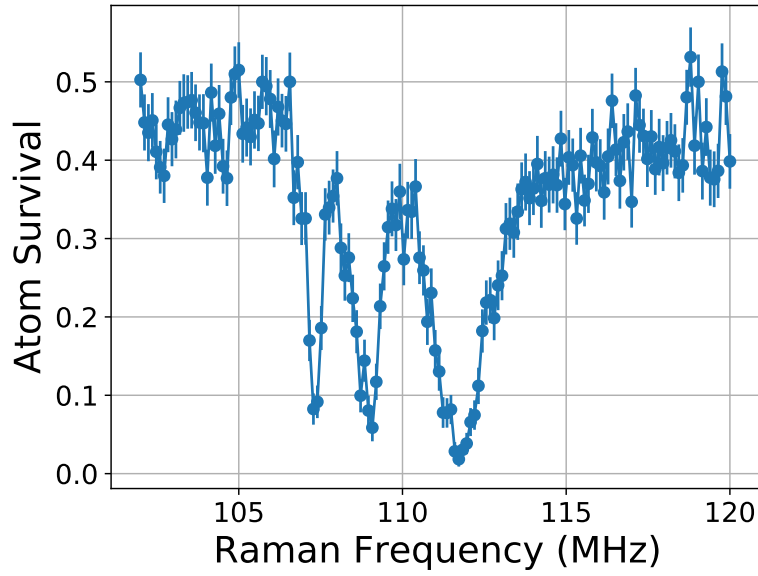
Figure 6.6: $N = 2$ Raman spectrum with 8.8 G of magnetic field and 10 mW of tweezer power. The three resonances correspond to the three $m_F = 6$ states.

pling between $\mathbf{F}_{\text{atom}}$ and $\mathbf{N}$. as discussed in section 5.2.1.2. In this basis, the three energy eigenstates are $|F = 6, m_F = 6\rangle$, $|F = 7, m_F = 6\rangle$ and $|F = 8, m_F = 6\rangle$.

External fields, both magnetic and electric[‡], couples mostly to the atomic spin $\mathbf{F}_{\text{atom}}$[§] rather than the nuclear rotation $\mathbf{N}$. Therefore, at high field $\mathbf{F}_{\text{atom}}$ and $\mathbf{N}$ decouples and their projections become good quantum numbers individually. In this case, the three energy eigenstates are $|m_{F_{\text{atom}}} = 6, m_N = 0\rangle$, $|m_{F_{\text{atom}}} = 5, m_N = 1\rangle$ and $|m_{F_{\text{atom}}} = 4, m_N = 2\rangle$.

[‡]Light field from the tweezer.
[§]More precisely the electron spins within $\mathbf{F}_{\text{atom}}$.
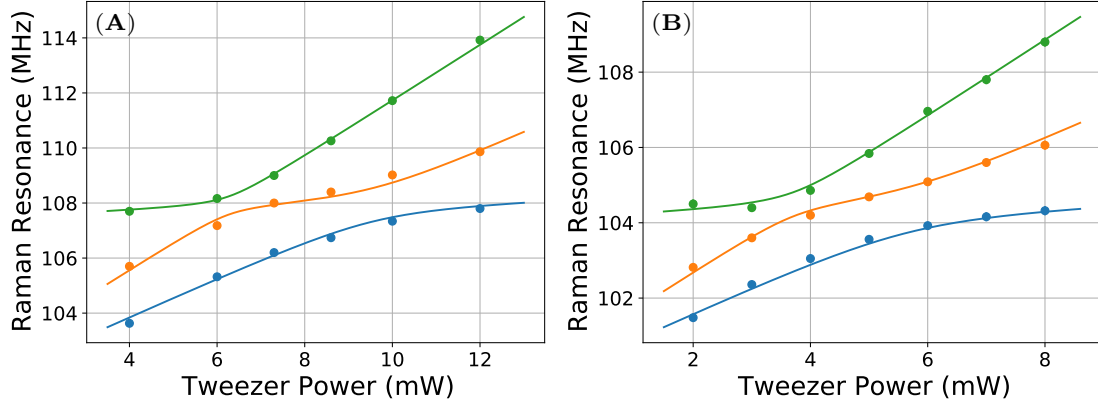
Figure 6.7: Dependence of $N = 2$ Raman resonances on the tweezer power at (A) 8.8 G and (B) 5.28 G magnetic field. The different colors show the resonance frequency for the states with the lowest (blue), second lowest (orange) and highest (green) binding energies. All of the data are taken in the intermediate field regime and therefore in a mixture of different spin states. The lines are fittings of the resonance frequencies using a field dependent Hamiltonian.

6.3.2 $N = 2$ Raman Resonances

Fig. 6.6 shows the Raman spectrum taken at 8.8 G of magnetic field and 10 mW of tweezer power where three resonances can be clearly seen as expected. This single measurement, however, does not allow us to directly identify the states that correspond to each of the resonances. Because of this, we measured the resonance at various tweezer powers and magnetic fields as shown in Fig. 6.7. Each dot in the plot corresponds to an observed resonance frequency.

In order to understand the dependence of the resonances on the external fields we use the following phenomenological model. The Hamiltonian in the $m_F = 6$ subspace we

Table 6.2: Fitted parameters for the $N = 2$ Hamiltonian. Since the ΔE_Fs are not independent, ΔE_8 is not a free parameter and is rather $-\Delta E_6 - \Delta E_7$. Also note that the fit is directly from the binding energy measured in Fig. 6.7 so the zero energy of the Hamiltonian is the atomic $|\mathrm{Na}(2,2),\mathrm{Cs}(4,4)\rangle$ state which also has non-zero Zeeman and AC Stark shifts.

H_0 parameters			
E_0 (MHz)	ΔE_6 (MHz)	ΔE_7 (MHz)	ΔE_8 (MHz)
$-99.196(89)$	$-0.146(87)$	$-0.652(78)$	$0.80(11)$
AC Stark shift parameters			
a_0 (MHz/mW)		a_1 (MHz/mW)	a_2 (MHz/mW)
$1.015(18)$		$0.721(21)$	$6.4(22) \times 10^{-2}$
Zeeman shift parameters			
b_0 (MHz/G)		b_1 (MHz/G)	b_2 (MHz/G)
$-0.237(22)$		$-0.222(22)$	$-0.947(23)$

coupled to can be expressed as,

$$H = H_0 + H_1$$

where H_0 is the zero field term due to the coupling between $\mathbf{F}_{\text{atom}}$ and $\mathbf{N}$, and the H_1 term is due to the coupling to external fields. At zero external field, the eigenstates are the F and m_F basis and the most generic term is,

$$H_0 = E_0 + \sum_{F=6,7,8} \Delta E_F |F, m_F = 6\rangle \langle F, m_F = 6|$$

where E_0 is the "average" energy and ΔE_F are the shift for each F states with $\sum_{F=6,7,8} \Delta E_F = 0$. The term for coupling to the external fields couples to the $m_{F_{\text{atom}}}, m_N$ basis and the generic

expression for such a term is,

$$H_1 = \sum_{i=0,1,2} \left(P_{\text{tweezer}} \cdot a_i + B \cdot b_i \right) |m_{F_{\text{atom}}} = 6 - i, m_N = i \rangle \langle m_{F_{\text{atom}}} = 6 - i, m_N = i|$$

where P_{tweezer} is the tweezer power, B is the magnetic field, and a_i and b_i are the state dependent AC Stark shift and Zeeman shift of the binding energies. We numerically diagonalize this Hamiltonian and fit to the experimental data as shown in the lines in Fig. 6.7. The free parameters of the Hamiltonian we obtained are shown in table 6.2.

6.4 Summary and Outlook

Based on the study of excited molecular states using photoassociation spectroscopy, we study the structure of the ground molecular state using Raman transitions. Compared to the excited states, the stability of the ground-state molecules allows us to resolve single quantum states and control all degrees of freedoms within the molecule. The path to coherent optical formation of ground-state molecules is now fully cleared and this will be the focus of chapter 7.

Coherent Optical Creation of a NaCs

Molecule

7.1 Introduction

The coherent production of a weakly bound ground-state NaCs molecule is an important

milestone in our two-step approach of creating rovibronic ground-state molecules with full

control. Achieving this goal using only an optical transition without a narrow excited-state linewidth can allow more laser-coolable atoms to be associated to molecules coherently. With the characterization of both the excited and ground molecular potentials, we have calibrated all the parameters needed to drive such a transition. Nevertheless, the wavefunction size mismatch between the atomic and molecular states remains a challenge that requires careful selection of the transition pathway.

In this chapter, we will discuss the considerations behind our choice of parameters and show the results of the coherent molecule creation. We begin with section 7.2 to set up a model for a realistic Raman transition beyond the ideal three-level system. Section 7.3 follows a similar track and constructs a model for stimulated Raman adiabatic passage (STIRAP), which is another common way to drive such a two-photon transition, and compares it to the Raman transition. Section 7.4 uses the results from the previous sections to finalize our molecule creation pathway. The result of the molecule creation is given in section 7.5, which also includes a discussion on the transfer efficiency.

7.2 Raman Transition Beyond Three-Level Model

For a Raman transition with Raman Rabi frequency Ω_R and total scattering rate Γ_s, defined as the sum of the scattering rates out of the initial and final states, the time of a π-

pulse is $t_\pi \equiv \pi/\Omega_R$ and the probability of scattering during this time is,

$$
\begin{aligned}
p_s &= \frac{\Gamma_s t_\pi}{2} \\
&= \frac{\pi \Gamma_s}{2\Omega_R}
\end{aligned}
$$

which is proportional to the ratio Γ_s/Ω_R. In an ideal three-level system, this is the only source of decoherence which can be made arbitrarily small by using a large single photon detuning (section 3.2.1.1). However, in a real system, there are often other effects that increase the scattering and may also put a lower limit on the scattering probability during the transfer. Fig. 7.1 shows a generic model for a real Raman transition demonstrating some of these effects. Additionally, other practical limitations in the system such as stabilities of the laser power and frequency also need to be taken into account.

For the experiment, we use a numerical simulation to find the parameter range that gives the best transfer efficiency (section 7.4). Nevertheless, in order to develop a general approach that can be applied to other systems, it is also important to understand the various physical mechanisms that lead to the optimal parameters. Therefore, in this section, we will discuss some of the most important effects on the transfer efficiency at a qualitative and semiquantitative level. Due to experimental constraints, we will assume that the single photon detuning is much smaller than the frequency of each of the individual beams, i.e. $\Delta \ll \nu_1, \nu_2$.
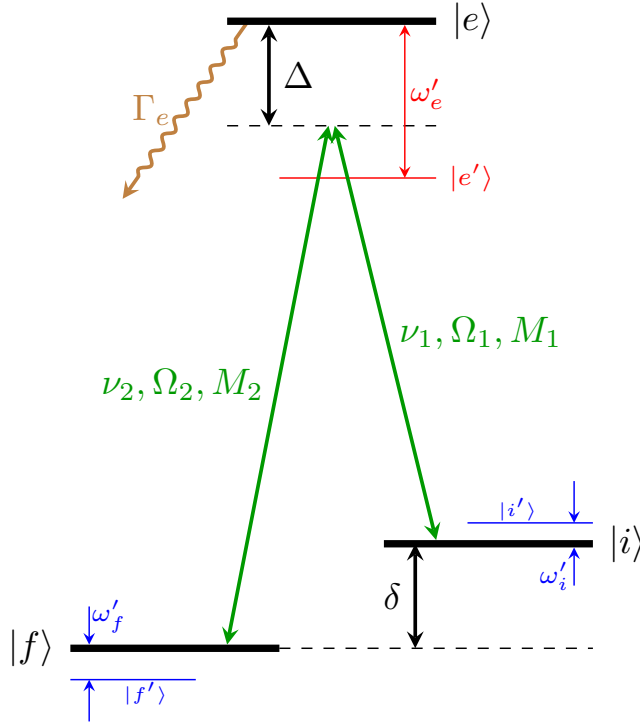
Figure 7.1: Generic model for a real Raman transition. The initial state $|i\rangle$ and the final state $|f\rangle$ has an energy difference δ and is coupled by two Raman beams with frequencies and single photon Rabi frequencies of ν_1, Ω_1 and ν_2, Ω_2 respectively. The corresponding matrix elements (arbitrary unit) are M_1 and M_2. The Raman beams are detuned by Δ from the primary excited state $|e\rangle$, which has a decay rate of Γ_e. We also consider additional states near the initial ($|i'\rangle$), final ($|f'\rangle$) and intermediate excited $|e'\rangle$ states which are separated from the corresponding Raman transition states by ω_i', ω_f' and ω_e' respectively. Only one additional state of each kind is included to simplify the discussion without loss of generality.

7.2.1 ADDITIONAL INITIAL AND FINAL STATES

First, we will discuss the effect of $|i'\rangle$ and $|f'\rangle$ states near the initial and final states. These states can be coupled to the excited state $|e\rangle$ by the Raman beams, which can in turn be coupled to the initial and final states by an off-resonance Raman transition. The leakage is suppressed by the detuning from the Raman resonance, i.e. ω_i' and ω_f'. This puts a limit on the Raman Rabi frequency Ω_R to be smaller than the smallest energy gap, which in turns puts a limit on the minimum Raman transfer time. In our experiment, the minimum energy gap comes from axial motional excitation of the atomic initial states which is between $2\pi \times 10 \sim 30$ kHz depending on the trap depth used. The typical Raman π time we can realize is $0.5 \sim 5$ ms so this effect is not a major limiting factor for our transfer efficiency.

7.2.2 ADDITIONAL EXCITED STATES

Next, we will consider the effect of the $|e'\rangle$ states near the excited intermediate state. These states can be coupled to the ground states, both $|i\rangle$ and $|f\rangle$, by the Raman beams and can cause a change in both the Raman Rabi frequency and the scattering rate. There are two relevant limiting cases that need to be discussed separately.
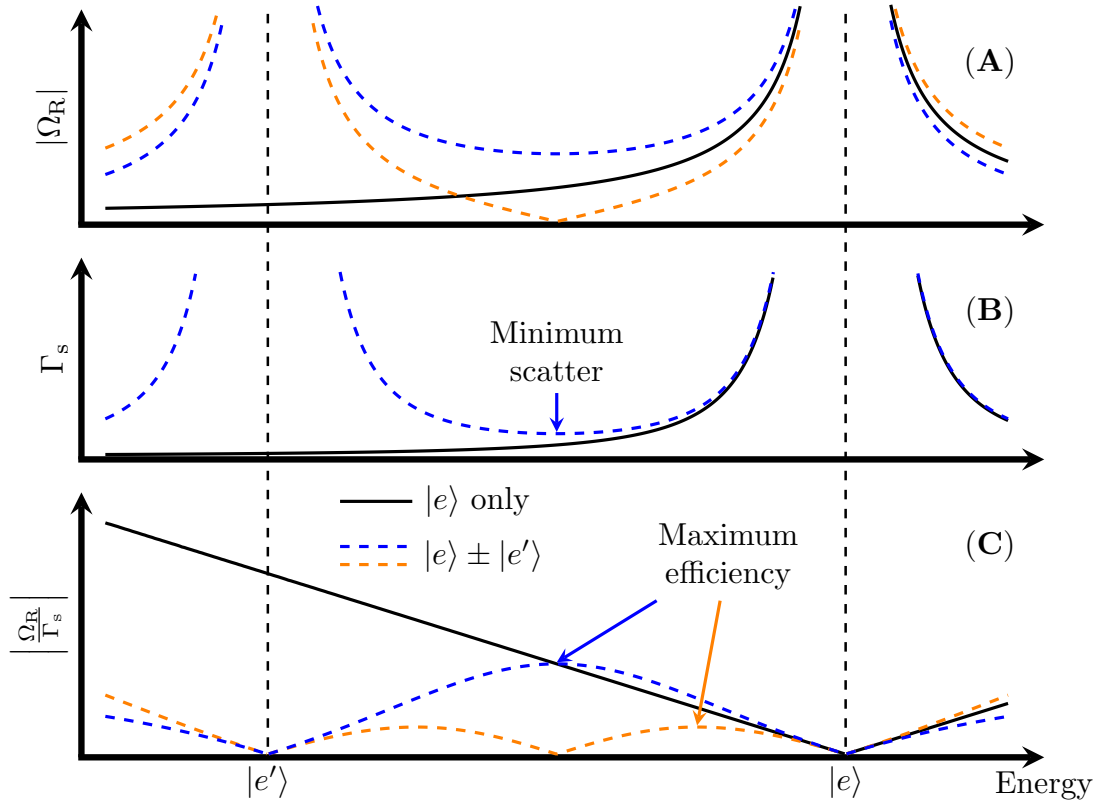
Figure 7.2: Effect of additional excited states $|e'\rangle$ on the Raman transition efficiency. (A) Depending on the sign of the coupling, there could be constructive (blue) or destructive (orange) interference on the Raman Rabi frequency Ω_{R}. (B) Increased scattering rate Γ_{s} caused by $|e'\rangle$ with a minimum between the two states. (C) Optimal detuning exists between the two states with the maximum transfer efficiency corresponding to a fraction of the state spacing.

In this case, the single photon frequency falls in between the two excited states $|e\rangle$ and $|e'\rangle$, which happens when $|e'\rangle$ is a different vibrational or electronic state. The total Raman Rabi frequency (Fig. 7.2A) is,

$$\Omega_R = \frac{\Omega_1\Omega_2}{2\Delta} + \frac{\Omega_1'\Omega_2'}{2(\Delta - \omega_e')}$$

where Ω_1' and Ω_2' are the single photon Rabi frequencies coupling $|e'\rangle$ to $|i\rangle$ and $|f\rangle$ respectively. Depending on whether $\Omega_1'\Omega_2'$ has the same (orange line) or different (blue line) sign as $\Omega_1\Omega_2$, the total Raman Rabi frequency may be cancelled or enhanced between the two excited states. On the other hand, the total scattering rate (Fig. 7.2B) is almost always increased due to the additional state, creating a local minimum between the excited states. Combining the two effects, the ratio between the Raman Rabi frequency and the scattering rate, which determines the transfer efficiency, always has a local maximum between the excited states (Fig. 7.2C).

Despite the difference in the position and value of the maximum for different $|e'\rangle$ parameters, we can summarize the effect on the transfer efficiency as a limit on the maximum detuning $\Delta_{\max}$ to a fraction of the spacing between the excited states (ω_e'). As an example, the blue and orange maxima in Fig. 7.2C corresponds to optimal single photon detuning

of $0.5\omega'_e$ and $0.15\omega'_e$ respectively. As one would expect, a larger excited state spacing usually results in a larger detuning optimum and a better transfer efficiency.

Summarizing the effect of additional excited state as a single number $\Delta_{\max}$ allows us to keep using the equation for Raman transitions with minor corrections and makes it easier to compare different state selection and transition schemes. It is also worth noting that although only one additional excited state $|e'\rangle$ is considered here, this result can be generalized when more excited states are taken into account as well. These states introduce additional smooth variation in both the Raman Rabi frequency and scattering rate and the effects on the final transition efficiency can be similarly treated as a change in the maximum detuning.

7.2.2.2 Excited State Spacing Much Smaller than Single-Photon Detuning

This is typically the case when $|e'\rangle$ is a different rotational or hyperfine state. In this case, the Raman transition is detuned from both $|e\rangle$ and $|e'\rangle$ at the same time and the two excited states behave similar to an effective state $|e''\rangle$ with modified coupling strengths and decay rate.

When the initial and final ground states have (nearly) identical spin and rotational states, which is the case for the transition to $N = 0$ states discussed in section 6.2.2, the new effective state will behave very similarly to the original ones. This is because the coupling

between the ground states and the excited states is determined by,

$$\Omega^i_{1,2} = \Omega^0_{1,2} \langle F^i_e | F_g \rangle$$

where the superscript i represents different excited states, the subscript $1, 2$ represents the initial (1) and final (2) ground state, $\Omega^0_{1,2}$ is the reduced Rabi frequency without the angular momentum projection, and F^i_e and F_g are the rotation and spin states for the excited and ground states respectively. Note that the ground states $|i\rangle$ and $|f\rangle$ both have the same F_g. This means

$$\frac{\Omega^i_1}{\Omega^i_2} = \frac{\Omega^0_1}{\Omega^0_2}$$

which is a constant. Given that the excited-state linewidths for different rotation and hyperfine states are very similar, we have the Rabi frequency to scattering rate ratio.

$$\frac{\Omega_R}{\Gamma_s} \approx \left(\sum_i \frac{\Omega^i_1 \Omega^i_2}{2\Delta} \right) \Big/ \left(\sum_i \frac{{\Omega^i_1}^2 + {\Omega^i_2}^2}{4\Delta^2} \right)$$
$$= \frac{\Omega_1 \Omega_2}{2\Delta} \Big/ \frac{\Omega_1^2 + \Omega_2^2}{4\Delta^2}$$

which is the same as the expression for a single excited state.

The properties of the effective state can be very different, however, when the initial and

final spin and rotational states are different. Nevertheless, other than the special case of complete destructive interference on the Raman Rabi frequency, the new excited state will generally have a worse ratio Ω_R/Γ_s by a constant factor. The dependence of the ratio on the detuning is not changed significantly for large detunings.

7.2.3 Cross Coupling Between Light Addressing Initial and Final States

Due to the small energy separation between the initial and final state δ, the cross coupling of the laser addressing the initial/final state on the final/initial state is another important effect in our experiment. Without the cross coupling, the total off resonance scattering rate for the initial and the final states is

$$\Gamma_{s0} = \frac{\Gamma_e \left(\Omega_1^2 + \Omega_2^2 \right)}{4\Delta^2}$$

For a given Raman Rabi frequency $\Omega_R \propto \Omega_1 \Omega_2$, this is minimized when $\Omega_1 = \Omega_2$.

When cross coupling is taken into account, however, the total scattering rate becomes[‡],

$$\Gamma_s = \frac{\Gamma_e \Omega_1^2}{4M_1^2} \left(\frac{M_1^2}{\Delta^2} + \frac{M_2^2}{(\Delta + \delta)^2} \right) + \frac{\Gamma_e \Omega_2^2}{4M_2^2} \left(\frac{M_2^2}{\Delta^2} + \frac{M_1^2}{(\Delta - \delta)^2} \right) \qquad (7.1)$$

$$\propto \frac{\Gamma_e P_1}{4} \left(\frac{M_1^2}{\Delta^2} + \frac{M_2^2}{(\Delta + \delta)^2} \right) + \frac{\Gamma_e P_2}{4} \left(\frac{M_2^2}{\Delta^2} + \frac{M_1^2}{(\Delta - \delta)^2} \right) \qquad (7.2)$$

where $P_{1,2} \propto \Omega_{1,2}^2/M_{1,2}^2$ are the powers of the laser beams 1 and 2. When $\delta \ll \Delta$ such as in our experiment,

$$\Gamma_s \approx \frac{\Gamma_e (M_1^2 + M_2^2)}{4\Delta^2} \left(\frac{\Omega_1^2}{M_1^2} + \frac{\Omega_2^2}{M_2^2} \right)$$

$$\propto \frac{\Gamma_e (M_1^2 + M_2^2)}{4\Delta^2} (P_1 + P_2)$$

For a given Raman Rabi frequency $\Omega_R \propto \Omega_1 \Omega_2 \propto \sqrt{P_1 P_2}$, this is minimized when $P_1 = P_2$. Hence, due to the strong cross coupling, we need to use the same power in both Raman beams rather than adjusting the powers to match their single photon Rabi frequencies.

Moreover, at the minimum scattering rate, we have $\Omega_2 = \Omega_1 M_2/M_1$ and the ratio

---

[‡]Here we assume that the matrix elements are the same for the two beams. This is the case when the two beams have the same polarization as in our experiment. This effect can be minimized or eliminated by selecting different polarizations for the two laser frequencies that do not couple to the other initial/final state. This would also require choosing an excited state with the same or lower angular momentum as the ground states in order to avoid cross coupling to different excited states.

between the Raman Rabi frequency and scattering rate is,

$$
\begin{aligned}
\frac{\Omega_R}{\Gamma_s} &= \frac{\Omega_1 \Omega_2}{2\Delta} \frac{4\Delta^2}{\Gamma_e \left(M_1^2 + M_2^2 \right)} \bigg/ \left(\frac{\Omega_1^2}{M_1^2} + \frac{\Omega_2^2}{M_2^2} \right) \\
&= \frac{2\Delta \Omega_1 \Omega_2}{\Gamma_e \left(M_1^2 + M_2^2 \right)} \bigg/ \left(\frac{\Omega_1^2}{M_1^2} + \frac{\Omega_2^2}{M_2^2} \right) \\
&= \frac{\Delta \Omega_1^2 M_2}{\Gamma_e M_1 \left(M_1^2 + M_2^2 \right)} \frac{M_1^2}{\Omega_1^2} \\
&= \frac{\Delta}{\Gamma_e} \frac{M_1 M_2}{M_1^2 + M_2^2}
\end{aligned}
$$

Therefore, for a given excited-state linewidth Γ_e and maximum detuning (section 7.2.2) the transfer efficiency maximizes for the smallest $M_1 M_2/(M_1^2 + M_2^2)$ which happens when the ratio M_1/M_2 is the closest to 1.

The light shift of the Raman resonance is similarly affected by the cross coupling. The differential light shift between the initial and the final state determines the resonance fluctuation as a function of light intensity fluctuation. The ratio between the light shift and the Raman Rabi frequency, i.e. line width, determines the stability requirement of our laser

indensity. With cross coupling, the differential shift is (assuming $\partial \ll \Delta$),

$$
\begin{aligned}
\Delta\partial &\approx \frac{\Omega_1^2}{4\Delta} - \frac{\Omega_1^2 M_2^2}{4\Delta M_1^2} - \frac{\Omega_2^2}{4\Delta} + \frac{\Omega_2^2 M_1^2}{4\Delta M_2^2} \\
&= \frac{M_1^2 - M_2^2}{4\Delta} \left(\frac{\Omega_1^2}{M_1^2} + \frac{\Omega_2^2}{M_2^2} \right) \\
&\propto \frac{M_1^2 - M_2^2}{4\Delta} (P_1 + P_2)
\end{aligned}
$$

which is also minimized when $P_1 = P_2$ at a given Raman Rabi frequency.

The ratio with the Raman Rabi frequency is,

$$
\begin{aligned}
\frac{\Delta\partial}{\Omega_{\mathrm{R}}} &\approx \frac{M_1^2 - M_2^2}{4\Delta} \left(\frac{\Omega_1^2}{M_1^2} + \frac{\Omega_2^2}{M_2^2} \right) \frac{2\Delta}{\Omega_1 \Omega_2} \\
&= \frac{M_1^2 - M_2^2}{2\Omega_1 \Omega_2} \left(\frac{\Omega_1^2}{M_1^2} + \frac{\Omega_2^2}{M_2^2} \right) \\
&= \frac{M_1^2 - M_2^2}{M_1 M_2}
\end{aligned}
$$

the absolute value of which is also minimized when the ratio M_1/M_2 is the closest to 1.

Due to the coupling strength difference, we have $M_2 \gg M_1$ in our experiment, which means,

$$
\left| \frac{\Delta\partial}{\Omega_{\mathrm{R}}} \right| \approx \frac{M_2}{M_1}
$$

In order to keep the resonance stable within the linewidth of the Raman resonance, i.e. Ω_R, the differential light shift $\Delta\delta$, and therefore the laser power, must be stabilized to better than M_1/M_2.

7.3 STIRAP

An alternative method often used to create and prepare the internal states of ultracold molecules is stimulated Raman adiabatic passage (STIRAP) [139]. Compared to a Raman transition, which uses detuning from the excited state to reduce scattering during the transfer, STIRAP relies on a superposition between the initial and final state as a dark state to achieve the same goal. The dark state in STIRAP is created due to a destructive interference of transition from the initial and final state to the excited state.

Similar to Raman transfer, STIRAP in an ideal three-level system can achieve full coherent transfer with arbitrarily small scattering probability when given unlimited time and power budget. However, in reality, coupling to states that exist outside the ideal three-level system always cause a non-zero probability of scattering loss (Fig. 7.3). In this section, we will apply the approach we took for Raman transition to STIRAP. We will then compare the loss caused by different practical limitations and discuss which approach should be taken under various circumstances.
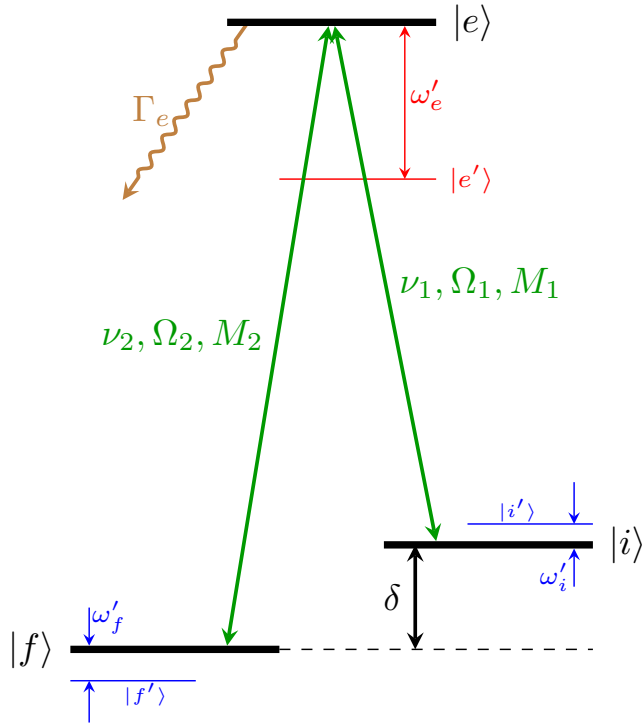
Figure 7.3: Generic model for a real STIRAP similar to Fig. 7.1. Differences are that the two beams are now on resonant with $|e\rangle$ and the Ω_1 and Ω_2 now represent the maximum single photon Rabi frequency during the STIRAP pulse for the two beams.

7.3.1 STIRAP for Ideal Three-Level System

During STIRAP, the system approximately remains in a dark state $|D(t)\rangle$

$$|D(t)\rangle = c_i(t)|i\rangle + c_f(t)|f\rangle$$

Since this state does not couple to the excited state, we have,

$$0 = \langle e|\mathbf{d} \cdot \mathbf{E}|D(t)\rangle$$

$$= c_i(t)\langle e|\mathbf{d} \cdot \mathbf{E}|i\rangle + c_f(t)\langle e|\mathbf{d} \cdot \mathbf{E}|f\rangle$$

$$= c_i(t)\Omega_1(t) + c_f(t)\Omega_2(t)$$

or

$$|D(t)\rangle = \frac{\Omega_2(t)|i\rangle - \Omega_1(t)|f\rangle}{\sqrt{\Omega_1^2(t) + \Omega_2^2(t)}}$$

In order to estimate the scattering rate, we use the fact that the wavefunction amplitude in the final state c_f is the integral of the excited state amplitude c_e and the down leg Rabi

frequency Ω_2, i.e.,[‡]

$$c_f(t) = \int_0^t \frac{i\Omega_2(t)}{2} c_e(t') dt'$$

For a complete transfer of length T, we have $c_f(0) = 0$ and $c_f(T) = 1$, therefore,

$$\int_0^T \Omega_2(t) c_e(t) dt = -2i$$

Since Ω_2 is the upper bound of $|\Omega_2(t)|$ we have,

$$\left| \int_0^T c_e(t) dt \right| \geqslant \frac{2}{\Omega_2}$$

The total scattering probability is,

$$\begin{aligned} p_{s0} &= \int_0^T \Gamma_e |c_e^2(t)| dt \\ &\geqslant \frac{\Gamma_e}{T} \left| \int_0^T c_e(t) dt \right|^2 \\ &\geqslant \frac{4\Gamma_e}{\Omega_2^2 T} \end{aligned}$$

[‡]This equation and the lower bound on scattering probability applies generally to all two-photon transfer process including Raman π-pulse. The equation we used in section 7.2 is a refinement on this limit.

156

By a similar argument, we also have,

$$p_{s0} \geqslant \frac{4\Gamma_e}{\Omega_1^2 T}$$

which is the same as the previous result for a three-level Raman system where $\Omega_1 = \Omega_2$. In the general case, these give us a lower bound on the scattering probability,

$$\min\left(p_{s0}\right) = \frac{4\Gamma_e}{\min\left(\Omega_1^2, \Omega_2^2\right) T}$$

whereas the real value in a experiement depends on the pulse shape and may be larger than this lower limit by a small constant factor. It is also easy to verify that this result agrees with the scattering probability for an optimal three-level Raman π-pulse with similar single photon Rabi frequency and pulse time. This confirms that without additional constraints from the real system or the experimental setup, neither Raman transfer nor STIRAP offers a significant advantage over the other. As we will see in the following sections, other effects in the system can favor one approach over the other.

7.3.2   ADDITIONAL INITIAL AND FINAL STATES

Similar to the case of a Raman transition (section 7.2.1), the additional initial and final states cause potential leakage out of the three-level system. This limits the minimum time

of the transfer in a way similar to that of a Raman transition.

7.3.3 Additional Excited States

For additional excited states that are further away than the single photon Rabi frequency Ω_1 and Ω_2, the contribution to the coherent transfer is minimal. However, these states can still contribute to scattering during the transfer.

The excited state will only contribute significantly to the scattering if it causes scattering from the dark state, which happens if $\Omega_1(t)/\Omega_2(t) \neq \Omega_1'(t)/\Omega_2'(t)$, where $\Omega_1'(t)$ and $\Omega_2'(t)$ are the time dependent single photon Rabi frequencies coupling $|e'\rangle$ to $|i\rangle$ and $|f\rangle$ respectively. As discussed in section 7.2.2.2, this does not happen for excited states with the same vibrational and electronic states when the initial and final spin and rotational states are identical. Similar to Ω_1 and Ω_2, we can also define $\Omega_1' \equiv \max\left(\Omega_1'(t)\right)$ and $\Omega_2' \equiv \max\left(\Omega_2'(t)\right)$. Since $\Omega_1'(t)(\Omega_2'(t))$ and $\Omega_1(t)(\Omega_2(t))$ are generated from the same beam, we have $\Omega_1'(t) \propto \Omega_1(t)(\Omega_2'(t) \propto \Omega_2(t))$. This allow the time dependent condition above: $\Omega_1(t)/\Omega_2(t) \neq \Omega_1'(t)/\Omega_2'(t)$ to be expressed as $\Omega_1/\Omega_2 \neq \Omega_1'/\Omega_2'$, which is time independent.

More quantitatively, the Rabi frequency coupling the dark state $|D(t)\rangle$ to the excited

state $|e'\rangle$ is,

$$
\begin{aligned}
\Omega'(t) =& \langle e'|\mathbf{d} \cdot \mathbf{E}|D(t)\rangle \\
=& \frac{\Omega_2(t)\Omega_1'(t) - \Omega_1(t)\Omega_2'(t)}{\sqrt{\Omega_1^2(t) + \Omega_2^2(t)}} \\
=& \frac{\Omega_1(t)\Omega_2(t)}{\sqrt{\Omega_1^2(t) + \Omega_2^2(t)}} \left(\frac{\Omega_1'}{\Omega_1} - \frac{\Omega_2'}{\Omega_2} \right)
\end{aligned}
$$

The additional scattering caused by this is,

$$
\begin{aligned}
p_s' =& \int_0^T \frac{\Gamma_e' \Omega'^2(t)}{4\omega_e'^2} \mathrm{d}t \\
=& \frac{\Gamma_e'}{4\omega_e'^2} \left(\frac{\Omega_1'}{\Omega_1} - \frac{\Omega_2'}{\Omega_2} \right)^2 \int_0^T \frac{\Omega_1^2(t)\Omega_2^2(t)}{\Omega_1^2(t) + \Omega_2^2(t)} \mathrm{d}t \\
=& C' \frac{\Gamma_e' T}{4\omega_e'^2} \left(\frac{\Omega_1'}{\Omega_1} - \frac{\Omega_2'}{\Omega_2} \right)^2 \frac{\Omega_1^2 \Omega_2^2}{\Omega_1^2 + \Omega_2^2}
\end{aligned}
$$

which has the form of an off-resonance scattering probability. C' is a dimensionless number depending only on the pulse shape defined as

$$
C' \equiv \frac{\Omega_1^2 + \Omega_2^2}{\Omega_1^2 \Omega_2^2 T} \int_0^T \frac{\Omega_1^2(t)\Omega_2^2(t) \mathrm{d}t}{\Omega_1^2(t) + \Omega_2^2(t)}
$$

It is worth noting that although there are not two different cases as in the discussion for a Raman transition in section 7.2.2 due to the lack of detuning in STIRAP, the difference

159

between excited states with different spacings may still play an important role when comparing Raman transition to STIRAP. This is discussed briefly at the end of section 7.3.5.1.

7.3.4 Cross Coupling Between Light Addressing Initial and Final States

As is the case for a Raman transition (section 7.2.3), the coupling of each beam on the other initial or final state can cause increased scattering. The total scattering probability caused by the cross coupling is[‡],

$$
\begin{aligned}
p_s'' &= \int_0^T \frac{\Gamma_e \Omega_1^2(t)}{4M_1^2} \frac{M_2^2}{\delta^2} \left|c_f(t)\right|^2 + \frac{\Gamma_e \Omega_2^2(t)}{4M_2^2} \frac{M_1^2}{\delta^2} \left|c_i(t)\right|^2 \mathrm{d}t \\
&= \frac{\Gamma_e}{4\delta^2} \int_0^T \frac{M_2^2}{M_1^2} \frac{\Omega_1^4(t)}{\Omega_1^2(t) + \Omega_2^2(t)} + \frac{M_1^2}{M_2^2} \frac{\Omega_2^4(t)}{\Omega_1^2(t) + \Omega_2^2(t)} \mathrm{d}t \\
&= \frac{\Gamma_e T}{4\delta^2} \left(C_1'' \frac{M_2^2}{M_1^2} \frac{\Omega_1^4}{\Omega_1^2 + \Omega_2^2} + C_2'' \frac{M_1^2}{M_2^2} \frac{\Omega_2^4}{\Omega_1^2 + \Omega_2^2} \right)
\end{aligned}
$$

where C_1'' and C_2'' are two dimensionless numbers depending only on the pulse shape defined as,

$$
C_i'' \equiv \frac{\Omega_1^2 + \Omega_2^2}{\Omega_i^4 T} \int_0^T \frac{\Omega_i^4(t)\mathrm{d}t}{\Omega_1^2(t) + \Omega_2^2(t)}
$$

[‡]Here we are making the same assumption of identical matrix elements for the two beams as the one we made for Raman transition in section 7.2.3.

7.3.5 Raman Transfer versus STIRAP

As one may expect, the scattering probability and the efficiency of a STIRAP transfer depends on the precise pulse shape used. While it may be possible to construct a STIRAP pulse shape with significantly different constant values, we will focus our discussion on more traditional shapes and assume $C_1'' \approx C_2'' \approx C' \approx 1$.

We will compare the scattering probability during STIRAP to that of a Raman π-pulse in two limiting cases depending on whether the contribution from the additional excited or ground state are more significant.

7.3.5.1 More Significant Contribution from Additional Excited State

This is the case where the excited-state separation ω_e' is significantly smaller compared to the ground-state separation δ. By choosing an optimal pulse time, the minimum scattering probability for the STIRAP pulse is,

$$
\begin{aligned}
p_s^{\text{STIRAP}} &\approx 2\sqrt{\frac{4\Gamma_e}{\min\left(\Omega_1^2, \Omega_2^2\right)} \frac{\Gamma_e'}{4\omega_e'^2} \left(\frac{\Omega_1'}{\Omega_1} - \frac{\Omega_2'}{\Omega_2}\right)^2 \frac{\Omega_1^2 \Omega_2^2}{\Omega_1^2 + \Omega_2^2}} \\
&= \frac{\sqrt{\Gamma_e \Gamma_e'}}{\omega_e'} \left|\frac{\Omega_1'}{\Omega_1} - \frac{\Omega_2'}{\Omega_2}\right| \frac{2\max\left(\Omega_1, \Omega_2\right)}{\sqrt{\Omega_1^2 + \Omega_2^2}} \\
&\geqslant \frac{\sqrt{\Gamma_e \Gamma_e'}}{\omega_e'} \left|\frac{\Omega_1'}{\Omega_1} - \frac{\Omega_2'}{\Omega_2}\right|
\end{aligned}
$$

For Raman π-pulse,

$$
\begin{aligned}
p_s^{\text{Raman}} &= \frac{\pi\Gamma}{2\Omega_R} \\
&= \frac{\pi}{2}\frac{\Gamma_e\left(\Omega_1^2 + \Omega_2^2\right)}{4\Delta_{\text{max}}^2}\frac{2\Delta_{\text{max}}}{\Omega_1\Omega_2} \\
&= \frac{\pi\Gamma_e}{4\Delta_{\text{max}}}\frac{\left(\Omega_1^2 + \Omega_2^2\right)}{\Omega_1\Omega_2} \\
&\geqslant \frac{\pi\Gamma_e}{2\Delta_{\text{max}}}
\end{aligned}
$$

The last inequality for both takes the equal sign when $\Omega_1 = \Omega_2$. Comparing the results and noting that Δ_{max} is a fraction of ω_e', we see that the two scale similarly to the excited-state spacing. However, given that in the common cases we have $\Delta_{\text{max}} < \omega_e'$ and $|\Omega_1'/\Omega_1 - \Omega_2'/\Omega_2| < 1$, using STIRAP can potentially reduce the total scattering in this case.

Note that the discussion above implicitly assumes that the relevant ω_e' is the same for Raman transition and STIRAP. However, as we saw in section 7.3.3 and 7.2.2.2, this may not be the case for hyperfine and rotational structures in the excited state when the initial and final states have different spin states. The ω_e' for STIRAP in this case is the hyperfine or rotational splitting and may be significantly smaller compared to the ω_e' for the Raman transition, which is the vibrational state spacing. As a result, STIRAP may not be as favorable compared to Raman anymore. The best option in this case would require more in-depth comparisons of the different effects and will not be discussed here in more detail since it is

not relevant in our experiment.

7.3.5.2   More Significant Contribution from Additional Ground State

With the assumption of $C_1'' \approx C_2'' \approx 1$ the scattering due to cross coupling for STIRAP is now,

$$
\begin{aligned}
p_s'' &= \frac{\Gamma_e T}{4\delta^2} \left(\frac{M_2^2}{M_1^2} \frac{\Omega_1^4}{\Omega_1^2 + \Omega_2^2} + \frac{M_1^2}{M_2^2} \frac{\Omega_2^4}{\Omega_1^2 + \Omega_2^2} \right) \\
&\geqslant \frac{\Gamma_e T}{2\delta^2} \left(\Omega_1^2 + \Omega_2^2 \right) \frac{M_1^2 M_2^2}{(M_1^2 + M_2^2)^2}
\end{aligned}
$$

and the minimum is taken when $M_2/M_1 = \Omega_2/\Omega_1$[‡] The minimum total scattering rate for STIRAP is therefore,

$$
\begin{aligned}
p_s^{\mathrm{STIRAP}} &\approx 2 \sqrt{ \frac{4\Gamma_e}{\min\left(\Omega_1^2, \Omega_2^2\right)} \frac{\Gamma_e}{2\delta^2} \left(\Omega_1^2 + \Omega_2^2 \right) \frac{M_1^2 M_2^2}{(M_1^2 + M_2^2)^2} } \\
&= 2\sqrt{2} \frac{\Gamma_e}{\delta} \frac{M_1 M_2}{M_1^2 + M_2^2} \frac{\sqrt{\Omega_1^2 + \Omega_2^2}}{\min\left(\Omega_1, \Omega_2\right)} \\
&= 2\sqrt{2} \frac{\Gamma_e}{\delta} \frac{\max\left(M_1, M_2\right)}{\sqrt{M_1^2 + M_2^2}} \approx 2\sqrt{2} \frac{\Gamma_e}{\delta}
\end{aligned}
$$

[‡]Same as Raman transition.

For Raman transition

$$
\begin{aligned}
p_{\text{s}}^{\text{Raman}} &= \frac{\pi \Gamma}{2 \Omega_{\text{R}}} \\
&= \frac{\pi \Gamma_e}{2 \Delta} \frac{M_1^2 + M_2^2}{M_1 M_2} \\
&\approx \frac{\pi \Gamma_e}{2 \Delta} \frac{\max (M_1, M_2)}{\min (M_1, M_2)}
\end{aligned}
$$

We can see that when the single photon Rabi frequency is changed to minimize cross coupling scattering, the Raman transition can be more strongly affected by the matrix element imbalance. However, if the Raman transition can use a detuning

$$
\Delta > \frac{\max (M_1, M_2)}{\min (M_1, M_2)} \delta
$$

then the scattering probability for a Raman transition can be made smaller than that of STIRAP.

7.3.5.3 CONCLUSION

In our experiment, we have an initial and final-state separation of $< 1 \, \text{GHz}$ and a matrix element ratio of < 30. This means that as long as we can use a single photon detuning of more than $\approx 30 \, \text{GHz}$, the total scattering probability for a Raman transition will be smaller than that of STIRAP. Since this detuning can be achieved easily, a Raman π-pulse should

be preferred in our experiment.

The comparison so far has been focused on the scattering probability from the Raman or STIRAP beams. There are also a few other more technical reasons we preferred Raman versus STIRAP in our experiment.

1. We use the tweezer beam as the Raman beam for transfer in order to reduce scattering from external sources (section 6.2). Doing this for STIRAP while optimizing the pulse shape for transfer is more challenging.

2. Apart from scattering, the additional excited and ground state also causes a power-dependent, and therefore time-dependent, light shift. A STIRAP pulse in the presence of these shifts must vary the frequency of the two beams in addition to the power in order to maintain the dark state. This is also technically challenging to do.

As a summary, for a two-photon transfer to a weakly bound molecular state, it is likely that a Raman transition is the preferred technique. However, for transferring to a deeply bound molecular state, which is where STIRAP has been used in previous experiments, STIRAP can have an advantage over a Raman transition if the energy separation between the initial and final states are large enough and when the hyperfine and rotational structures in the excited state does not cause significant scattering.

7.4 States Selection

From section 7.2 we see that the transfer efficiency is directly related to the excited-state linewidth, the maximum detuning and the matrix elements ratio (M_1/M_2). In this section,
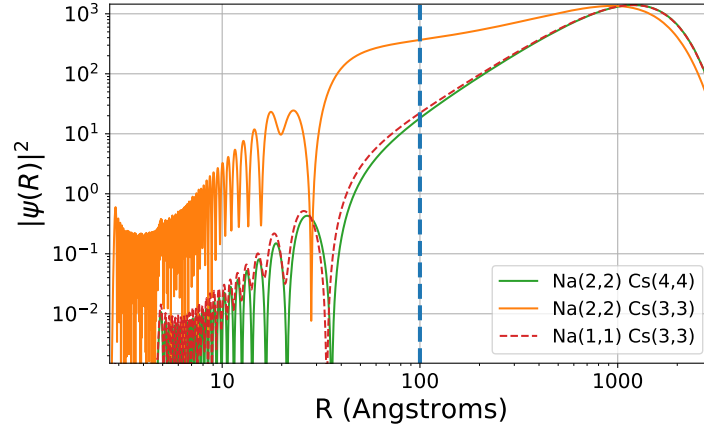
Figure 7.4: Enhancement of short range wavefunction. The large scattering length for the $Na(2, 2)$, $Cs(3, 3)$ state creates an interaction shift comparable to the axial trapping frequency. This causes a significant change in the relative wavefunction especially at short internuclear distance (R). Compared to other spin states with weaker interactions, the wavefunction at short distance $(R < 100 \text{ Å}$, left of the dashed line) is significantly enhanced.

we will discuss how these, as well as other technical constraints, affect the choices of states we use for the Raman transfer.

7.4.1 INITIAL ATOMIC STATE

The choice of initial state can affect the transfer efficiency by changing the matrix element M_1 and therefore the matrix elements ratio. Since for most choices of the atomic and molecular states we have $M_1 < M_2$, we would like to choose an atomic initial state with the largest M_1 possible. Unlike the selection of final state (section 7.4.3), maximizing M_1 can improve the matrix element ratio as well as shorten the transfer time to decrease sensitivity to technical noise.

As discussed in section 5.3.3, M_1 is only sensitive to the wavefunction at a short inter-

atomic distance that is comparable to the size of the molecule. Therefore, states with a large wavefunction value at short interatomic distance should generally have a larger M_1. In addition to the confinement potential and the motional state of the atoms, this is also affected by the interaction between the atoms. A strong interaction, either attractive or repulsive, can significantly change the relative motional wavefunction of the atoms. This effect can be seen in Fig. 7.4 and is especially significant for the $|\mathrm{Na}(2,2), \mathrm{Cs}(3,3)\rangle$ state when the interaction energy scale is comparable to that of the motional energy as seen in section 4.3.2.

7.4.2 EXCITED STATE

Based on theory calculation, most of the molecular excited states have a linewidth Γ'_e very similar to those of the Cesium D lines between $2\pi \times 5\,\mathrm{MHz}$ to $2\pi \times 10\,\mathrm{MHz}$ due to optical decay processes. States above the Cesium $6^2\mathrm{P}_{1/2}$ state, however, could non-radiatively decay to the Cs $6^2\mathrm{P}_{1/2}$ and Na $3^2\mathrm{S}_{1/2}$ states via pre-dissociation which significantly increases the linewidth and should be avoided.

The other factor that affects excited-state selection is the maximum detuning Δ_{max}. Due to larger FCF with the ground atomic and weakly bound molecular state, previous attempts at Raman spectroscopy typically use an excited state closed to the dissociative threshold as the intermediate state [140, 141]. However, the smaller inter-state spacing and the smaller detuning from the atomic excited state means that these states have a relatively small Δ_{max} and therefore a lower coherent transfer efficiency. On the other hand, a deeply bound
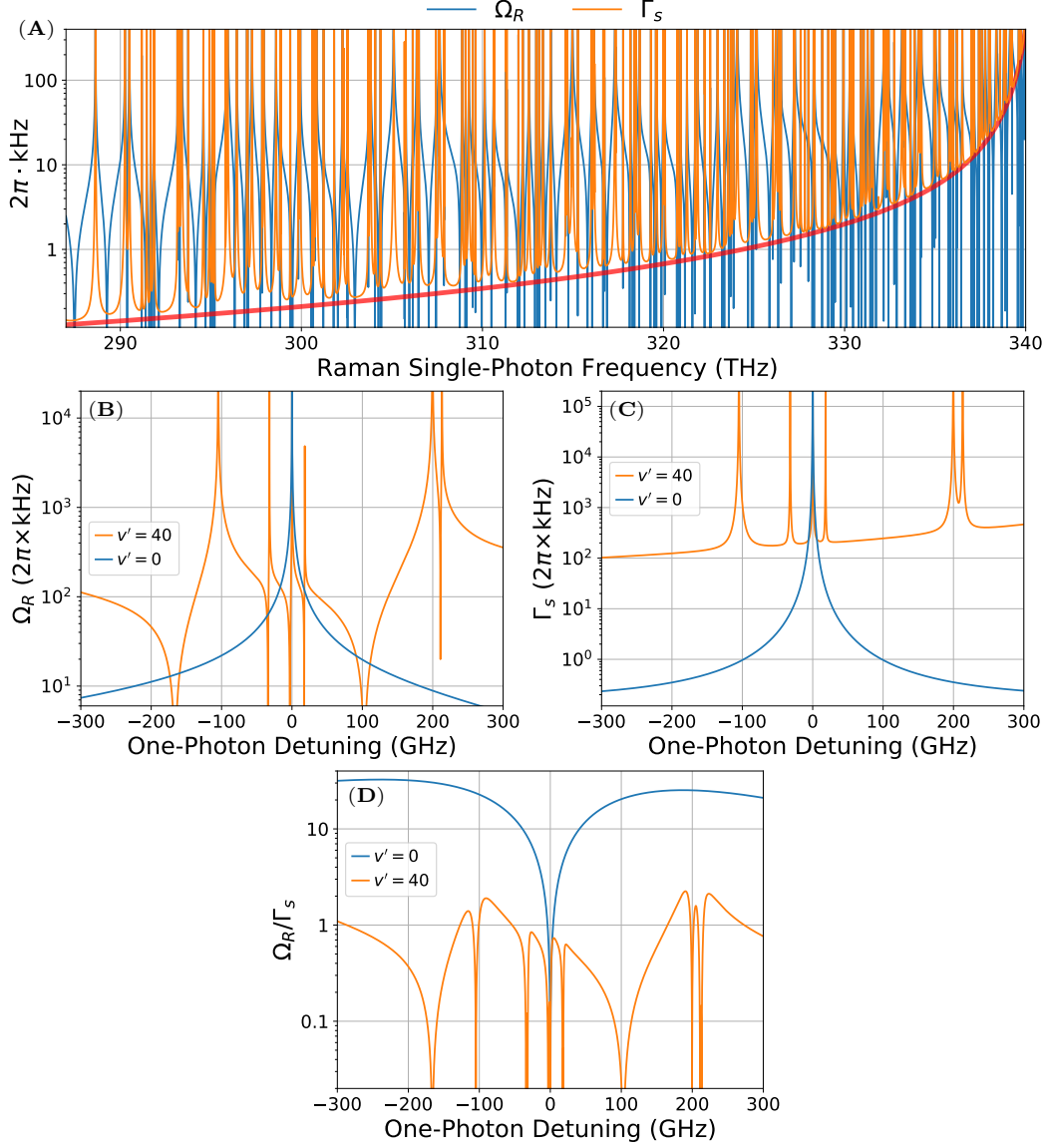
Figure 7.5: Comparison between using a weakly bound and a deeply bound excited state as intermediate state for the Raman transition. (A) Raman Rabi frequency (Ω_R) and scattering rate (Γ_s) as a function of the tweezer/Raman frequency. An overall decrease of both quantities can be observed with increasing detuning from the atomic threshold. The red line shows the contribution to Γ_s from near-threshold states. (B) The deeply bound excited state ($v' = 0$, blue lines) has a smaller Raman Rabi frequency (Ω_R) compared to the weakly bound excited state ($v' = 40$, orange lines). (C) However, the lower scattering rate (Γ_s) allows a much larger Δ_{max}, which results in a larger Raman Rabi frequency to scattering rate ratio as shown in (D).

168

excited state has a significantly higher Δ_{max} and is the preferred choice for coherent Raman transfer.

In the experiment, we use numerical simulation to calculate the Raman transfer efficiency for any given Raman beam wavelength using the multi-channel ground-state wavefunctions provided to us by Jeremy Hutson and taking into account all the states of 8 excited molecular state potentials [134–136, 142, 143] and the continuum [144]. Fig. 7.5B-D shows the result near a deeply bound and weakly bound excited state. Despite having a lower Raman Rabi frequency, the deeply bound state has significantly higher transfer efficiency and is used as the intermediate state for coherent Raman transfer in our experiment. The scattering due to the near-threshold state is very important as can be seen from the red line in Fig. 7.5A.

7.4.3   FINAL MOLECULAR STATE

In addition to the scattering and light shift considerations discussed above, the transition can also be affected by external magnetic fields. We minimize the effect of magnetic field noise on the transition by using molecular and atomic states that are in the same molecular potential, i.e. molecular bound state in the potential that asymptotes to the atomic state. For weakly bound molecular states, i.e. binding energy smaller than or comparable to the hyperfine energy scale, this ensures that the atomic and molecular states have maximally overlapping spin states and therefore a small differential Zeeman shift that can affect the

Raman resonance frequency. The similarity in the spin state between the initial and final states also minimizes the effect of hyperfine and rotational states near the excited states as we have seen in section 7.2.2.2.

Because of the weak coupling between the atomic and molecular states, the Raman transition has a relatively low Rabi frequency. This also means a longer transfer time over which the Raman lasers must remain coherent. In order to lower the requirement on our Raman and tweezer laser, we select the first bound state, i.e. smallest binding energy, as the final molecular state. This ensures the maximum Raman Rabi frequency. Additionally, the typical binding energy for these states are $< 1\,\mathrm{GHz}$ which is a frequency difference that can be generated using AOM's so that the coherence between the two beams is greatly improved.

7.5 Raman Transfer Results

The setup and sequence for forming the molecule is very similar to those used in the Raman spectroscopy previously mentioned in section 6.2.1 that drives the two-photon transition by adding a second frequency to the tweezer light. Nevertheless, a few changes were made to the sequence in order to improve the transfer efficiency and the signal to noise.

1. The initial $|\mathrm{Na}(2,2), \mathrm{Cs}(3,3)\rangle$ state is prepared by driving the interaction shift resonance from $|\mathrm{Na}(2,2), \mathrm{Cs}(4,4)\rangle$ after the two atoms are merged into the same tweezer. As discussed in section 4.4, the strong interaction between the atoms allows preparation of relative motional ground state with low background.
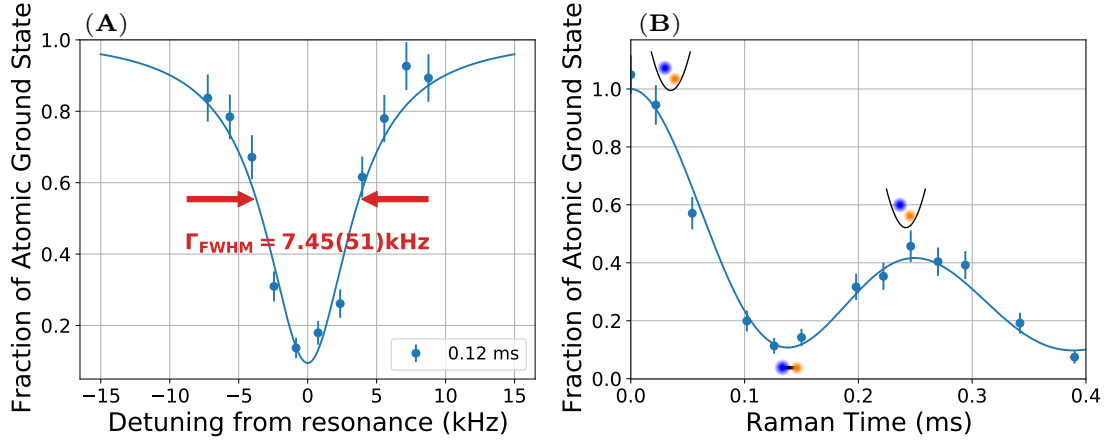
Figure 7.6: (A) Raman resonance after optimizing for transfer coherence, showing a Fourier limited linewidth. The solid line shows a fit to a Lorentzian line shape used to determine the linewidth. (B) Time scan on the Raman Resonance, showing coherent Rabi oscillations. The illustration on the plot marks when the atom pair is associated into a weakly bound molecule and then dissociated back to atoms.

2. Instead of using a smaller detuning and longer time to maximize the signal of the resonance, we increased the single photon detuning to 145 GHz and used short pulse times (<1 ms) to reduce the scattering and the linewidth of the resonance.

3. We added a narrow bandpass filter to reduce the spectral noise from the laser. This will be discussed in more detail below in section 7.5.1.

With these changes, the narrowest linewidth we were able to observe using 15 mW of total power in the tweezer is shown in Fig. 7.6A. The full width half maximum (FWHM) of 7.45(51) kHz is consistent with the Fourier limited linewidth of 7 kHz for a π-pulse of 0.12 ms used in the experiment. This is evidence that the linewidth is mainly determined by the Raman Rabi frequency rather than the lifetime of the molecule, suggesting that we are in the coherent regime. We can confirm this by varying the pulse time on the Raman resonance and the resulting decaying Rabi flop can be seen in Fig. 7.6B. The coherence in the

molecule creation signals the successful transfer of the control of single atoms to the control on the single molecule. Because of this, the molecules we created are in a single internal spin state with higher than 60 % probability of being in the motional ground state in the tweezer.

Based on the Rabi flopping signal, we can infer that 57 % of the atoms that were prepared in the relative motional ground state have been transferred to the molecule. This is the first time coherent optical transfer from atoms to molecules has been demonstrated without the help of a narrow-linewidth excited state. Nevertheless, the transfer efficiency is lower than the prediction from the theory, which, we believe, is caused by the molecule lifetime. Below, we will discuss some of the possible causes for the low transfer efficiency. In section 7.5.1 we will focus on technical sources and in section 7.5.2 we will measure the properties of the molecular state and the transition in order to compare it to the theory prediction.

7.5.1 Effect of laser spectral noise

One of the most important technical sources affecting the transfer efficiency is the spectral noise from the tweezer. The 1038 nm tweezer light we used is generated by amplifying an external-cavity diode laser (ECDL) seed using a Raman fiber amplifier. In a typical ECDL setup using grating feedback, although the external cavity selects a single preferred mode within the gain bandwidth of the laser diode in the feedback path, the output path does not
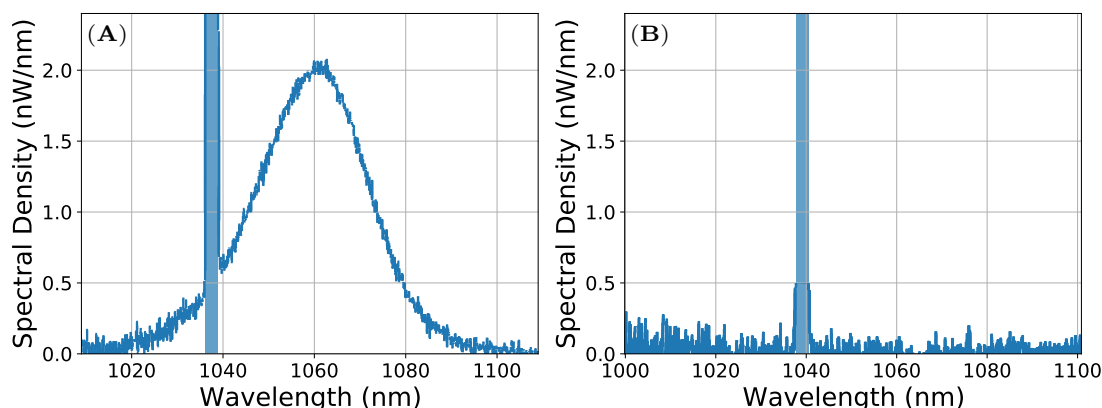
Figure 7.7: Spectra of the tweezer beam (A) before and (B) after the ASE filter. The power in the desired output frequency from the laser is 20 ~ 200 μW where the uncertainty is caused by saturation of the spectrum analyzer. This saturated range is shown as the vertical blue bands in both plots. The exact position of this band depends on the scan setting which causes it to be slightly different between the two spectra. (A) The spectrum before the ASE filter clearly shows a broad band spectral impurity approximately matching the gain bandwidth of the laser diode. This noise spans tens of nm and can potentially cover multiple molecular excited states causing increased scattering. (B) With the ASE filter, the spectrum is consistent with the background.

have a filter, allowing the amplified spontaneous emission (ASE) from the diode to get into the laser output. We observed this effect on our laser using an optical spectrum analyzer, as shown in Fig. 7.7A. Although the absolute power in the ASE is very low, it could resonantly couple to multiple molecular lines causing significant scattering during the Raman transition.

This is a common problem for systems with a large number of excited states, especially molecules, and ASE filters have been developed to address this. In our experiment, we use SureBlock ultra narrow-band notch filter from Ondax with part number 114-ER407-015, which is based on a volume holographic grating and has a FWHM of ≈ 30 GHz. We added
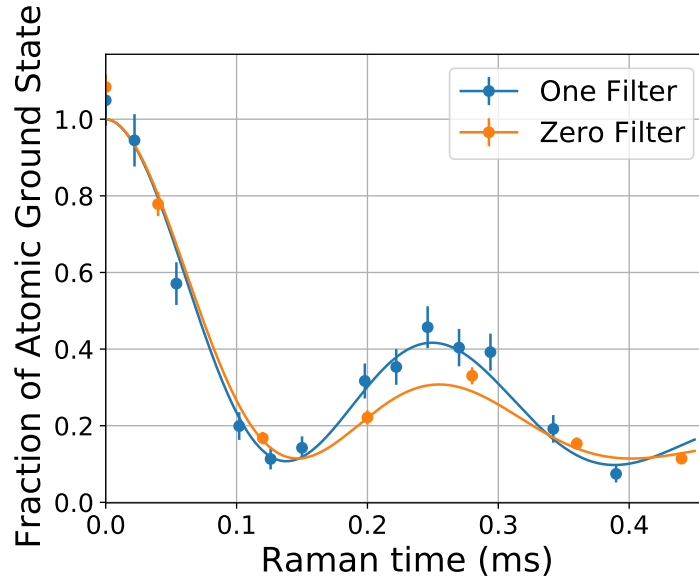
Figure 7.8: Rabi flopping without ASE filter showing a shorter coherence time compared to that with one ASE filter. The blue line shows the same data as Fig. 7.6B for direct comparison. The condition between the two lines are identical otherwise.

the filter after the Raman fiber amplifier[‡] and the spectrum of the laser after the filter is shown in Fig. 7.7B. As mentioned above, this is the condition under which the Rabi flopping in Fig. 7.6B is taken. Comparing it to a similar measurement without the ASE filter shown in Fig. 7.8, we can see the filter clearly improved the contrast of the oscillation. More quantitatively, the Raman Rabi frequency is not affected by the filter as expected whereas the coherence time of the oscillation is increased from $0.170(10)$ ms to $0.244(19)$ ms when the ASE filter is added. It is worth noting that depending on the wavelength range of the spectral noise, more precisely the FCF of the transition within the range, the scattering rate measurement can be more sensitive than the spectrum analyzer. In particular, noise on the

---

[‡]Before passing through the beam path shown in Fig. 6.3
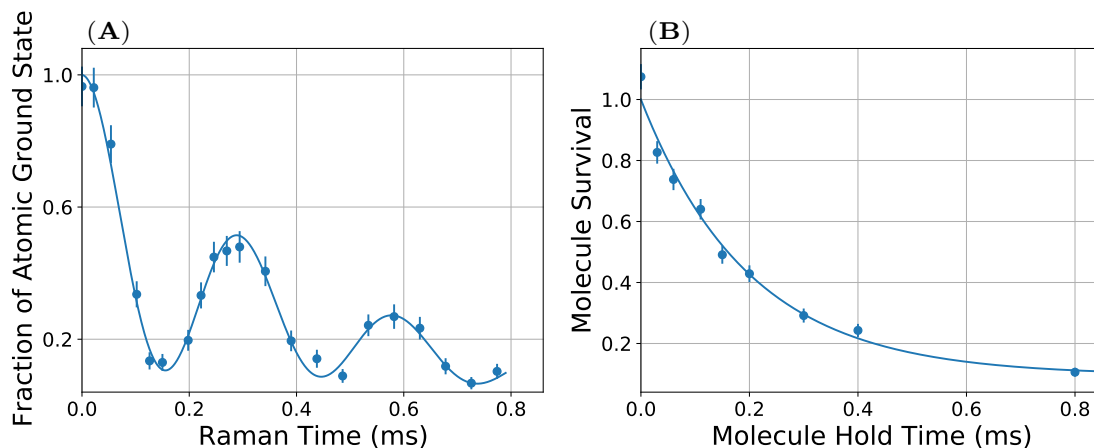
Figure 7.9: (A) Rabi flopping and (B) molecule lifetime measurement with a second ASE filter after the fiber showing further reduction in scattering rate.

level of $\approx 0.1\,\mathrm{ppm/nm}$ ($\approx 0.01\,\mathrm{nW/nm}$ in Fig. 7.7) near the atomic transition wavelength is enough to cause kHz of scattering. Because of this, we only use Fig. 7.7B to qualitatively confirm the effectiveness of the filter and rely on the specification of the filter to estimate the cleanliness of the spectrum after the filter.

In addition to the diode laser, broad spectral noise has also been observed from non-linear effects in the fiber. Although we cannot see such noise on the spectrum directly, we checked whether this has an effect on the molecule by adding another ASE filter after the last fiber in the beam path. The best result from these tests is shown in Fig. 7.9A which indeed shows an improvement in the coherence time to $0.398(17)$ ms. We also measured the molecular lifetime under this condition directly by preparing the molecule with a π-pulse and then using a second π-pulse to dissociate the molecule back to atoms after a variable wait time. The result in Fig. 7.9B shows a molecular lifetime of $0.1992(87)$ ms consistent

with the decay of the Rabi oscillation. However, adding the filter after the fiber potentially has a negative impact on other properties of the tweezer, including beam shape, power variation and pointing fluctuation, that we have not been able to characterize yet. Future experiments using a beam path that better integrate the filter needs to be used to investigate the effect of the tweezer noise more accurately.

7.5.2 Scaling of Raman Transition Parameters

The Rabi flopping signal shown above is caused by a combination of many effects (including the ones shown in section 7.2), making it difficult to identify the reason for the transfer efficiency that is lower than expected. Because of this, we vary various experimental parameters and measure how they affect the Raman transition. This allows us to distinguish between different mechanisms based on their different responses to the parameters. As mentioned in section 7.5.1, due to the potential issues with the ASE filter after the fiber, the setup using one ASE filter before the fiber is currently the most reliable configuration that offers the lowest scattering rate. Therefore, for the measurements in this section, this is the setup we used to measure the scattering rate. For properties that are not directly related to scattering, for example light shift and Rabi frequency, we will also use data that were taken before the ASE filter was added.

The parameters of the transition that we can easily vary are the power and the detun-

ing of the tweezer[‡]. The tweezer power changes the single photon Rabi frequencies both by changing the field strength and by changing the confinement which affects the relative atomic wavefunction but not the molecular wavefunction. We will compare the measured power scaling with the theory calculation to check for unknown loss mechanisms. Based on the discussion about extra excited states in section 7.2.2, we see that for most properties of the Raman transition, there is a term attributed to the desired excited state $|e\rangle$ (i.e. the $v' = 0$ state) and other terms that are caused by the combined effect of other excited states. As a function of the single-photon detuning, the first term scales the same way as a simple three-level Raman transition whereas the second term can have more complex scaling but generally varies slower than the first term due to the larger detunings from the excited states involved. In the study below, we will treat the contribution from other states as a constant background[§] over the range of frequencies we scan. In other words, we fit the detuning dependence of each property as an offset plus the contribution from the $v' = 0$ state (either $1/\Delta$ or $1/\Delta^2$). We will focus more on the $v' = 0$ term since it is easier to compare to the theory prediction. However, we will also discuss the effect of the background term on the transfer efficiency.

The properties we can directly measure from the transitions are the resonance frequency f_R,

---

[‡]We of course also vary the Raman pulse time and the two-photon detuning but these are used to determine the transition parameters and are not treated as different conditions.

[§]Constant here means independent of the single photon detuning. It could, however, depend on other variables including the tweezer power.

Table 7.1: Fitted Raman transition parameters from Fig. 7.6B and 7.10.

f_R (MHz)	Ω_R ($2\pi \times$ kHz)	Γ_a ($2\pi \times$ Hz)	Γ_m ($2\pi \times$ kHz)
770.60823(11)	3.971(89)	24.5(22)	1.30(10)

Raman Rabi frequency Ω_R, and the two scattering rates for the atomic Γ_a and molecular

states Γ_m. We measure these by fitting both the time (i.e. Rabi flopping) and frequency scan

to a single model. For a measurement of the Raman transition at frequency f, the time evo-

lution of the system is determined by,

$$
\begin{pmatrix} \psi_a(t) \\ \psi_m(t) \end{pmatrix} = e^{-iHt} \begin{pmatrix} \psi_a(0) \\ \psi_m(0) \end{pmatrix} = e^{-iHt} \begin{pmatrix} 1 \\ 0 \end{pmatrix}
\tag{7.3}
$$

where the effective non-Hermitian Hamiltonian H is

$$
H = -\frac{i}{2} \begin{pmatrix} \Gamma_a + i(f - f_R) & \Omega_R \\ -\Omega_R & \Gamma_m - i(f - f_R) \end{pmatrix}
$$

The survival of both Na and Cs atom after the Raman transition is fitted to $\left|\psi_a(t)\right|^2$ from

Eq. 7.3. Additionally, since the atomic loss rate Γ_a is slow compared to the Raman transi-

tion time, it is measured separately using the two-body lifetime of the atoms to obtain a

more accurate number. An example of such fitting is shown in Fig. 7.6B and 7.10, which

result in the fitting parameters shown in table 7.1.

After repeating this for multiple tweezer powers P and frequencies f_{twr}, we first look at
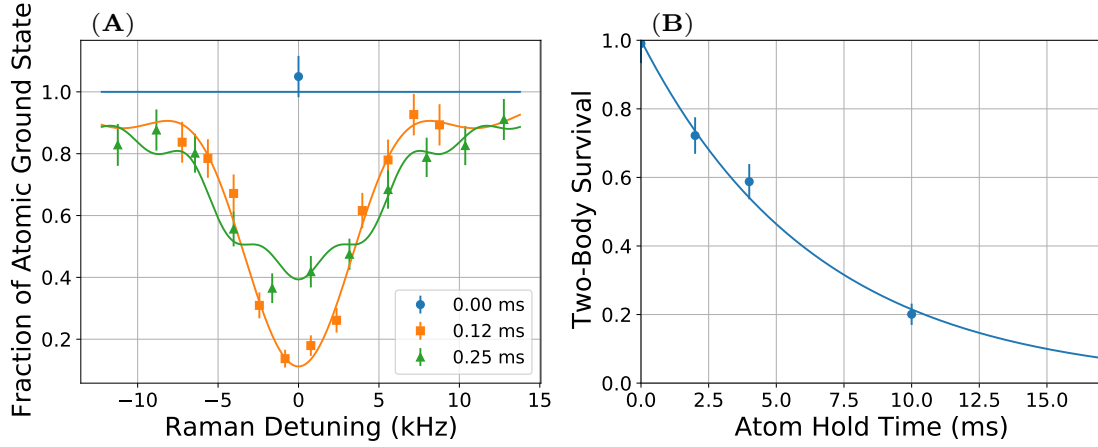
Figure 7.10: Fitting of Raman transition parameters. (A) Raman spectrum for different times. The 0.12 ms data was previously shown in Fig. 7.6A and is fit to a more accurate model in this plot. (B) Two-body atom loss measurement with longer time to more accurately determine the atomic lifetime. The fit also includes data from Fig. 7.6B.

the light shift of the transition. The resonance frequencies are fitted to the formula,

$$f_{\mathrm{R}} = \left(f_{\mathrm{R}0} + a \cdot P + b \cdot P^2\right) + \frac{c \cdot P}{f_{\mathrm{PA}0} - f_{\mathrm{twr}}} \tag{7.4}$$

where the first term is the background contribution and the second term is due to the $v' = 0$ state. Since we have $\Omega_2^2 \gg \Omega_1^2$, we assume the $v' = 0$ term is only caused by the coupling between the excited state $|e\rangle$ and the final molecular state $|f\rangle$. Taking into account the cross coupling effect, we have,

$$c \cdot P = \frac{\Omega_2^2}{2} \tag{7.5}$$

179
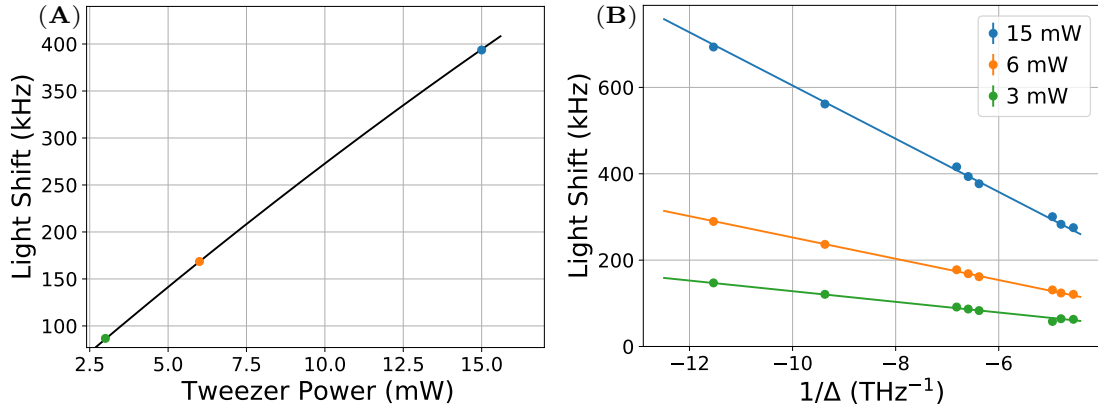
Figure 7.11: Fitting of Raman light shift as a function of tweezer power and detuning. (A) The light shift varies approximately linearly with the tweezer power with a small quadratic term. (B) The light shift is proportional to $1/\Delta$ as expected from theory prediction.

Table 7.2: Fitted Raman light shift from Fig. 7.11. Note that the frequencies in this table and Fig. 7.11 are linear frequencies whereas the quantities used in Eq. 7.4 and 7.5 are typically angular frequencies.

f_{R0} (MHz)	f_{PA0} (GHz)	a (kHz/mW)	b (Hz/mW^2)	c (MHz ·GHz/mW)
770.200516(24)	288711	2.194(17)	−199.13(58)	4.1083(46)

For the background term, we have the "raw" resonance frequency[‡] f_{R0}, a linear term $a \cdot P$ caused by the scalar AC Stark shift from other states and a quadratic term $b \cdot P^2$ that we attribute to the vector AC Stark shift. In principle the vector AC Stark shift may also depend on the single-photon detuning but the dependence is not significant within the frequency range we measured. The fit is shown in Fig. 7.11B with Fig. 7.11A showing the near linear dependence of the light shift on the tweezer power. The fitting parameters are shown in table 7.2. Most importantly, the down-leg Rabi frequency is $2\pi \times 90.645(50)$ MHz/$\sqrt{mW}$ or $2\pi \times 351.07(19)$ MHz for 15 mW tweezer power. This number is within 50 % of

---

[‡]Note that the Zeeman shift is still included.

Table 7.3: Fitted result from Fig. 7.12 for Eq. 7.6.

$a\ (2\pi \times \mathrm{Hz/mW^{1.29}})$	$b\ (4\pi^2 \times \mathrm{kHz \cdot GHz/mW^{1.29}})$
$-68.3(27)$	$28.00(33)$

the value $2\pi \times 148\,\mathrm{MHz}/\sqrt{\mathrm{mW}}$ calculated from theory. The background light shift is

$2.194(17)\,\mathrm{kHz/mW}$ which results in $\approx 8\,\%$ of the light shift for the previous measure-

ment (Fig.7.8) and is not a significant factor.

Next we study the Raman Rabi frequency. Unlike the light shift, this quantity is strongly

affected by the coupling between the atomic state and the excited molecular state. For weak

confinements and interactions, this coupling scales as the amplitude of the wavefunction at

zero relative distance, or square root of the probability density, which scales as $P^{0.375}$ for a

3D harmonic trap[‡]. For stronger confinements and interactions, however, this scaling starts

to saturate as the scattering length a approaches the harmonic oscillator length β and does

not follow a simple power law scaling anymore. This is the regime we have for the strongly

interacting $|\mathrm{Na}(2,2),\mathrm{Cs}(3,3)\rangle$ state. Nevertheless, in order to simplify the fitting, we use a

numerical calculation to determine an approximate scaling of $P^{0.29}$ for our scattering length

within the range of tweezer powers we measure. This results in a scaling of Ω_R propor-

tional to $P^{1.29}$ which can be verified using measurements with the same tweezer frequency

at different powers, as shown in Fig. 7.12A. We fit the Ω_R for different detunings to the

---

[‡]$|\psi(0)|^2 \propto \prod_{i=x,y,z} \beta_i^{-1} \propto \prod_{i=x,y,z} \omega_i^{1/2} \propto P^{3/4}$
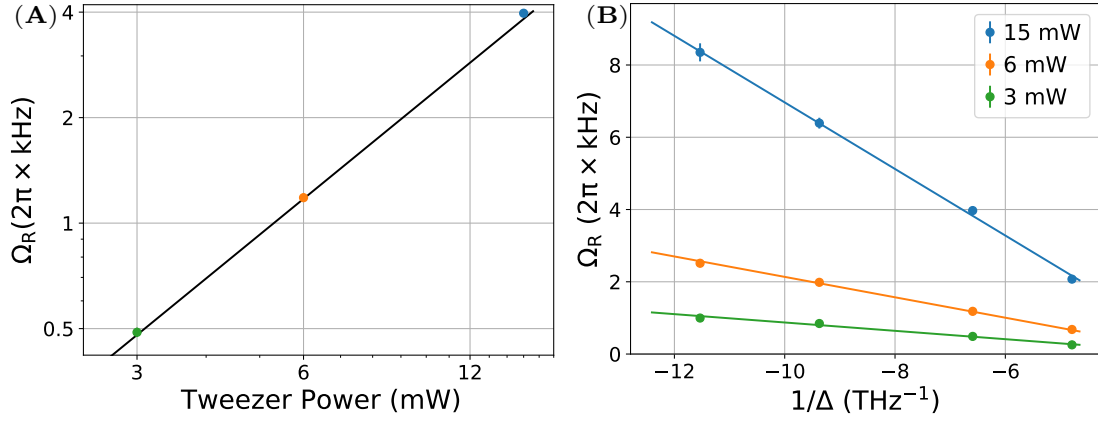
Figure 7.12: Fitting of Raman Rabi frequency Ω_R as a function of tweezer power and detuning. (A) Ω_R varies approximately with $P^{1.29}$. (B) Ω_R is proportional to $1/\Delta$ as expected from theory prediction. The detuning is calculated using the f_{PA0} from the light shift fitting in table 7.2

following model,

$$\Omega_R = \left(a + \frac{b}{f_{PA0} - f_{twr}} \right) \cdot P^{1.29} \tag{7.6}$$

where a and b are the coefficients for the background and the $v' = 0$ terms respectively. This is shown in Fig. 7.12B and the fitting parameters are shown in table 7.3 For the $v' = 0$ term, we have

$$b \cdot P^{1.29} = \frac{\Omega_1 \Omega_2}{2}$$

Combining with the previous measurement of the down-leg Rabi frequency, this gives an up-leg Rabi frequency of $2\pi \times 617.8(72)$ kHz/mW$^{0.79}$. The value for 15 mW tweezer

power is $2\pi \times 5.248(61)$ MHz for a Rabi frequency ratio Ω_2/Ω_1 of $66.90(79)$, which is close to the theory prediction of 77.7. Therefore, this should not cause the ratio of the Raman Rabi frequency to scattering rate from the $v' = 0$ state to be higher than expected. This ratio also verifies the assumption $\Omega_2^2 \gg \Omega_1^2$ made above for the light shift model. The background component fitted has the opposite sign with the $v' = 0$ term for a red detuned tweezer which reduces Ω_R by $\approx 35\ \%$ in Fig. 7.6B. The relative sign should change when the tweezer frequency is tuned to be higher than the excited molecular state resonance causing an increase in Ω_R. Unfortunately, we have observed another excited molecular state ≈ 200 GHz higher than $|e\rangle$ which increases the scattering and makes it difficult to drive a coherent transitions on the blue side.

Next we move on to the scattering rates. Based on the scaling of $P^{0.29}$ for the coupling between the atomic state and the excited molecular state, we expect the atomic scattering rate Γ_a to scale as $P^{1.58}$. However, as shown in Fig. 7.13, the scaling is very close to $P^{2.58}$ instead. This suggests that a two-photon scattering process is potentially involved. Furthermore, the plot also shows that the scattering rate does not depend strongly on the tweezer frequency meaning that almost all of the contributions are from other excited states or the laser noise. This scaling behavior is unexplained by our current theory. Nevertheless, as we will see soon, the absolute value of the scattering rate is much smaller than that from the molecular state and is therefore not limiting the transfer efficiency.
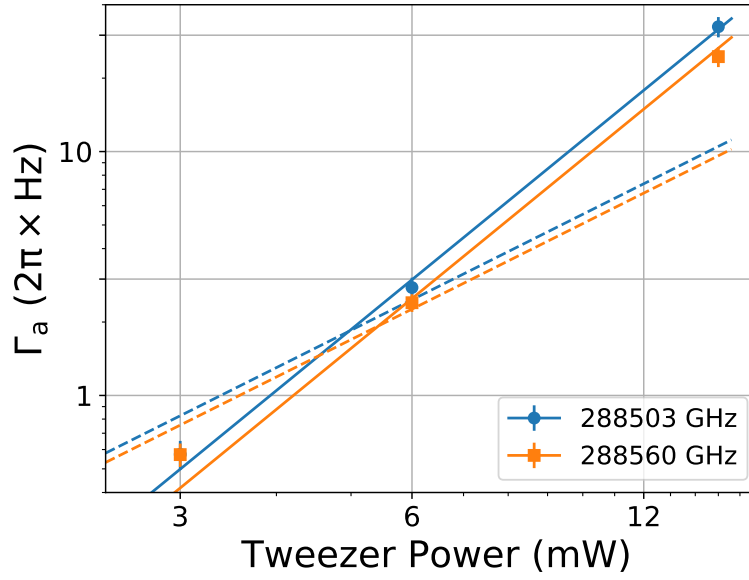
Figure 7.13: Dependence of atomic scattering rate Γ_a on tweezer power and frequency on a log-log scale. The dashed lines fit to $a \cdot P^{1.58}$ as expected from theory that has poor agreement with the data. The solid lines fit to $b \cdot P^{2.58}$ with much better agreement with data. The fitting results for tweezer frequencies of 288503 GHz and 288560 GHz are $b_{288503} = 2\pi \times 29.3(17)$ mHz/mW$^{2.58}$ and $b_{288560} = 2\pi \times 24.5(13)$ mHz/mW$^{2.58}$ respectively. The scaling behavior and the lack of sensitivity to tweezer frequency suggests that the scattering from the atomic state is dominated by other excited states or technical noise and is potentially a two-photon scattering process.
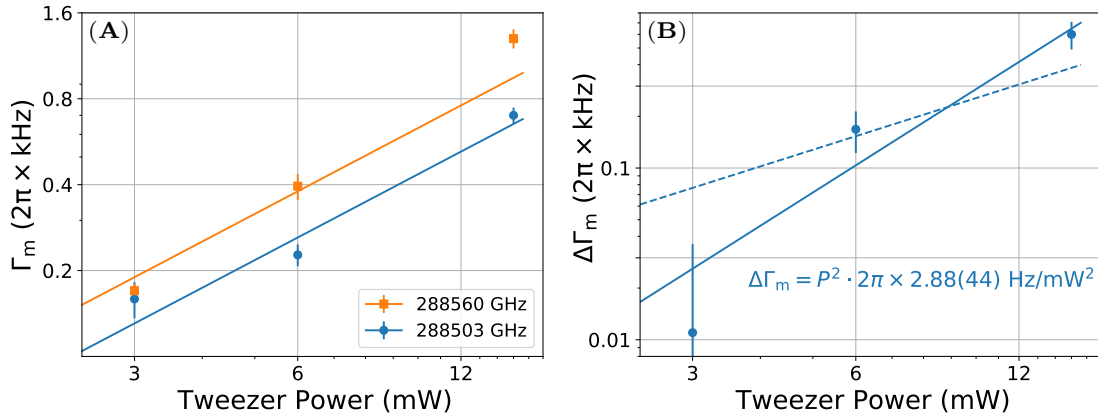
Figure 7.14: (A) Dependence of molecular scattering rate Γ_m on tweezer power and frequency on a log-log scale. The data fits to a linear model $a \cdot P$ better than the atomic scattering rate though the higher tweezer power points shows signature of a stronger power dependence. The fitting results for tweezer frequencies of 288503 GHz and 288560 GHz are $a_{288503} = 2\pi \times 43.5(21)$ Hz/mW and $a_{288560} = 2\pi \times 63.2(27)$ Hz/mW respectively. (B) The difference between the scattering rate for tweezer frequency at 288503 GHz and 288560 GHz. The result fits better to a P^2 model (solid line) than a P^1 model (dashed line) suggesting that there is potentially a two-photon process related to the $v' = 0$ excited molecular state. The fitting result for the P^2 model is shown on the plot.

Finally, we look at the molecular scattering rate Γ_m which is expected to scale proportionally to the tweezer power. This agrees with the experimental data better compared to the scattering on the atomic state, as shown in Fig. 7.14A. However, the points for higher tweezer power and smaller detuning deviates from the fit, suggesting that there could be multiple processes with different power scaling involved. The dependence on the tweezer frequency suggests that part of the scattering is related to the $v' = 0$ excited state[‡]. Although we do not measure at enough tweezer frequencies to allow a fit against detuning, we can take the difference between the two points we measured to study the dependence on

---

[‡]Note that part of the scattering is expected to be caused by the laser noise due to the decrease of scattering observed in section 7.5.1 after adding a second ASE filter after the fiber.

detuning and the effect from the $v' = 0$ state, as shown in Fig. 7.14B. The result shows a better agreement with P^2 scaling which could be caused by a two-photon scattering process. If we assume this two-photon process scales with $1/\Delta^{2\ddagger}$, the corresponding scattering rate for the condition in Fig. 7.9 is $\Gamma_m^{2-\text{photon}} = 2\pi \times 0.72(11)$ kHz or a Rabi oscillation coherence time of $0.441(67)$ ms. This is consistent with the measured value of $0.398(17)$ ms suggesting that the two-photon scattering could fully explain the observed excess scattering rate.

One possibility is for the two-photon process to couple to a state that is ≈ 577 THz or ≈ 519 nm above the atomic states. However, the molecular potential is not very well characterized at this energy range so we are unable to make any theory prediction about it. The other possibility, as discussed in section 5.3.3.3, is that it couples to an atomic continuum for a different hyperfine state combination. As shown in Fig. 5.10(B-F), in this case, the energies of the atomic continuum is between 210 MHz and 1.77 GHz which fully satisfies the approximations made to derive Eq. 5.3 and allows us to use it to compute the scattering rate. However, this coupling requires changes of m_F quantum number and therefore can only be caused by polarization impurity in the tweezer, which is difficult to measure accurately. We have measured this for a previous tweezer configuration based on the vector light shift of the tweezer that gives a $C = 0.0545(94)$ where $\mathbf{C}$ qualifies the ellipticity of the

---

$\ddagger$This is, of course, not a given. However, this is the case for the mechanism shown in Fig. 5.10(F), which we will estimate below.

polarization as defined in Eq. 5.2. We can roughly estimate the loss rate by assuming this polarization. After summing up the contribution from all the pathways in Fig. 5.10(F), we get a scattering rate of $\Gamma_m^{2-\text{photon}} = 2\pi \times 0.2\,\text{kHz}$. This agrees in order of magnitude with the observed loss and proves that this mechanism can indeed cause the observed scattering rate. Further verification and potential elimination of this requires changing the tweezer polarization and measuring the change in the scattering rate. This could also be done by changing the direction of the magnetic field.

7.6 Summary and Outlook

We demonstrated the coherent creation of a single molecule in the optical tweezer using only optical transitions and achieved control over all its degrees of freedoms. The technique we developed relies on fewer special properties of the system and can be generalized to associate more laser-coolable atoms into molecules. We calibrated the parameters of the Raman transition by measuring the dependence with tweezer power and detuning. The resulting Rabi frequencies match quite well with the theory prediction but the scattering rate we observe is much higher than expected. This undetermined scattering mechanism appears to be the limiting factor for the transfer efficiency in our experiment. We believe this could be caused by either technical sources or other processes involving the molecular excited state that are not accounted for. We discussed both possibilities based on our observations and

concluded that two likely sources of the scattering are the spectral noise of the laser and a two-photon process coupling the molecular state to an atomic state with lower hyperfine interaction energy. We raised questions and gave potential directions for further investigation.

Despite the limitation, the transfer efficiency may be further improved. This is especially true for the selection of the final state (section 7.4.3), which was mainly done based on technical considerations. As examples, states with larger binding energies can have weaker coupling to the excited states therefore reducing the ratio Ω_2/Ω_1 and the total scattering during the Raman transition. This may be a promising direction to explore but requires locking two lasers with a coherence time longer than a few milliseconds.

The creation of the weakly bound molecule in our experiment marks the first step towards a fully controlled array of interacting molecules. As the next step, the molecules will be transferred to the rovibronic ground state to enable strong dipole interactions, which has recently been achieved from Feshbach molecule in the optical tweezer in our experiment [145]. Combined with real-time rearrangement [74, 75], defect-free arrays of highly controlled molecules comprise a promising and flexible platform for quantum simulation and quantum computing applications.

A

Computer Control Hardware Specification

In this appendix we list the specifications of the important hardware used in our computer control system. See section 1.3 for the integration of these hardware into the system.

A.1 FPGA

We use the ZC702 evaluation board (part number EK-Z7-ZC702-G). The on board CPU has a maximum clock speed of 666.667 MHz and supports the VFPv3 and NEON extension for floating point and SIMD instructions. The board also includes 1 GiB of DDR3 RAM connected to the CPU. The FPGA is configured to run at 100 MHz which determines the highest timing resolution of 10 ns in our experiment.

We connect the FPGA to the peripherals using two FMC LPC connectors each containing 68 pins used for single-ended signals. Each FMC connector is used to control 11 DDS's, which will be described in section A.2, and one of the connector is also used to output 32 logical control signals and the clock signal to synchronize with other devices.

The DDS's on each FMC connector are controlled using a shared parallel bus with 7-bit address, 16-bit data and 6 control signals. A chip select pin for each DDS is used to enable the relevant one for update. The setup allows, in the general case, one DDS on each FMC connector to be programmed simultaneously while updating the logical outputs at the same time. This concurrent update capability, however, is not currently used in the experiment and only one update at a time is allowed.

A.2   DDS

The DDS we use is AD9914 from Analog Devices. The chip runs on an external clock of 3.5 GHz, which sets the sampling rate of 3.5 GS/s, and can directly output frequencies up to 1.4 GHz. The clock is shared between all the channels and can be provided by any source with sufficient power ($\approx$ 17 dBm). The sources that have been used in our experiment include MixNV from Windfreak Technologies and 5009 from Valon Technology, both being amplified by a ZX60-V82-S+ from Mini-Circuits. We configure the chip to use a single profile and output a fixed frequency and amplitude at any given time. Using the 16-bit data bus, the amplitude has a resolution of 12-bit, taking one 16-bit write or 160 ns to update, whereas the frequency has a resolution of 31-bit taking two 16-bit write or 240 ns to update[‡].

We use a ERA-4XSM+ gain block to amplify the signal from the DDS which gives a maximum power of 12 dBm at low frequencies ($\leqslant$ 100 MHz) and gradually decreases to 8 dBm around 1 GHz. We measure the noise on the output after the amplifier. We saw a low second harmonic power of $-40 \sim -50$ dBc over a wide frequency range of $80 \sim 900$ MHz. We also observed distortion when the output frequency is close to a fraction of the clock frequency but the effect is also relatively small (≈ -40 dBc). Finally, we

---

[‡]Currently we conservatively wait for a total of 500 ns before issuing the next command. However, it is likely that this wait time can be shortened.

measured the crosstalk between different channels. With a single channel outputing at maximum amplitude, we observed a $\approx -40 \sim -50$ dBc crosstalk between the channels. This is comparable to other noise on the output, though, the effect can be greater on a DDS outputting lower power. For this reason, we ensure the DDSs are outputting maximum power most of the time so that they are less susceptible to noise from other channels. For important noise sensitive channels, we also use additional methods including filtering, RF switches, light shutters (when the channel is driving an AOM) and offsetting the output frequencies from each other to minimize any crosstalk effects.

A.3 NI DAQ Board

We use a NI PCI-6733 analog output board connected to a BNC-2110 BNC connector block to generate low frequency voltage output. Other analog output boards that support trigger and external clock should also be supported. The board supports a sampling rate of 769 kS/s when using all output channels and we use 500 kS/s in the experiment. The output swing is -10 V to 10 V with a 16-bit resolution.

Unfortunately, different output channels on the board shares the same ground. This causes ground loop when connected to different devices, which significantly increases the noise on the output voltage. To fix this problem, a AD8429 instrumentation amplifier is used on each channel to isolate the output.

A.4 USRP

The USRP system we use has two parts, a motherboard, which is used to convert the data to analog signal, and a daughterboard, which can be used to further process the output. We use the USRP X310 motherboard which supports up to 200 MHz master clock frequency and a sampling rate of any integer fraction of the clock. We tested two different daughterboards.

1. UBX 160
   This daughterboard supports upshifting the output frequency by mixing with a local oscillator (LO) frequency. However, we observed strong leakage of the LO frequency and consequently high heating rate of the atom when using the output on the AOM controling the tweezer.

2. BasicTX
   This daughterboard directly outputs the signal from the motherboard without additional signal generation on board. Although we still see increased heating on the atom using this daughterboard compared to using the DDS output, the rate is lower than when using the UBX 160 daughterboard.

From the test results, we use the BasicTX daughterboard in the experiment for its lower noise and limit the use of the output to low frequency signals < 100 MHz. We use a sampling rate of 50 MS/s and a center frequency of 60 MHz. The maximum total power we get is around 10 dBm.

B

Full Raman Sideband Cooling Sequence

Each Raman pulse in the cooling sequence is followed immediately by an optical pumping pulse. The full parameters for the Raman pulses, including the cooling "axis", the sideband "order (Δn)", the cooling frequency "δ'", the carrier $(\Delta n = 0)$ frequency "δ'_0", the pulse "duration", the pulse strength in "Ω_0", and the beam on which a non-uniform "power ramp" is applied, are listed in 6 groups below. The applied cooling frequency, δ', is the two-

photon detuning given relative to the zero-field $F = 1$ and $F = 2$ hyperfine splitting of 1.7716261288(10) GHz [89]. Due to the Stark shifts of the Raman beams, the carrier transition, δ_0', varies with the power of the Raman beams. δ_0' is given also relative to the zero-field hyperfine splitting. The strength of the pulses given in Ω_0 determines the two-photon Rabi frequency, $\Omega_{n,\Delta n} = \Omega_0 \langle n | e^{i\vec{k}\cdot\vec{r}} | n + \Delta n \rangle$. We adopt the convention that a π-pulse between state n and $n + \Delta n$ requires a duration $\pi/\Omega_{n,\Delta n}$. The difference between δ' and δ_0' gives the motional sideband frequency, δ. Many Raman pulses include a "power ramp" with a Blackman envelope [108] to minimize off-resonant excitations. Because each Raman pulse is a product of two spatial- and temporal-overlapped laser beams, the "power ramp" is applied only to the beam that has the smaller light shift (we label the beam by the corresponding F number) while the other beam has a square-pulse shape. For a Raman pulse with a power ramp, the Rabi frequency gives the arithmetic mean over the duration of the pulse.

Group 1

This group is repeated 4 times.

Axis	Δn	δ' (MHz)	δ'_0 (MHz)	Duration (μs)	Ω_0 (kHz)	Power ramp
x	-2	19.625	18.649	44.1	$2\pi \times 23$	F1
y	-2	19.615	18.648	28.6	$2\pi \times 35$	F1
x	-1	19.130	18.649	36.9	$2\pi \times 23$	F1
y	-1	19.615	18.648	24.0	$2\pi \times 35$	F1

Group 2

This group is repeated 5 times.

Axis	Δn	δ' (MHz)	δ'_0 (MHz)	Duration (μs)	Ω_0 (kHz)	Power ramp
z	-5	19.030	18.605	81.5	$2\pi \times 16$	F2
x	-2	19.625	18.649	44.1	$2\pi \times 23$	F1
z	-4	18.940	18.605	76.3	$2\pi \times 16$	F2
y	-2	19.615	18.648	28.6	$2\pi \times 35$	F1
z	-5	19.030	18.605	81.5	$2\pi \times 16$	F2
x	-1	19.130	18.649	36.9	$2\pi \times 23$	F1
z	-4	18.940	18.605	76.3	$2\pi \times 16$	F2
y	-1	19.130	18.648	24.0	$2\pi \times 35$	F1

Group 3

This group is repeated 6 times.

Axis	Δn	δ' (MHz)	δ'_0 (MHz)	Duration (µs)	Ω_0 (kHz)	Power ramp
z	-4	18.940	18.605	76.3	$2\pi \times 16$	F2
x	-2	19.625	18.649	44.1	$2\pi \times 23$	F1
z	-3	18.858	18.605	70.2	$2\pi \times 16$	F2
y	-2	19.615	18.648	28.6	$2\pi \times 35$	F1
z	-4	18.940	18.605	76.3	$2\pi \times 16$	F2
x	-1	19.130	18.649	36.9	$2\pi \times 23$	F1
z	-3	18.858	18.605	70.2	$2\pi \times 16$	F2
y	-1	19.130	18.648	24.0	$2\pi \times 35$	F1

Group 4

This group is repeated 7 times.

Axis	Δn	δ' (MHz)	δ'_0 (MHz)	Duration (μs)	Ω_0 (kHz)	Power ramp
z	-3	18.858	18.605	70.2	$2\pi \times 16$	F2
x	-2	19.625	18.649	44.1	$2\pi \times 23$	F1
z	-2	18.773	18.605	62.7	$2\pi \times 16$	F2
y	-2	19.615	18.648	28.6	$2\pi \times 35$	F1
z	-3	18.858	18.605	70.2	$2\pi \times 16$	F2
x	-1	19.130	18.649	36.9	$2\pi \times 23$	F1
z	-2	18.773	18.605	62.7	$2\pi \times 16$	F2
y	-1	19.130	18.648	24.0	$2\pi \times 35$	F1

Group 5

This group is repeated 10 times.

Axis	Δn	δ^{γ} (MHz)	δ^{γ}_0 (MHz)	Duration (µs)	Ω_0 (kHz)	Power ramp
z	-2	18.773	18.605	62.7	$2\pi \times 16$	F2
x	-1	19.130	18.649	36.9	$2\pi \times 23$	F1
z	-1	18.685	18.605	52.5	$2\pi \times 16$	F2
y	-1	19.130	18.648	24.0	$2\pi \times 35$	F1
z	-2	18.773	18.605	62.7	$2\pi \times 16$	F2
x	-1	19.130	18.649	70.0	$2\pi \times 23$	F1
z	-1	18.685	18.605	52.5	$2\pi \times 16$	F2
y	-1	19.130	18.648	46.0	$2\pi \times 35$	F1

Group 6

This group is repeated 30 times.

Axis	Δn	δ' (MHz)	δ'_0 (MHz)	Duration (μs)	Ω_0 (kHz)	Power ramp
z	-1	18.683	18.605	78.7	$2\pi \times 11$	F2
z	-1	18.683	18.605	135.0	$2\pi \times 11$	F2
z	-1	18.685	18.605	78.7	$2\pi \times 11$	F2
x	-1	19.130	18.649	36.9	$2\pi \times 23$	F1
y	-1	19.130	18.648	24.0	$2\pi \times 35$	F1
z	-1	18.685	18.605	78.7	$2\pi \times 11$	F2
z	-1	18.685	18.605	135.0	$2\pi \times 11$	F2
z	-1	18.685	18.605	78.7	$2\pi \times 11$	F2
x	-1	19.130	18.649	70.0	$2\pi \times 23$	F1
y	-1	19.130	18.648	46.0	$2\pi \times 35$	F1

References

[1] Y. Wang, A. Kumar, T.-Y. Wu, and D. S. Weiss, "Single-Qubit Gates Based on Targeted Phase Shifts in a 3D Neutral Atom Array," Science **352**(6293), 1562–1565 (2016).

[2] M. Anderlini, P. J. Lee, B. L. Brown, J. Sebby-Strabley, W. D. Phillips, and J. V. Porto, "Controlled Exchange Interaction between Pairs of Neutral Atoms in an Optical Lattice," Nature **448**(7152), 452–456 (2007).

[3] A. M. Kaufman, B. J. Lester, M. Foss-Feig, M. L. Wall, A. M. Rey, and C. A. Regal, "Entangling Two Transportable Neutral Atoms via Local Spin Exchange," Nature **527**(7577), 208–211 (2015).

[4] H. Levine, A. Keesling, A. Omran, H. Bernien, S. Schwartz, A. S. Zibrov, M. Endres, M. Greiner, V. Vuletić, and M. D. Lukin, "High-Fidelity Control and Entanglement of Rydberg-Atom Qubits," Physical Review Letters **121**(12), 123,603 (2018).

[5] L. Isenhower, E. Urban, X. L. Zhang, A. T. Gill, T. Henage, T. A. Johnson, T. G. Walker, and M. Saffman, "Demonstration of a Neutral Atom Controlled-NOT Quantum Gate," Physical Review Letters **104**(1), 010,503 (2010).

[6] T. G. Tiecke, J. D. Thompson, N. P. de Leon, L. R. Liu, V. Vuletić, and M. D. Lukin, "Nanophotonic Quantum Phase Switch with a Single Atom," Nature **508**(7495), 241–244 (2014).

[7] A. Reiserer, N. Kalb, G. Rempe, and S. Ritter, "A Quantum Gate between a Flying Optical Photon and a Single Trapped Atom," Nature **508**(7495), 237–240 (2014).

[8] S. Welte, B. Hacker, S. Daiss, S. Ritter, and G. Rempe, "Photon-Mediated Quantum Gate between Two Neutral Atoms in an Optical Cavity," Physical Review X **8**(1), 011,018 (2018).

[9] B. J. Bloom, T. L. Nicholson, J. R. Williams, S. L. Campbell, M. Bishof, X. Zhang, W. Zhang, S. L. Bromley, and J. Ye, "An optical lattice clock with accuracy and stability at the 10^{-18} level," Nature **506**(7486), 71–75 (2014).

[10] R. H. Parker, C. Yu, W. Zhong, B. Estey, and H. Müller, "Measurement of the Fine-Structure Constant as a Test of the Standard Model," Science **360**(6385), 191–195 (2018).

[11] W. S. Bakr, J. I. Gillen, A. Peng, S. Fölling, and M. Greiner, "A Quantum Gas Microscope for Detecting Single Atoms in a Hubbard-Regime Optical Lattice," Nature **462**(7269), 74–77 (2009).

[12] L. W. Cheuk, M. A. Nichols, M. Okan, T. Gersdorf, V. V. Ramasesh, W. S. Bakr, T. Lompe, and M. W. Zwierlein, "Quantum-Gas Microscope for Fermionic Atoms," Physical Review Letters **114**(19), 193,001 (2015).

[13] H. Bernien, S. Schwartz, A. Keesling, H. Levine, A. Omran, H. Pichler, S. Choi, A. S. Zibrov, M. Endres, M. Greiner, V. Vuletić, and M. D. Lukin, "Probing Many-Body Dynamics on a 51-Atom Quantum Simulator," Nature **551**(7682), 579–584 (2017).

[14] S. de Léséleuc, V. Lienhard, P. Scholl, D. Barredo, S. Weber, N. Lang, H. P. Büchler, T. Lahaye, and A. Browaeys, "Observation of a Symmetry-Protected Topological Phase of Interacting Bosons with Rydberg Atoms," Science **365**(6455), 775–780 (2019). 1810.13286.

[15] J. Koepsell, J. Vijayan, P. Sompet, F. Grusdt, T. A. Hilker, E. Demler, G. Salomon, I. Bloch, and C. Gross, "Imaging Magnetic Polarons in the Doped Fermi-Hubbard Model," Nature **572**(7769), 358–362 (2019).

[16] C. S. Chiu, G. Ji, A. Bohrdt, M. Xu, M. Knap, E. Demler, F. Grusdt, M. Greiner, and D. Greif, "String Patterns in the Doped Hubbard Model," Science **365**(6450), 251–256 (2019).

[17] I. Bloch, J. Dalibard, and W. Zwerger, "Many-Body Physics with Ultracold Gases," Reviews of Modern Physics **80**(3), 885–964 (2008).

[18] T. Lahaye, C. Menotti, L. Santos, M. Lewenstein, and T. Pfau, "The Physics of Dipolar Bosonic Quantum Gases," Reports on Progress in Physics **72**(12), 126,401 (2009).

[19] J. Weiner, V. S. Bagnato, S. Zilio, and P. S. Julienne, "Experiments and Theory in Cold and Ultracold Collisions," Reviews of Modern Physics **71**(1), 1–85 (1999).

[20] P. Sompet, S. S. Szigeti, E. Schwartz, A. S. Bradley, and M. F. Andersen, "Thermally robust spin correlations between two ^{85}Rb atoms in an optical microtrap," Nature Communications **10**(1), 1889 (2019).

[21] P. Xu, J. Yang, M. Liu, X. He, Y. Zeng, K. Wang, J. Wang, D. J. Papoular, G. V. Shlyapnikov, and M. Zhan, "Interaction-Induced Decay of a Heteronuclear Two-Atom System," Nature Communications **6**(1), 7803 (2015).

[22] Q. Guan, V. Klinkhamer, R. Klemt, J. H. Becher, A. Bergschneider, P. M. Preiss, S. Jochim, and D. Blume, "Density Oscillations Induced by Individual Ultracold Two-Body Collisions," Physical Review Letters **122**(8), 083,401 (2019).

[23] I. Dimitrova, W. Lunden, J. Amato-Grill, N. Jepsen, Y. Yu, M. Messer, T. Rigaldo, G. Puentes, D. Weld, and W. Ketterle, "Observation of Two-Beam Collective Scattering Phenomena in a Bose-Einstein Condensate," Physical Review A **96**(5), 051,603 (2017).

[24] S. Bickman, P. Hamilton, Y. Jiang, and D. DeMille, "Preparation and Detection of States with Simultaneous Spin Alignment and Selectable Molecular Orientation in PbO," Physical Review A **80**(2), 023,418 (2009).

[25] J. J. Hudson, D. M. Kara, I. J. Smallman, B. E. Sauer, M. R. Tarbutt, and E. A. Hinds, "Improved Measurement of the Shape of the Electron," Nature **473**(7348), 493–496 (2011).

[26] S. Eckel, P. Hamilton, E. Kirilov, H. W. Smith, and D. DeMille, "Search for the electron electric dipole moment using Ω-doublet levels in PbO," Physical Review A **87**(5), 052,130 (2013).

[27] I. Kozyryev and N. R. Hutzler, "Precision Measurement of Time-Reversal Symmetry Violation with Laser-Cooled Polyatomic Molecules," Physical Review Letters **119**(13), 133,002 (2017).

[28] W. B. Cairncross, D. N. Gresh, M. Grau, K. C. Cossel, T. S. Roussy, Y. Ni, Y. Zhou, J. Ye, and E. A. Cornell, "Precision Measurement of the Electron's Electric Dipole Moment Using Trapped Molecular Ions," Physical Review Letters **119**(15), 153,001 (2017).

[29] ACME Collaboration, V. Andreev, D. G. Ang, D. DeMille, J. M. Doyle, G. Gabrielse, J. Haefner, N. R. Hutzler, Z. Lasner, C. Meisenhelder, B. R. O'Leary, C. D. Panda, A. D. West, E. P. West, and X. Wu, "Improved Limit on the Electric Dipole Moment of the Electron," Nature **562**(7727), 355–360 (2018).

[30] S. S. Kondov, C.-H. Lee, K. H. Leung, C. Liedl, I. Majewska, R. Moszynski, and T. Zelevinsky, "Molecular Lattice Clock with Long Vibrational Coherence," Nature Physics **15**(11), 1118–1122 (2019).

[31] V. V. Flambaum and V. A. Dzuba, "Electric Dipole Moments of Atoms and Molecules Produced by Enhanced Nuclear Schiff Moments," Physical Review A **101**(4), 042,504 (2020).

[32] A. Micheli, G. K. Brennen, and P. Zoller, "A Toolbox for Lattice-Spin Models with Polar Molecules," Nature Physics **2**(5), 341 (2006).

[33] H. P. Büchler, E. Demler, M. Lukin, A. Micheli, N. Prokof'ev, G. Pupillo, and P. Zoller, "Strongly Correlated 2D Quantum Phases with Cold Polar Molecules: Controlling the Shape of the Interaction Potential," Physical Review Letters **98**(6), 060,404 (2007).

[34] A. V. Gorshkov, S. R. Manmana, G. Chen, J. Ye, E. Demler, M. D. Lukin, and A. M. Rey, "Tunable Superfluidity and Quantum Magnetism with Ultracold Polar Molecules," Physical Review Letters **107**(11), 115,301 (2011).

[35] M. A. Baranov, M. Dalmonte, G. Pupillo, and P. Zoller, "Condensed Matter Theory of Dipolar Quantum Gases," Chemical Reviews **112**(9), 5012–5061 (2012).

[36] N. Y. Yao, A. V. Gorshkov, C. R. Laumann, A. M. Läuchli, J. Ye, and M. D. Lukin, "Realizing Fractional Chern Insulators in Dipolar Spin Systems," Physical Review Letters **110**(18), 185,302 (2013).

[37] S. V. Syzranov, M. L. Wall, V. Gurarie, and A. M. Rey, "Spin-Orbital Dynamics in a System of Polar Molecules," Nature Communications **5**(1), 5391 (2014).

[38] M. L. Wall, K. R. A. Hazzard, and A. M. Rey, "Quantum Magnetism with Ultracold Molecules," in *From Atomic to Mesoscale: The Role of Quantum Coherence in Systems of Various Complexities*, S. Malinovskaya and I. Novikova, eds. (World Scientific, 2015).

[39] M. L. Wall, K. Maeda, and L. D. Carr, "Realizing Unconventional Quantum Magnetism with Symmetric Top Molecules," New Journal of Physics **17**(2), 025,001 (2015).

[40] D. Peter, N. Y. Yao, N. Lang, S. D. Huber, M. D. Lukin, and H. P. Büchler, "Topological bands with a Chern number $C = 2$ by dipolar exchange interactions," Physical Review A **91**(5), 053,617 (2015).

[41] N. Y. Yao, M. P. Zaletel, D. M. Stamper-Kurn, and A. Vishwanath, "A Quantum Dipolar Spin Liquid," Nature Physics **14**(4), 405–410 (2018).

[42] B. Sundar, B. Gadway, and K. R. A. Hazzard, "Synthetic Dimensions in Ultracold Polar Molecules," Scientific Reports **8**(1), 3422 (2018). 1708.02112.

[43] T. Schuster, F. Flicker, M. Li, S. Kotochigova, J. E. Moore, J. Ye, and N. Y. Yao, "Realizing Hopf Insulators in Dipolar Spin Systems," arXiv:1901.08597 [cond-mat, physics:quant-ph] (2019). 1901.08597.

[44] D. DeMille, "Quantum Computation with Trapped Polar Molecules," Physical Review Letters **88**(6), 67,901 (2002).

[45] K.-K. Ni, T. Rosenband, and D. D. Grimes, "Dipolar Exchange Quantum Logic Gate with Polar Molecules," Chemical Science **9**(33), 6830–6838 (2018).

[46] E. R. Hudson and W. C. Campbell, "Dipolar Quantum Logic for Freely Rotating Trapped Molecular Ions," Physical Review A **98**(4), 040,302 (2018).

[47] Y. Lin, D. R. Leibrandt, D. Leibfried, and C.-w. Chou, "Quantum Entanglement between an Atom and a Molecule," Nature **581**(7808), 273–277 (2020).

[48] N. Balakrishnan, "Perspective: Ultracold Molecules and the Dawn of Cold Controlled Chemistry," The Journal of Chemical Physics **145**(15), 150,901 (2016).

[49] M.-G. Hu, Y. Liu, D. D. Grimes, Y.-W. Lin, A. H. Gheorghe, R. Vexiau, N. Bouloufa-Maafa, O. Dulieu, T. Rosenband, and K.-K. Ni, "Direct Observation of Bimolecular Reactions of Ultracold KRb Molecules," Science **366**(6469), 1111–1115 (2019).

[50] Y. Segev, M. Pitzer, M. Karpov, N. Akerman, J. Narevicius, and E. Narevicius, "Collisions between Cold Molecules in a Superconducting Magnetic Trap," Nature **572**(7768), 189–193 (2019).

[51] T. de Jongh, M. Besemer, Q. Shuai, T. Karman, A. van der Avoird, G. C. Groenenboom, and S. Y. T. van de Meerakker, "Imaging the Onset of the Resonance Regime in Low-Energy NO-He Collisions," Science **368**(6491), 626–630 (2020).

[52] D. A. Fedorov, A. Derevianko, and S. A. Varganov, "Accurate Potential Energy, Dipole Moment Curves, and Lifetimes of Vibrational States of Heteronuclear Alkali Dimers," The Journal of Chemical Physics **140**(18), 184,315 (2014).

[53] S. Giovanazzi, A. Görlitz, and T. Pfau, "Tuning the Dipolar Interaction in Quantum Gases," Physical Review Letters **89**(13), 130,401 (2002).

[54] J. F. Barry, D. J. McCarron, E. B. Norrgard, M. H. Steinecker, and D. DeMille, "Magneto-Optical Trapping of a Diatomic Molecule," Nature **512**(7514), 286–289 (2014).

[55] E. B. Norrgard, D. J. McCarron, M. H. Steinecker, M. R. Tarbutt, and D. DeMille, "Submillikelvin Dipolar Molecules in a Radio-Frequency Magneto-Optical Trap," Physical Review Letters **116**(6), 1–6 (2016).

[56] S. Truppe, H. J. Williams, M. Hambach, L. Caldwell, N. J. Fitch, E. A. Hinds, B. E. Sauer, and M. R. Tarbutt, "Molecules Cooled below the Doppler Limit," Nature Physics **13**(12), 1173–1176 (2017).

[57] L. Anderegg, B. L. Augenbraun, Y. Bao, S. Burchesky, L. W. Cheuk, W. Ketterle, and J. M. Doyle, "Laser Cooling of Optically Trapped Molecules," Nature Physics **14**(9), 890–893 (2018).

[58] D. J. McCarron, M. H. Steinecker, Y. Zhu, and D. DeMille, "Magnetic Trapping of an Ultracold Gas of Polar Molecules," Physical Review Letters **121**(1), 013,202 (2018).

[59] A. L. Collopy, S. Ding, Y. Wu, I. A. Finneran, L. Anderegg, B. L. Augenbraun, J. M. Doyle, and J. Ye, "3D Magneto-Optical Trap of Yttrium Monoxide," Physical Review Letters **121**(21), 213,201 (2018).

[60] D. Mitra, N. B. Vilas, C. Hallas, L. Anderegg, B. L. Augenbraun, L. Baum, C. Miller, S. Raval, and J. M. Doyle, "Direct Laser Cooling of a Symmetric Top Molecule," Science **369**(6509), 1366–1369 (2020).

[61] S. Ding, Y. Wu, I. A. Finneran, J. J. Burau, and J. Ye, "Sub-Doppler Cooling and Compressed Trapping of YO Molecules at µK Temperatures," Physical Review X **10**(2), 021,049 (2020).

[62] L. W. Cheuk, L. Anderegg, B. L. Augenbraun, Y. Bao, S. Burchesky, W. Ketterle, and J. M. Doyle, "Λ-Enhanced Imaging of Molecules in an Optical Trap," Physical Review Letters **121**(8), 083,201 (2018).

[63] L. Anderegg, L. W. Cheuk, Y. Bao, S. Burchesky, W. Ketterle, K.-K. Ni, and J. M. Doyle, "An Optical Tweezer Array of Ultracold Molecules," Science **365**(6458), 1156–1158 (2019).

[64] K.-K. Ni, S. Ospelkaus, M. H. G. de Miranda, A. Pe'er, B. Neyenhuis, J. J. Zirbel, S. Kotochigova, P. S. Julienne, D. S. Jin, and J. Ye, "A High Phase-Space-Density Gas of Polar Molecules," Science **322**(5899), 231–235 (2008).

[65] F. Lang, "Ultracold Triplet Molecules in the Rovibrational Ground State," Physical Review Letters **101**(13) (2008).

[66] L. D. Marco, G. Valtolina, K. Matsuda, W. G. Tobias, J. P. Covey, and J. Ye, "A Degenerate Fermi Gas of Polar Molecules," Science **363**(6429), 853–856 (2019).

[67] J. T. Zhang, Y. Yu, W. B. Cairncross, K. Wang, L. R. B. Picard, J. D. Hood, Y.-W. Lin, J. M. Hutson, and K.-K. Ni, "Forming a Single Molecule by Magnetoassociation in an Optical Tweezer," Physical Review Letters **124**(25), 253,401 (2020). 2003.07850.

[68] X. He, K. Wang, J. Zhuang, P. Xu, X. Gao, R. Guo, C. Sheng, M. Liu, J. Wang, J. Li, G. V. Shlyapnikov, and M. Zhan, "Coherently Forming a Single Molecule in an Optical Trap," Science **370**(6514), 331–335 (2020).

[69] S. A. Moses, J. P. Covey, M. T. Miecnikowski, B. Yan, B. Gadway, J. Ye, and D. S. Jin, "Creation of a Low-Entropy Quantum Gas of Polar Molecules in an Optical Lattice," Science **350**(6261), 659–662 (2015).

[70] M. Mayle, G. Quéméner, B. P. Ruzic, and J. L. Bohn, "Scattering of Ultracold Molecules in the Highly Resonant Regime," Physical Review A **87**(1), 1–8 (2013).

[71] J. F. E. Croft and J. L. Bohn, "Long-Lived Complexes and Chaos in Ultracold Molecular Collisions," Physical Review A **89**(1), 012,714 (2014).

[72] Y. Liu, M.-G. Hu, M. A. Nichols, D. D. Grimes, T. Karman, H. Guo, and K.-K. Ni, "Photo-Excitation of Long-Lived Transient Intermediates in Ultracold Reactions," Nature Physics **16**(11), 1132–1136 (2020).

[73] N. Schlosser, G. Reymond, I. Protsenko, and P. Grangier, "Sub-Poissonian Loading of Single Atoms in a Microscopic Dipole Trap," Nature **411**(6841), 1024–1027 (2001).

[74] D. Barredo, S. de Léséleuc, V. Lienhard, T. Lahaye, and A. Browaeys, "An Atom-by-Atom Assembler of Defect-Free Arbitrary Two-Dimensional Atomic Arrays," Science **354**(6315), 1021–1023 (2016).

[75] M. Endres, H. Bernien, A. Keesling, H. Levine, E. R. Anschuetz, A. Krajenbrink, C. Senko, V. Vuletic, M. Greiner, and M. D. Lukin, "Atom-by-Atom Assembly of Defect-Free One-Dimensional Cold Atom Arrays," Science $\mathbf{354}$(6315), 1024–1027 (2016).

[76] J. G. Danzl, E. Haller, M. Gustavsson, M. J. Mark, R. Hart, N. Bouloufa, O. Dulieu, H. Ritsch, and H.-C. Nägerl, "Quantum Gas of Deeply Bound Ground State Molecules," Science $\mathbf{321}$(5892), 1062–1066 (2008).

[77] T. Takekoshi, L. Reichsöllner, A. Schindewolf, J. M. Hutson, C. R. Le Sueur, O. Dulieu, F. Ferlaino, R. Grimm, and H.-C. Nägerl, "Ultracold Dense Samples of Dipolar RbCs Molecules in the Rovibrational and Hyperfine Ground State," Physical Review Letters $\mathbf{113}$(20), 205,301 (2014).

[78] P. K. Molony, P. D. Gregory, Z. Ji, B. Lu, M. P. Köppinger, C. R. Le Sueur, C. L. Blackley, J. M. Hutson, and S. L. Cornish, "Creation of Ultracold ^{87}Rb^{133}Cs Molecules in the Rovibrational Ground State," Physical Review Letters $\mathbf{113}$(25), 255,301 (2014).

[79] J. W. Park, S. A. Will, and M. W. Zwierlein, "Ultracold Dipolar Gas of Fermionic ^{23}Na^{40}K Molecules in Their Absolute Ground State," Physical Review Letters $\mathbf{205302}$(May), 1–5 (2015).

[80] M. Guo, B. Zhu, B. Lu, X. Ye, F. Wang, R. Vexiau, N. Bouloufa-Maafa, G. Quéméner, O. Dulieu, and D. Wang, "Creation of an Ultracold Gas of Ground-State Dipolar ^{23}Na^{87}Rb Molecules," Physical Review Letters $\mathbf{116}$(20), 205,303 (2016).

[81] T. M. Rvachov, H. Son, A. T. Sommer, S. Ebadi, J. J. Park, M. W. Zwierlein, W. Ketterle, and A. O. Jamison, "Long-Lived Ultracold Molecules with Electric and Magnetic Dipole Moments," Physical Review Letters $\mathbf{119}$(14), 143,001 (2017).

[82] K. K. Voges, P. Gersema, M. Meyer zum Alten Borgloh, T. A. Schulze, T. Hartmann, A. Zenesini, and S. Ospelkaus, "Ultracold Gas of Bosonic ^{23}Na^{39}K Ground-State Molecules," Physical Review Letters $\mathbf{125}$(8), 083,401 (2020). 2008.05439.

[83] G. Reinaudi, C. B. Osborn, M. McDonald, S. Kotochigova, and T. Zelevinsky, "Optical Production of Stable Ultracold ^{88}Sr$_2$ Molecules," Physical Review Letters **109**(11), 115,303 (2012).

[84] S. Stellmer, B. Pasquiou, R. Grimm, and F. Schreck, "Creation of Ultracold Sr$_2$ Molecules in the Electronic Ground State," Physical Review Letters **109**(11), 115,302 (2012).

[85] P. J. Dagdigian and L. Wharton, "Molecular Beam Electric Deflection and Resonance Spectroscopy of the Heteronuclear Alkali Dimers: ^{39}K^{7}Li, Rb^{7}Li, ^{39}K^{23}Na, Rb^{23}Na, and ^{133}Cs^{23}Na," The Journal of Chemical Physics **57**(4), 1487–1496 (1972).

[86] J. Deiglmayr, M. Aymar, R. Wester, M. Weidemüller, and O. Dulieu, "Calculations of Static Dipole Polarizabilities of Alkali Dimers: Prospects for Alignment of Ultracold Molecules," The Journal of Chemical Physics **129**(6), 064,309 (2008).

[87] K. Bergmann, H. Theuer, and B. W. Shore, "Coherent Population Transfer among Quantum States of Atoms and Molecules," Reviews of Modern Physics **70**(3), 1003–1025 (1998).

[88] L. R. Liu, "Building Single Molecules - Reactions, Collisions, and Spectroscopy of Two Atoms," Ph.D., Harvard University, Cambridge (2019).

[89] D. A. Steck, "Sodium D Line Data," (2019).

[90] D. A. Steck, "Cesium D Line Data," (2019).

[91] N. R. Hutzler, L. R. Liu, Y. Yu, and K.-K. Ni, "Eliminating Light Shifts for Single Atom Trapping," New Journal of Physics **19**(2), 023,007 (2017).

[92] ISO/TC 172/SC 9, "ISO 11146-1:2005(En), Lasers and Laser-Related Equipment — Test Methods for Laser Beam Widths, Divergence Angles and Beam Propagation Ratios — Part 1: Stigmatic and Simple Astigmatic Beams," Tech. rep., ISO (2005).

[93] DataRay Inc., "WinCamD User Manual," (2018).

[94] F. Diedrich, J. C. Bergquist, W. M. Itano, and D. J. Wineland, "Laser Cooling to the Zero-Point Energy of Motion," Physical Review Letters **62**(4), 403–406 (1989).

[95] D. J. Heinzen, "Quantum-Limited Cooling and Detection of Radio-Frequency Oscillations by Laser-Cooled Ions," Physical Review A **42**(5), 2977–2994 (1990).

[96] C. Monroe, D. M. Meekhof, B. E. King, S. R. Jefferts, W. M. Itano, D. J. Wineland, and P. Gould, "Resolved-Sideband Raman Cooling of a Bound Atom to the 3D Zero-Point Energy," Physical Review Letters **75**(22), 4011–4014 (1995).

[97] A. J. Kerman, V. Vuletić, C. Chin, and S. Chu, "Beyond Optical Molasses: 3D Raman Sideband Cooling of Atomic Cesium to High Phase-Space Density," Physical Review Letters **84**(3), 439–442 (2000).

[98] D.-J. Han, S. Wolf, S. Oliver, C. McCormick, M. T. DePue, and D. S. Weiss, "3D Raman Sideband Cooling of Cesium Atoms at High Density," Physical Review Letters **85**(4), 724–727 (2000).

[99] L. R. Liu, J. D. Hood, Y. Yu, J. T. Zhang, K. Wang, Y.-W. Lin, T. Rosenband, and K.-K. Ni, "Molecular Assembly of Ground State Cooled Single Atoms," Physical Review X **9**(2), 021,039 (2019). 1902.03935.

[100] Y. Yu, N. R. Hutzler, J. T. Zhang, L. R. Liu, J. D. Hood, T. Rosenband, and K.-K. Ni, "Motional-Ground-State Cooling Outside the Lamb-Dicke Regime," Physical Review A **97**(6), 063,423 (2018). 1708.03296.

[101] P. L. Knight, E. A. Hinds, M. B. Plenio, D. J. Wineland, M. Barrett, J. Britton, J. Chiaverini, B. DeMarco, W. M. Itano, B. Jelenković, C. Langer, D. Leibfried, V. Meyer, T. Rosenband, and T. Schätz, "Quantum Information Processing with Trapped Ions," Philosophical Transactions of the Royal Society of London. Series A: Mathematical, Physical and Engineering Sciences **361**(1808), 1349–1361 (2003).

[102] D. Wineland, C. Monroe, W. Itano, D. Leibfried, B. King, and D. Meekhof, "Experimental Issues in Coherent Quantum-State Manipulation of Trapped Atomic Ions," J. Res. Natl. Inst. Stand. Technol. **103**(3), 259 (1998).

[103] M. Gröbner, P. Weinmann, E. Kirilov, and H.-C. Nägerl, "Degenerate Raman side-band cooling of ^{39}K," Physical Review A **95**(3), 033,412 (2017).

[104] D. M. Meekhof, C. Monroe, B. E. King, W. M. Itano, and D. J. Wineland, "Generation of Nonclassical Motional States of a Trapped Atom," Physical Review Letters **76**(11), 1796–1799 (1996).

[105] A. M. Kaufman, B. J. Lester, and C. A. Regal, "Cooling a Single Atom in an Optical Tweezer to Its Quantum Ground State," Physical Review X **2**(4), 041,014 (2012).

[106] J. D. Thompson, T. G. Tiecke, A. S. Zibrov, V. Vuletić, and M. D. Lukin, "Coherence and Raman Sideband Cooling of a Single Atom in an Optical Tweezer," Physical Review Letters **110**(13), 133,001 (2013). 1209.3028.

[107] D. J. Wineland and W. M. Itano, "Laser Cooling of Atoms," Physical Review A **20**(4), 1521–1540 (1979).

[108] M. Kasevich and S. Chu, "Laser Cooling below a Photon Recoil with Three-Level Atoms," Physical Review Letters **69**(12), 1741–1744 (1992).

[109] J. Dalibard, Y. Castin, and K. Mølmer, "Wave-Function Approach to Dissipative Processes in Quantum Optics," Physical Review Letters **68**(5), 580–583 (1992).

[110] R. Chrétien, "Laser Cooling of Atoms : Monte-Carlo Wavefunction Simulations," Master's thesis, University of Liège, Belgium (2014).

[111] R. Fu and G. Bodenhausen, "Broadband Decoupling in NMR with Frequency-Modulated 'Chirp' Pulses," Chemical Physics Letters **245**(4), 415–420 (1995).

[112] R. Grimm, M. Weidemüller, and Y. B. Ovchinnikov, "Optical Dipole Traps for Neutral Atoms," Adv. At. Mol. Opt. Phys. **42**, 95–170 (2000).

[113] G. Colzi, G. Durastante, E. Fava, S. Serafini, G. Lamporesi, and G. Ferrari, "Sub-Doppler Cooling of Sodium Atoms in Gray Molasses," Physical Review A **93**(2), 1–6 (2016).

[114] C. Ospelkaus, S. Ospelkaus, L. Humbert, P. Ernst, K. Sengstock, and K. Bongs, "Ultracold Heteronuclear Molecules in a 3D Optical Lattice," Physical Review Letters **97**(12), 2–5 (2006).

[115] J. G. Danzl, M. J. Mark, E. Haller, M. Gustavsson, R. Hart, J. Aldegunde, J. M. Hutson, and H.-C. Nägerl, "An Ultracold High-Density Sample of Rovibronic Ground-State Molecules in an Optical Lattice," Nature Physics **6**(4), 265–270 (2010).

[116] J. P. Covey, S. A. Moses, M. Gärttner, A. Safavi-Naini, M. T. Miecnikowski, Z. Fu, J. Schachenmayer, P. S. Julienne, A. M. Rey, D. S. Jin, and J. Ye, "Doublon Dynamics and Polar Molecule Production in an Optical Lattice," Nature Communications **7**(1), 11,279 (2016).

[117] A. Goban, R. B. Hutson, G. E. Marti, S. L. Campbell, M. A. Perlin, P. S. Julienne, J. P. D'Incao, A. M. Rey, and J. Ye, "Emergence of Multi-Body Interactions in a Fermionic Lattice Clock," Nature **563**(7731), 369–373 (2018).

[118] J. Amato-Grill, N. Jepsen, I. Dimitrova, W. Lunden, and W. Ketterle, "Interaction Spectroscopy of a Two-Component Mott Insulator," Physical Review A **99**(3), 033,612 (2019).

[119] J. D. Hood, Y. Yu, Y.-W. Lin, J. T. Zhang, K. Wang, L. R. Liu, B. Gao, and K.-K. Ni, "Multichannel Interactions of Two Atoms in an Optical Tweezer," Physical Review Research **2**(2), 023,108 (2020).

[120] T. Busch, B.-G. Englert, K. Rza\.zewski, and M. Wilkens, "Two Cold Atoms in a Harmonic Trap," Found. Phys. **28**(4), 549–559 (1998).

[121] E. L. Bolda, E. Tiesinga, and P. S. Julienne, "Effective-Scattering-Length Model of Ultracold Atomic Collisions and Feshbach Resonances in Tight Harmonic Traps," Physical Review A **66**(1), 013,403 (2002).

[122] D. Blume and C. H. Greene, "Fermi Pseudopotential Approximation: Two Particles under External Confinement," Physical Review A **65**(4), 043,613 (2002).

[123] Z. Idziaszek and T. Calarco, "Analytical Solutions for the Dynamics of Two Trapped Interacting Ultracold Atoms," Physical Review A **74**(2), 022,712 (2006).

[124] J. F. Bertelsen and K. Mølmer, "Association of Heteronuclear Molecules in a Harmonic Oscillator Well," Physical Review A **76**(4), 043,615 (2007).

[125] F. Deuretzbacher, K. Plassmeier, D. Pfannkuche, F. Werner, C. Ospelkaus, S. Ospelkaus, K. Sengstock, and K. Bongs, "Heteronuclear Molecules in an Optical Lattice: Theory and Experiment," Physical Review A **77**(3), 032,726 (2008).

[126] B. Gao, "Quantum-Defect Theory of Atomic Collisions and Molecular Vibration Spectra," Physical Review A **58**(5), 4222–4225 (1998).

[127] B. Gao, "Angular-Momentum-Insensitive Quantum-Defect Theory for Diatomic Systems," Physical Review A **64**(1), 010,701 (2001).

[128] B. Gao, "General form of the quantum-defect theory for $-1/r^{\alpha}$ type of potentials with $\alpha > 2$," Physical Review A **78**(1), 012,702 (2008).

[129] O. Docenko, M. Tamanis, J. Zaharova, R. Ferber, A. Pashov, H. Knöckel, and E. Tiemann, "The coupling of the $X^1\Sigma^+$ and $a^3\Sigma^+$ states of the atom pair Na + Cs and modelling cold collisions," J. Phys. B At. Mol. Opt. Phys. **39**(19), S929–S943 (2006).

[130] B. H. McGuyer, M. McDonald, G. Z. Iwata, M. G. Tarallo, A. T. Grier, F. Apfelbeck, and T. Zelevinsky, "High-Precision Spectroscopy of Ultracold Molecules in an Optical Lattice," New Journal of Physics **17**(5), 055,004 (2015).

[131] S. G. Porsev and A. Derevianko, "Accurate Relativistic Many-Body Calculations of van der Waals Coefficients C_8 and $C_1 0$ for Alkali-Metal Dimers," The Journal of Chemical Physics **119**(2), 844–850 (2003).

[132] B. Bransden, C. Joachain, and T. Plivier, *Physics of Atoms and Molecules*, Pearson Education, 2nd ed. (Prentice Hall, 2003).

[133] B. P. Straughan, ed., *Spectroscopy. Vol. 3*, no. 122 in Science Paperbacks, 2nd ed. (Chapman and Hall, London, 1976).

[134] J. Zaharova, M. Tamanis, R. Ferber, A. N. Drozdova, E. A. Pazyuk, and A. V. Stolyarov, "Solution of the fully-mixed-state problem: Direct deperturbation analysis of the $A^1\Sigma^+ - b^3\Pi$ complex in a NaCs dimer," Physical Review A **79**(1), 012,508 (2009).

[135] A. Grochola, P. Kowalczyk, J. Szczepkowski, W. Jastrzebski, A. Wakim, P. Zabawa, and N. P. Bigelow, "Spin-forbidden $c^3\Sigma^+(\Omega = 1) \leftarrow X^1\Sigma^+$ transition in NaCs: Investigation of the $\Omega = 1$ state in hot and cold environments," Physical Review A **84**(1), 012,507 (2011).

[136] A. Grochola, P. Kowalczyk, and W. Jastrzebski, "Investigation of the $B^1\Pi$ state in NaCs by polarisation labelling spectroscopy," Chem. Phys. Lett. **497**(1-3), 22–25 (2010).

[137] J. L. Dunham, "The Energy Levels of a Rotating Vibrator," Physical Review **41**(6), 721–731 (1932).

[138] L. R. Liu, J. D. Hood, Y. Yu, J. T. Zhang, N. R. Hutzler, T. Rosenband, and K.-K. Ni, "Building One Molecule from a Reservoir of Two Atoms," Science **360**(6391), 900–903 (2018).

[139] N. V. Vitanov, M. Fleischhauer, B. W. Shore, and K. Bergmann, "Coherent Manipulation of Atoms Molecules By Sequential Laser Pulses," in *Advances In Atomic, Molecular, and Optical Physics*, B. Bederson and H. Walther, eds., vol. 46, pp. 55–190 (Academic Press, 2001).

[140] R. Wynar, R. S. Freeland, D. J. Han, C. Ryu, and D. J. Heinzen, "Molecules in a Bose-Einstein Condensate," Science **287**(5455), 1016–1019 (2000).

[141] T. Rom, T. Best, O. Mandel, A. Widera, M. Greiner, T. W. Hänsch, and I. Bloch, "State Selective Production of Molecules in Optical Lattices," Physical Review Letters **93**(7), 073,002 (2004).

[142] M. Korek, S. Bleik, and A. R. Allouche, "Theoretical Calculation of the Low Laying Electronic States of the Molecule NaCs with Spin-Orbit Effect," The Journal of Chemical Physics **126**(12), 124,313 (2007).

[143] P. J. Zabawa, "Production of Ultracold, Absolute Vibrational Ground State NaCs Molecules," Ph.D. thesis, University of Rochester, Rochester, New York (2012).

[144] L. R. Liu, J. T. Zhang, Y. Y. Yu, N. R. Hutzler, Y. Liu, T. Rosenband, and K.-K. Ni, "Ultracold Molecular Assembly," arXiv 1701.03121 (2017). 1701.03121.

[145] W. B. Cairncross, J. T. Zhang, L. R. B. Picard, Y. Yu, K. Wang, and K.-K. Ni, "Assembly of a Rovibrational Ground State Molecule in an Optical Tweezer," arXiv:2101.03168 [cond-mat, physics:physics] (2021). 2101.03168.